Jürgen Sattelkow, BSc

Semicrystalline Thin Film Cellulose: Close-to-Nature Substrates for In-Situ Atomic Force Microscopy

MASTER THESIS

For obtaining the academic degree
Diplom-Ingenieur

Master Programme of
Advanced Material Science

Graz University of Technology

Supervisor:

Ao.Univ.-Prof. Dipl.-Ing. Dr.techn. Gerald Kothleitner

Co-Supervisor:

Dipl.-Ing. Dr.techn. Harald Plank

Institute of Electron Microscopy and Nanoanalysis

Graz, January 2015

Acknowledgments

Firstly, I would like to take the opportunity to express my gratitude to the head of the Institute of Electron Microscopy and Nanoanalysis Professor Ferdinand Hofer and the head of the Institute of Biotechnology and Biochemical Engineering Professor Bernd Nidetzky and furthermore Prof. Gerald Kothleitner and Dr. Harald Plank for supervision and co-supervision, respectively.

Special thanks go to DI Thomas Ganner for his advice and assistance as well as DI Manuel Eibinger and Karin Siegl BSc of the Institute of Biotechnology and Biochemical Engineering for their biochemical support.

I wish to thank Ing. Claudia Mayrhofer for performing the ultramicrotomy cuts, Dr. Boril Chernev and DI Harald Fitzek for the Raman measurements, Mag. Johanna Kraxner for the TEM images, Dr. Johannes Rattenberger and Barbara Geier for the SEM images and Dr. Stefan Mitsche for his support with XRD.

I also want to thank all staff members of the FELMI/ZfE and all students working at the FELMI/ZfE for all the good work and time. It was a great experience working with you all.

I would like to say thank you to my friends and family for supporting me.

Finally a big gratitude goes to my girlfriend Bernadette Gsellmann for being by my side all the time and I hope this will never change.

"If I have seen further than others, it is by standing upon the shoulders of giants."
Isaac Newton

Abstract

Global climate change is currently a big issue significantly caused by carbon dioxide greenhouse gases. To reduce fuel-related aspects of CO_2 emission, strong emphasis is put on renewable resources such as cellulose, which can be considered an almost abundant source. In particular, enzymatic degradation into sugar and further fermentation to ethanol could be a successful route which is collectively called second-generation biofuel. Although sugar conversion is a natural process, the technically efficient application is still complicated. One reason for this is an incomplete understanding of the fundamental degradation mechanism and, in particular, its correlation to structural properties of cellulosic materials. To overcome this limitation, highly defined and tuneable substrates are needed which then allow fundamental studies in close-to-nature conditions in combination with localized methods such as Atomic Force Microscopy (**AFM**). In this master's thesis, new cellulose substrates have been developed which provide fully crystalline and mixed amorphous/crystalline cellulose properties. The main advantages compared to existing artificial cellulose substrates are the defined size of cellulose nano-crystals, its controllable content in the amorphous matrix, and the nano-flat surfaces with tuneable film thicknesses. In addition to the fabrication routes, this thesis investigates its morphological, chemical and structural properties by using **AFM**, scanning electron microscopy, transmission electron microscopy, X-ray diffraction and Raman spectroscopy. Together with degradation experiments using well-known enzymes, the close-to-nature character of the new materials could be proven. This substrate is therefore highly promising for new fundamental studies as demonstrated in this thesis for a novel enzyme revealing a slightly different activity than expected.

Kurzfassung

Der globale Klimawandel ist ein stetig steigendes Problem und wird neben vielen Faktoren speziell durch das Treibhausgas Kohlendioxid massiv verstärkt. Um den durch Treibstoff verursachten CO_2 Ausstoß zu reduzieren, werden gegenwärtig große Anstrengungen in erneuerbare Rohstoffe, wie zum Beispiel Zellulose als immer wieder nachwachsender Rohstoff, investiert. Ein besonders vielversprechender Weg ist der Einsatz von Enzymen zum Abbau von Zellulose in Zucker welcher durch Fermentation weiter zu Ethanol umgewandelt werden kann. Dieser Ansatz wird weitläufig als Biotreibstoffherstellung der zweiten Generation bezeichnet. Obwohl diese Umwandlung zu Zucker ein natürlicher Prozess ist, ist die technisch effiziente Umsetzung noch immer sehr komplex. Ein Grund hierfür ist das unvollständige Grundverständnis des Abbaumechanismus und im Speziellen der Zusammenhang mit strukturellen Eigenschaften der Zelluloseausgangsmaterialien. Ein Ansatz um diese Wissenslücke zu schließen ist es, hoch definierte und abstimmbare Substrate herzustellen, welche lokale Messmethoden wie die Rasterkraftmikroskopie (**RKM, AFM**(eng.)) ermöglichen, um dadurch unter „naturnahen Bedingungen“ biologische Prozesse auf molekularer Ebene zu studieren. Der Ansatz dieser Masterarbeit ist die Entwicklung derartiger Zellulose-Substrate, welche hochkristalline und amorphe Zellulosematerialien kombinieren. Die großen Vorteile des Ansatzes dieser Masterarbeit gegenüber bereits existierenden, künstlichen Zellulosesubstraten sind definierte Größe der Zellulosenanokristalle, die Kontrollierbarkeit des kristallinen Anteils in der amorphen Matrix und nanoflache Oberflächen deren Schickdicke sich sehr genau variieren lässt. Neben der Entwicklung der Substrate wurden in dieser Arbeit zusätzlich morphologische, chemische und strukturelle Substrateigenschaften mittels **RKM**, Rasterelektronenmikroskopie, Transmissionselektronenmikroskopie, Röntgendiffraktometrie und Raman-Spektroskopie charakterisiert. Zusätzlich wurden enzymatischen Abbauexperimenten unter Verwendung von wohlbekannten Enzymen durchgeführt, um den Naturnahen Charakters der neuen Materialien zu demonstrieren. Gerade aus diesem Grund sind diese neuen Substrate für fundamentale Studien mit neuartigen Enzymen sehr vielversprechend, wie im letzten Kapitel dieser Arbeit gezeigt wird.

Table of Contents

1 Introduction and Motivation

Global climate change will be a big issue in the foreseeable future. One of the major greenhouse gases is carbon dioxide, which we annually release from fossil resources at an ever increasing rate. To illustrate that, the atmospheric mixing ratio of CO_2 has increased from a preindustrial value of 280 ppm to over 390 ppm in 2011 [1]. This calls for renewable resources that are carbon dioxide-neutral [2]. A lot of effort has been put into this topic. Nevertheless a lot of these concepts have been proven to be ineffective or more expensive than existing ones. The idea of turning food into fuel while humans are still starving in many parts of the world is highly controversial. Because of this we thought that cellulose was a good point to start form. It grows in all kinds of grass, shrubs and trees consuming carbon dioxide. So in a well-cultivated cycle it would be an infinite resource and carbon dioxide-neutral. But it is not that easy. The process from grown plants to a fluid fuel is quite long and costly. A lot of research has to be done.

Cellulose consists mostly of polymeric-linked glucose. So first the cellulose has to be prepared for degradation enzymes that can break it down to glucoses. This is done by hydrolysis of cellulose either in a chemical way with sulfuric acid or with enzymatic hydrolysis by cellulases. One major problem of cellulose is the insolubility in water which makes it inefficient for a biochemical approach. Mechanical shred for batches is needed. The degradation product glucose can then be further fermented to obtain ethanol as fuel. All enzymes have to be grown in bacteria or fungi, making the process even more complicated. Although these technical issues can definitely be solved, one problem remains: a fundamental understanding of the degradation process of cellulose by enzymes which, however, are essential for optimization strategies for efficient hydrolysis.

Historically, two different approaches have been extensively used: *1)* biochemical experiments with an integral character and *2)* microscopic investigations in static conditions as described in detail in reference [3]. What was missing for a long time were dynamic investigations in natural conditions which provide localized information down to the molecular scale. In recent years several techniques have been developed in which Atomic Force Microscopy seems to be the most promising, due to the capability of liquid environments without the necessity of material labelling. However, to gain a deep understanding for fundamental processes there is another issue: a defined substrate! Although groundbreaking investigations have been carried out, including dynamic single enzyme spotting in the sub-second range [4–7], most of these investigations were performed on highly idealized cellulose substrates by means of either crystalline or amorphous materials. As nature does not consist of such highly idealized characteristics, the demand for mixed substrates arose which should also allow for tunable crystalline contents including controllable crystal sizes. This was the starting point at the Institute for Electron Microscopy and Nanoanalyis (**FELMI**, **TU Graz**), which focused on the development of defined and tunable cellulosic substrates. During recent years a variety of different model materials have successfully been developed and used for fundamental studies in collaboration with the Institute for Biotechnology and Biochemical Engineering (**TU Graz**). Although this cellulose substrate toolbox continuously grew and allowed for different, dedicated investigations, the "ideal" substrate has not been able to be fabricated so far despite the fact that a lot of work has been done in the master's theses of Mag. Judith Dohr, Timothy Aschl, DI Thomas Ganner and Stephanie Rošker [8–11]. However, the knowledge gained led to new ideas which had the potential to reach the final goal of a fully controllable cellulose substrate. This master's thesis describes these ideas and its successful transfer to a real fabrication route. **FELMI'**s toolbox has therefore been successfully completed by a very powerful substrate: the semicrystalline-thin-film-cellulose, or **SCTFC**.

2 Biological & Chemical Fundamentals

2.1 Cellulose

As part of the group of carbohydrates, cellulose is considered organic material along with sugar and starch which occur naturally in plant cell walls. Carbohydrates mainly consist of carbon, oxygen and hydrogen. Furthermore, cellulose has a polymer structure with the empirical formula $C_6H_{10}O_5$ as the individual repeat unit. Prokaryotes like bacteria and algae produce cellulose along with fungi. Also in eukaryotes 300 gene variations of glycosyl hydrolase family 9 (**GHF9**) cellulases have been found hence cellulose is a very old biological component [12].
Historically, cellulose was used by mankind long ago as fuel for fire, construction material (wood), tools, papyrus, paper and even as clothing (fibre). Then, in 1833, its chemical structure was discovered by the French chemist [13]. Since then it has been used even more in refined ways as packing material (cellophane), fabrics (viscose), and plastics (celluloid).
Starch also has a polymeric saccharide structure (nutrition), because it can be degraded down to sugar by most mammals. Cellulose on the other hand is not digestible for most mammals. The reason for this is the lack of enzymes necessary for full hydrolysis. When cellulose is degraded by hydrolysis the sugar produced can be further fermented into ethanol which can be used as biofuel and is then called second-generation biofuel. So far, cellulose seems to be the best solution for fuel production due to the huge amount of source material and the elimination of food-vs-fuel concerns. However, a main disadvantage of cellulose is its insolubility in water and most organic solvents, which makes ethanol production very inefficient and cost intensive. In the following, a closer look at cellulose structure and morphology is given to provide a brief overview of the main material for this thesis.

2.1.1 Molecular Structure and Chemistry

As mentioned above, cellulose has a polymeric structure in a linear and unbranched configuration (no side chains) commonly called ß-1,4-D-glucopyranose. The monomeric unit is a ß-D-glucopyranose where the D indicates the highest numbered asymmetric carbon atom of its former sugar molecule glucose. The D-glucose has the OH group on the right while the L-glucose (its stereo-chemical counterpart) has it on the left side. When the OH of the fifth carbon atom connects with the first carbon atom via nucleophilic addition it forms a cycle called D-glucopyranose. Pyranose originate from cyclic ether pyran. This happens in water at room temperature. Now it has an additional isomeric form (anomer) which is determined at the first carbon atom in comparison to the fifth carbon atom resulting in an alpha (equals *'trans'*) and a beta (equals *'cis'*) form. D-glucopyranose can turn into both anomers as schematically shown in Figure 1. The beta form is energetically the most stable from, but can change with a very low probability back into the intermediate and further into the alpha form [14]. Cycles of 6 membered rings can have different conformations like boat, chair, twisted boat, etc. However, due to thermodynamic equilibrium, the chair conformation is the most stable.

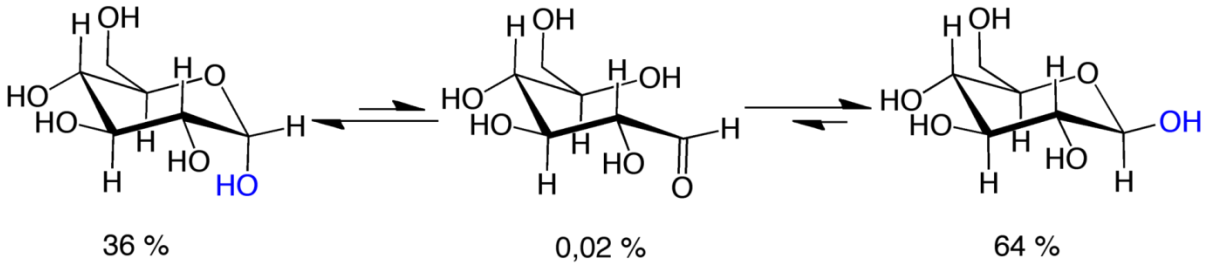

Figure 1: Indication of the different isomeric structures of α-D-glucopyranose with the blue hydroxyl in axial position (left), intermediate (centre) and ß-D-glucopyranose with the blue hydroxyl in equatorial position (right) [15].

In cellulose, two ß-D-glucopyranose units are linked alternating (180°) by their first and fourth carbon atom to a dimer cellobiose shown in Figure 2.

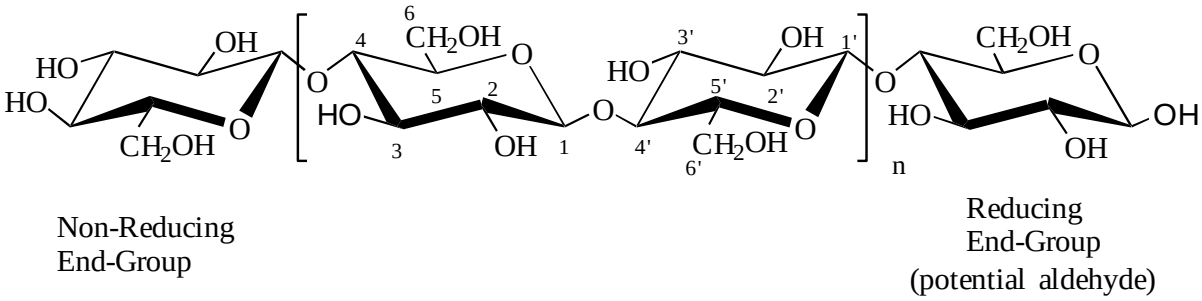

Figure 2: ß-1,4-D-glucopyranose dimer cellobiose (enclosed by the bracket) which builds up cellulose polymer chains with a reducing and a non-reducing end-group [16].

These cellobiose units are then repeated from several hundred up to many thousand times to form a single cellulose polymer chain. As an essential characteristic, every chain has a reducing and a non-reducing end which is the reason why different enzymes are needed for an efficient degradation. Chains are then hydrophilic bonded to each other to form single fibres [17].

2.1.2 Supramolecular Structure

Cellulose is polymorphic and occurs in 7 different crystalline structures, namely cellulose 1α, 1β, 2, 3_I, 3_{II}, 4_I, 4_{II} [18], which has been proven by nuclear magnetic resonance (**NMR**), infrared and diffraction studies [19, 20]. The common modifications in nature are cellulose 1 with triclinic 1α and monoclinic, more stable 1β. Both polymorphs coexist in the cellulose 1 structure. Swelling in concentrated sodium hydroxide and later reduction of swelling agent (mercerization) or dissolving and afterwards precipitation (curing or regeneration) of cellulose 1 gives irreversibly cellulose 2. Cellulose 3_I or 3_{II} are formed by treating either cellulose 1 or 2 with liquid ammonia or amine solutions and subsequent withdrawing ammonia/amines by evaporation. If these polymorphic products are further heated in glycerine, cellulose 4_I and 4_{II} are yielded. In Figure 3 an overview of the cellulose conversion is summarized [21, 22].

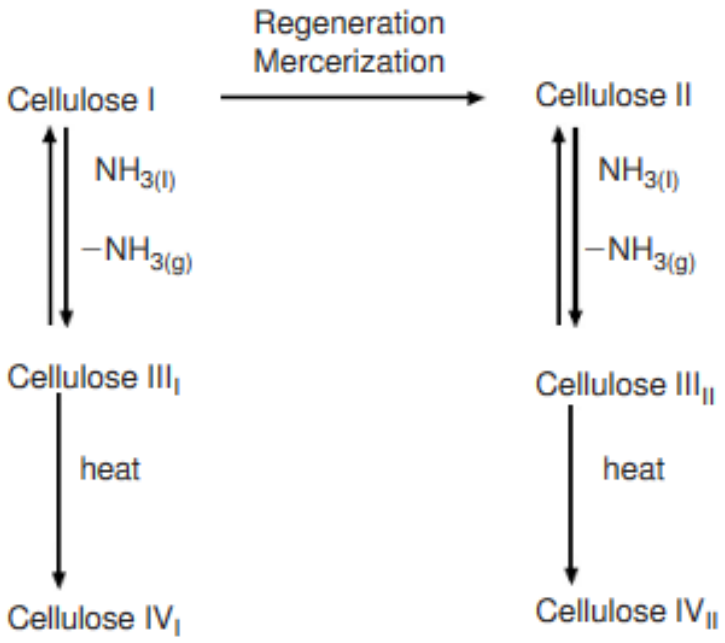

Figure 3: Conversion of cellulose polymorphs [18]**.**

2.1.3 Morphological Structure

Microfibrils, fibres, layers, cell walls, and many more morphological structures can be comprised of cellulose. The most common cellulose form is fibre. What cellulose structures in plants look like is shown in Figure 4. Fibres, films and other structures can be synthesized with regenerated cellulose [21]. Microfibrils are the basic crystalline form of natural cellulose and have typical widths between 2 nm and 50 nm with lengths up to tens of micrometres [23]. When cellulose is cured by exposure of trimethylsilylcellulose to chloric acid, microfibrils have a rather constant diameter of approximately 5 nm independent of the method of how they were synthesized [22].

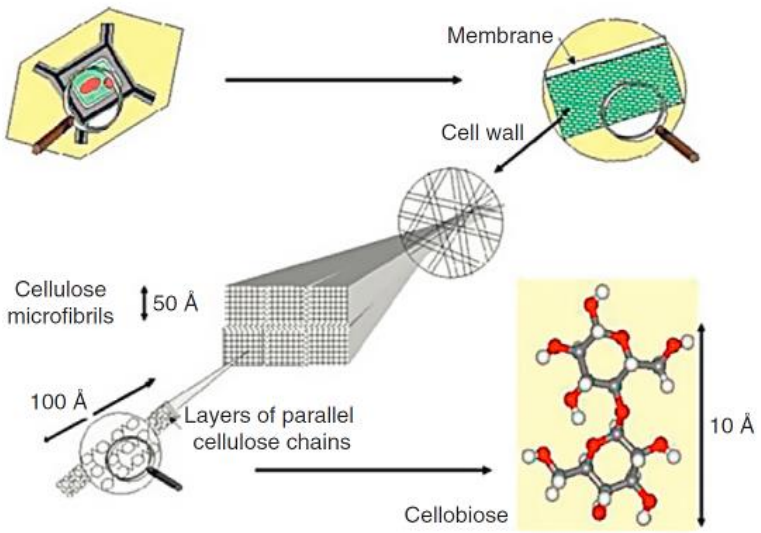

Figure 4: Morphology from a plant cell (top left) down to cellulose polymers (bottom right) [23]**.**

2.2 Cellulases

Cellulose is very stable due to its β-1,4-glycosidic bonds. To break these bonds, cellulases (degradative enzymes) are needed, which have a catalytic activity [6]. They lower the activation energy for hydrolysis while not be being consumed during the reaction. Cellulases are assigned to the group of glycoside hydrolase (**GH**) families, which includes all kind of enzymes capable of hydrolysing polysaccharides in plant cell walls [21]. Microorganisms like fungi, bacteria, certain plants and even insects like termites and cockroaches [24] have such cellulases as active enzymes. The *Trichoderma reesei* fungus exacerbated cellulosic material such as tents, sand bags and clothing of the US Army in World War II. Investigations to identify the fundamental origin led to the discovery of cellulases and triggered further intensive research on cellulose degradation [25].
The structure of cellulases consists of a carbohydrate-binding module (**CBM** or cellulose-binding domain **CBD**) and a catalytic part. The latter is the active element which hydrolyses the cellulose. The activity of the enzyme is amplified by the **CBM** as it binds to the insoluble substrates and has an influence during degradation of crystalline cellulose [26]. Typically, **CBM** first binds strongly with its amino acids to cellulose chains through Van der Waals interactions and then the catalytic module is able to attack the cellulose chains. In Figure 5, the gold-labelled **CBM1Cel7A** can be seen as black dots sitting on cellulose microfibrils; this has been shown by J. Lehtiö and J. Sugiyama et al. [27].

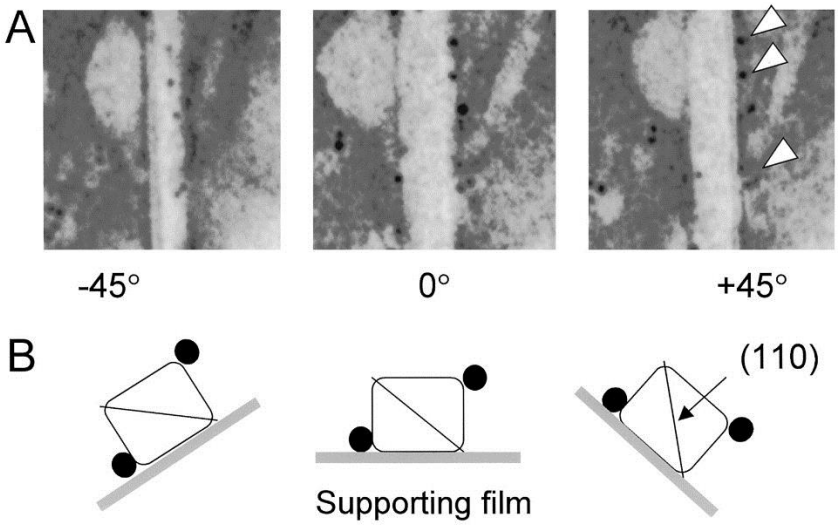

Figure 5: (A) TEM images (magnifications: x250) of gold-labelled CBM1Cel7A as black dots (and white arrows in the right image) sitting on cellulose microfibrils (light grey) on a supporting film (dark grey) rotated from initial 0° position in the middle to ±45° left and right. For a better understanding, a schematically illustration of the experiment is given in (B). Black circles indicate gold-labelled CBM1Cel7A on cellulose crystal with (110) net plain (arrow) [27].

A distinction between different cellulases can be made: whether they split the cellulose chains at the ends (exo-glucanases or cellobiohydrolase **CBH**) or internally (endo-glucanases **EG**). The product is always cellobiose (Figure 2) which can be cleaved to glucose by β-1,4-glucosidases (**BGL**).
For this thesis the *Trichoderma reesei* fungus was used as the source for cellusases. It contains **CBHs** as well as **EG** which are well studied in general but also at the Institute for Electron Microscopy [6] . In Table 1 cellulases formed in *Trichoderma reesei* are shown. **CBH** and **EG** produce cellobiose, but

cellobiose inhibits **CBH** and **EG**. Therefore, cellobiose has to be reduced to glucoses with **BGL** to run degradation experiments [28].

Table 1: Trichoderma reesei related enzyme components [21]**. Those which are relevant for this thesis are marked bold green.**

enzyme	former name
Cel7A	**CBH1**
Cel6A	**CBH2**
Cel7B	**EG1**
Cel5A	EG2
Cel12A	EG3
Cel61A	EG4
Cel45A	EG5

EG and **CBH** are cellulases that coexist and it has been shown that there is synergistic behaviour [7, 29, 30]. To illustrate the effects, Figure 6 gives an activity scheme where both cellulases types work together. The result of synergism is a higher activity of the multi-enzyme system compared to the activity of the individual enzymes. Such a multi-enzyme system can have either a combination of free cellulases or a multicomponent complex called cellulosomes [21]. Many types of synergism are possible. For example, endo-exo synergy where endo-glucanases divides chains while exo-glucanases reduces them or exo-exo synergy where different exo-glucanases attack the reducing and the non-reducing end of celluloses chains from each side. There is synergy between **CBM** that reduces cellobiose to glucose increasing the activity of **EG** [28]. At least three enzymes (two **CBHs** + one **EG**) are required for effective hydrolysis of cellulose which has been shown by K. Bhat and S. Bhat [25]. In this context it must be mentioned that our activities during recent years revealed the synergism as substrate dependent. In more detail it has been found that cooperative activity depends on crystal sizes and their distribution in the amorphous matrix [5]. Based on these pre-investigations it became evident that for a full understanding, highly-defined and controllable multi-phase cellulose substrates are essential which was a major intention for this thesis.

*The cellulases used in the experiments for this thesis all come from Trichoderma reesei and were prepared by DI Manuel Eibinger and Karin Sigl from the Institute of Biotechnology and Biochemical Engineering headed by Prof. Dr. Bernd Nidetzky (**TU Graz**).*

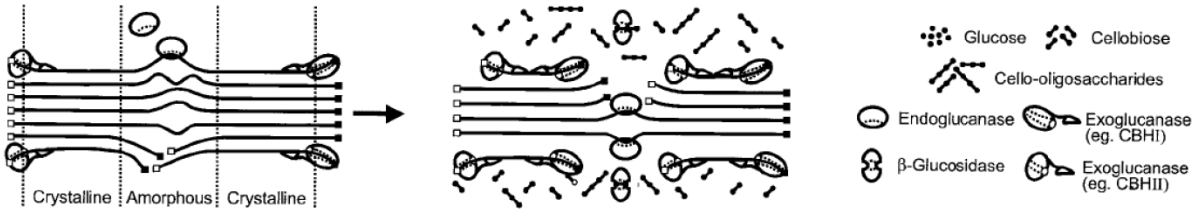

Figure 6: Scheme of synergistic effects between EGs and CBH enzymes during hydrolysis of amorphous and crystalline cellulose. Open squares represent non-reducing ends, solid squares represent reducing ends. Synergism effect in brief: EG open up cellulose chain increasing the number of binding sides for CBH enzymes [28]**.**

2.2.1 CBH1 (Cel7A)

CBH1 – with the official commission number **EC** 3.2.1.91 – represents an exo-glucanase which reduces cellulose into cellobiose from the reducing end of the cellulose chain. The shape of **CBH1** shows a tunnel 50 Å in length through which the cellulose is processed and separated into cellobiose (see Figure 7) [10]. It has been shown that **CBH1** operates mainly on crystalline structures of cellulose [7]. It can be isolated from the supernatant **SVG**.

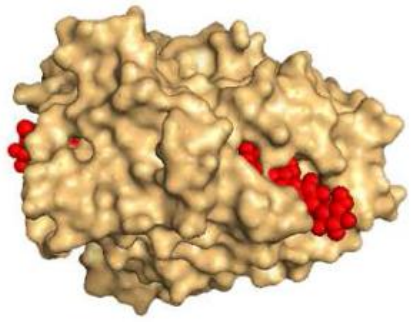

Figure 7: Simulated 3D structure of CBH1 with catalytic tunnel (red) in which single cellulose chains are processes [10]**.**

2.2.2 CBH2 (Cel6A)

In comparison to **CBH1**, **CBH2** (EC 3.2.1.91) is also an exo-glucanase but it attacks the cellulose from the non-reducing end. Figure 8 gives the simulated shape of **CBH2**, which has some similarity to **CBH1** concerning the processive tunnel. **CBH2** was thought to mainly work on amorphous areas [10]. However, during our activities we found clear indication that **CBH2** is an all-rounder that can also be very active on crystalline cellulose as long as the fibres are sufficiently small [7, 31]. These dual capabilities are the main difference compared to **CBH1** and give **CBH2** a considerably important character. It was provided to us by the Institute of Biotechnology and they obtained it from ***ACIB*** [32].

Figure 8: Simulated 3D structure of CBH2 with the catalytic tunnel in the centre [10]**.**

2.2.3 EG1 (Cel7B)

EG (EC 3.2.1.4), by contrast, is an endo-glucanases which binds to a random site on cellulose chains and cuts them into two smaller chains which then increase the number of chain-ends for further **CBH** degradation. This enzyme is shaped like a grabber as can be seen in see Figure 9 [10]. Due to steric reasons it becomes evident that **EG** is most efficient for exposed cellulose fibres as can be found in amorphous regions and small crystals. . It was provided to us by the Institute of Biotechnology and they purchased it from Megazyme.

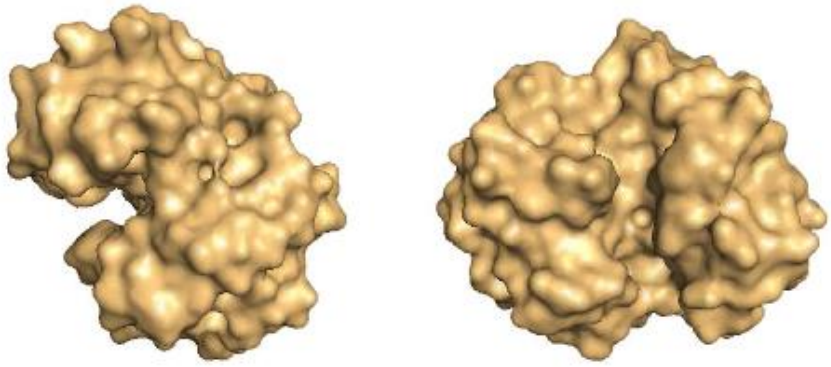

Figure 9: Simulated shape of EG in a side and bottom view, where the grabber and trench features become evident [10]**.**

2.2.4 Supernatant (SVG)

The supernatant is extracted from the *Trichoderma reesei* fungus and whenever **CBH1**, **CBH2**, **EG** and **BGL** are present in the same solution, it is called supernatant or **SVG** as is used to a great extent in this thesis and former studies [6]. This is important because it represents a combination which can often be found in nature and therefore is of essential importance in this thesis [33]. **SVG** has a ratio of 50 - 60% **CBH1**, 15 - 20% **CBH2**, 10 - 20% **EG1** and 1% **BGL**, furthermore it contains **EG** 2, 3 and 4 in very small amounts that can be neglected [3]. The **BGL** has a very important role although it has no degradation action. As described above, it splits cellobiose (see monomer in the middle of Figure 2) into glucoses. The enzymes **CBH1**, **CBH2** and **EG1** produce cellobiose and would reduce activity at high concentrations of cellobiose, thus **BGL** prevents inhibition by cellobiose accumulation [7].

The long-term goal concerning the supernatant is to find appropriate relative concentrations which allow highly efficient degradation of cellulose widely independent of their structural peculiarities. However, before that can be done, a fundamental understanding of individual, cooperative and structure-related activities is needed which immediately leads to the high relevance of defined and controllable cellulose substrates.

2.2.5 Swollenin (SWO1)

Another rather new protein investigated at the end of this thesis is swollenin. It has an expansin-like domain followed by a linker region that has an *N-terminal fungal* type cellulose-binding domain at its end. Expansin is an enzyme found in plant cells that unlocks the network of wall polysaccharides,

enabling cell enlargement [34]. Additionally, swollenin has regions which are similar to mammalian fibronectin type III repeats. It can be isolated form the fungus *Trichoderma reesei* which makes it odd, because it is the first time that mammalian fibronectin type III repeats were found in a fungal protein [35]. Fibronectin plays a role in trans-membrane linkage [36].

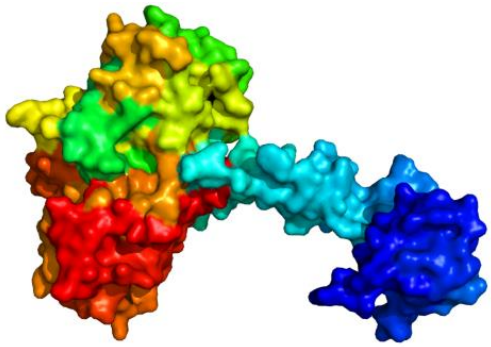

Figure 10: Structural simulation of swollenin with CMB (blue) and conserved domains (green to red) done by DI Manuel Eibinger.

The activity of swollenin is not yet fully understood. Its name results from the proven ability to swell cotton fibres due to internal disruption. However, the formation of reducing sugars (as is the case with **EG**) could not be observed [35]. More recent literature indicates that swollenin aids in enzymatic hydrolysis by disrupting hemicellulose [37]. Recently, it was hypothesized that it might swell the cellulosic material which then simplifies the penetration of active enzyme components into the bulk and therefore increases the efficiency. To test this hypothesis, we have first investigated this enzyme's activity on highly crystalline regions followed by activity screening in multi-phasic cellulose substrates (chapter 6.4.3).

3 Experimental Techniques

3.1 Atomic Force Microscopy

In 1982 G. Binning, H. Rohrer and E. Weibel [38] invented the scanning tunneling microscope (**STM**) and laid the foundation for the development of the atomic force microscope (**AFM**) in 1986 by G. Binnig, C. F. Quate and C. Gerber [39].
The **AFM** is a scientific instrument that operates in a close range to the sample thus "feeling" the sample's surface. It works ideally on very flat samples with features of less than 1 µm height and has the advantage of a non-destructive character allowing further specimen processing. Also, **AFM** allows for spatial resolution in the nanometre range and below which makes it an ideal tool for nanotechnology. Furthermore, **AFM** can not only be used in ambient conditions but also under (ultra-)high vacuum conditions and, most importantly for this thesis, in liquid environments which makes it ideal for the observation of in-situ biological processes.
Nowadays there are many different operation modes that have been developed over the years. This includes the detection of chemical, mechanical, magnetic, electrostatic or optical properties [40]. Recent advances led to real high-speed scanning, providing image rates in the second range and below. In the following, a brief overview of **AFM** technology is given, with a focus on the most important modes; for deeper insight, the reader can choose from a great deal of literature [39–44].

3.1.1 Principle

The **AFM** uses a sharp tip placed at the end of a cantilever. The cantilever acts as a transducer for attractive and repulsive forces acting on the tip and connects it to a piezoelectric motion system that moves the cantilever. A laser beam is reflected from the back of the cantilever on a photo detector. The most often used laser beam method measures the movement of the tip and keeps certain physical parameters of the cantilever-tip system (deflection, amplitude, phase, frequency, etc.) constant via a feedback loop. A schematic of the main components for **AFM** is shown in Figure 11.

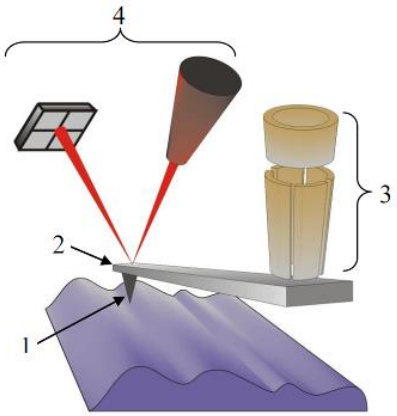

Figure 11: Schematic of AFM main components: tip (1), cantilever (2), piezo motion system (3), laser/detection system (4) [45]**.**

3.1.2 Components

The following components of the **AFM** are the cantilever-tip system, piezo motion system and detection and feedback system and will be described in more detail.

3.1.2.1 *Cantilever-Tip System*

The tip of the cantilever is the most essential part of the **AFM** system. Shape, size and radius at the apex of the tip limit characterization of surfaces. Most cantilever-tip systems are manufactured microelectronically with materials like silicon or silicon nitride. The tip sits at the end of the cantilever. As the cantilever is an expendable item it is attached to a plate for better handling. The resolution is tip radius dependent and common tips have a radius between 5 nm to 10 nm, but very expensive tips with a radius of 2 nm are also available.
The image quality is also influenced by the surface investigated. A very fine tip can pick up dirt or can be damaged when it hits a hard surface thus leading to convolution artefacts. The principle of convolution can be observed in Figure 12 while Figure 13 shows how convolution (right image) can look like in a real experiment.

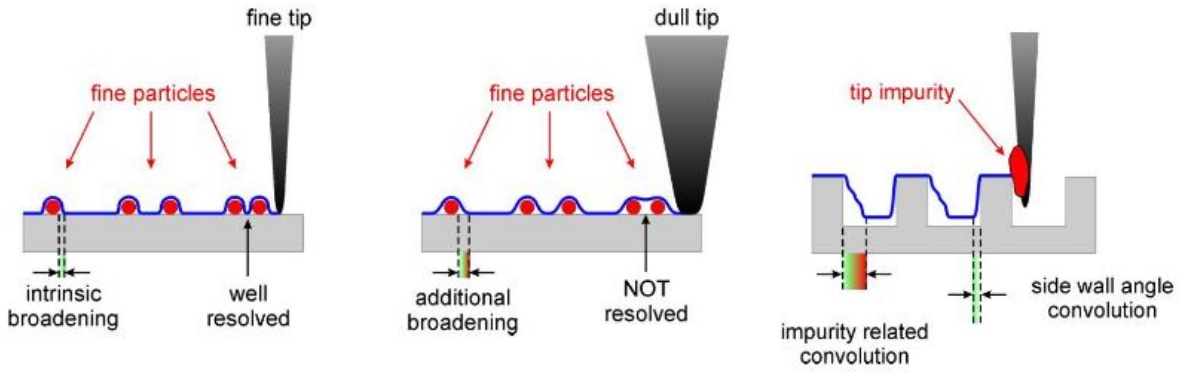

Figure 12: Schematic of image quality of high resolution with a fine tip (left) compared to a dull tip (middle) that cannot resolve fine features. Distortion of the true sample structure by particles is also possible (right) [45].

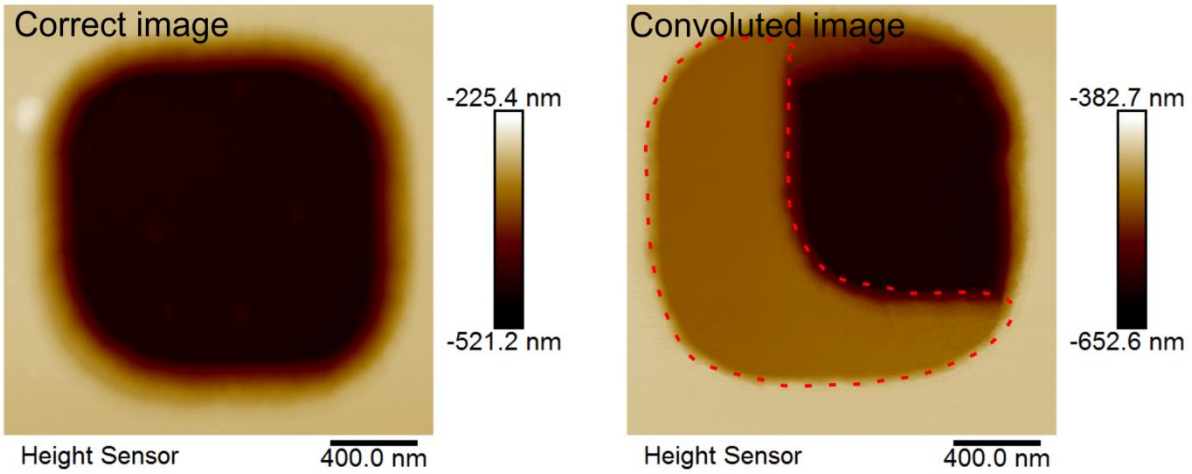

Figure 13: AFM height images of a standard sample imaged with a completely and clean tip (left) and a broken tip resulting in a convoluted image (right). The red dashed line indicates the image artifact.

Common cantilevers possess V-shaped or rectangular geometries as shown in Figure 14. V-shaped cantilevers are used to reduce torsional movements and allow lower overall spring constants compared to rectangular cantilevers. Therefore, V-shapes are mainly used for contact mode operation while the tapping mode mostly uses rectangular shapes.

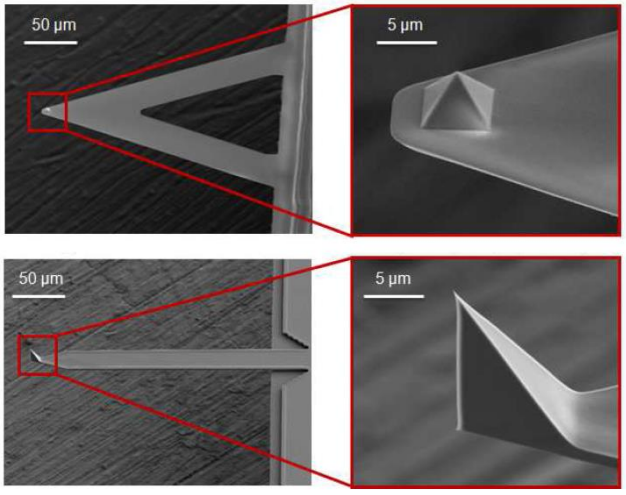

Figure 14: SEM image of tip geometries. Top: V-shaped cantilever with a pyramidal tip. Bottom: rectangular cantilevers with tetragonal tip [45]**.**

3.1.2.2 *Motion System*

The piezoelectric effect leads to deformation to the crystal lattice of piezoelectric materials when an external potential is applied. This deformation is very small but extremely accurate and fast. Therefore piezoelectric actuators are perfect for accurate, fast and fine movements which are required for cantilever motion. A tube scanner is an often-used scanner design (see Figure 15) as it eliminates a separate scanning stage and therefore is much more flexible with regard to the sample geometries or weight. One part is a ring that is responsible for the vertical z-movement. Below, there is a 4-segmented ring for control of the x- and y-direction (see Figure 16).

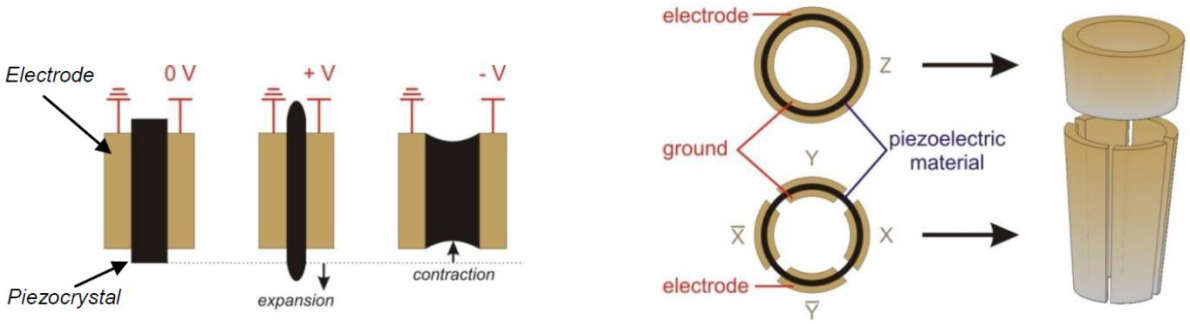

Figure 15: Left: Principal of the piezoelectric effect with expansive and contractive deformation when an external voltage is applied. Right: Schematic of the tube scanner consisting of an upper ring for z-movement and a lower ring for x- and y- movement [45]**.**

The scanning range of an **AFM** is in the scale of nm² to µm² areas. However, the motion of the tube scanner is more complicated. Coupling among the lateral and vertical motions of the piezoelectric behaviour does not depend linearly on the voltage. Hysteresis, creeping and other aberration effect have to be corrected by the software in real time. Regular recalibration is essential [40]. Image arte-

facts can be additionally corrected with software like Gwyddion [46, 47] for accurate image interpretation.

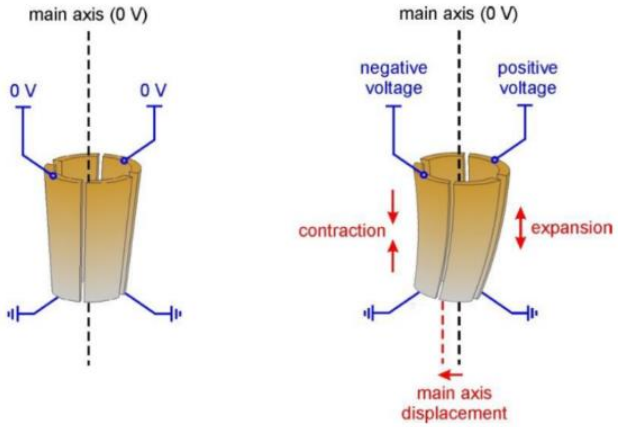

Figure 16: Schematic of the x- and y-motion of a tube scanner [45]**.**

3.1.2.3 *Detection and Feedback System*

For detecting the deflection of the cantilever, a highly sensitive system is needed. This is commonly achieved with an optical beam reflected at the very end of the cantilever and detected by a 4-segmented position sensitive photodetector (**PSD**). Bending and torsion of the cantilever sends the laser beam to different positions of the **PSD**, thus detecting normal and lateral forces (illustrated in Figure 17). In contact mode friction force would result in lateral deflection at the detector. The system has to be well adjusted to enable high sensitivity down to deflections of 0.01 nm or lower, depending on the overall noise level of the detection system (laser → cantilever reflection → detector).

Another possibility is to use self-sensing cantilever such as piezoresitive cantilevers, which are increasingly interesting due to the simplicity of use. These cantilevers have a layer of piezoelectric material that reacts to deflection by changes in resistance. This is due to deformational strain or stress of the piezocrystal lattice. The result is a shift of the electrons in the band structure and therefore a change in resistivity [44]. The main advantage, however, is the absence of any setup by means of laser positioning and rearrangement which gives much more freedom concerning the measurement conditions (e.g. in liquid or low temperature conditions).

The information gathered about the deflection from the tip-cantilever system is used to calculate a feedback signal. The feedback system (called feedback loop) tries to keep deflection constant by adjusting the motion system. For each x-y-position the feedback loop records the correction and processes it into an image with surface topology information [40].

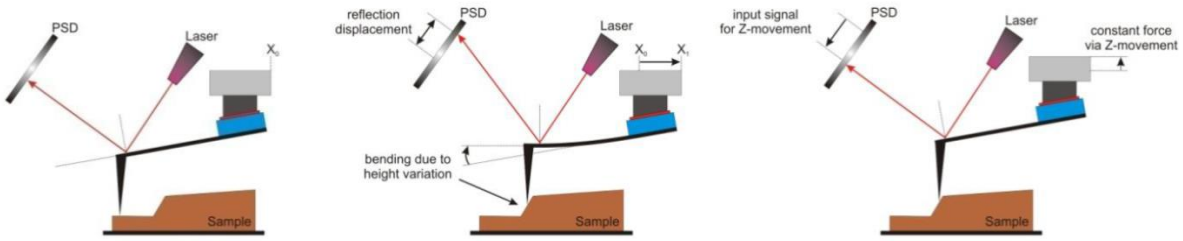

Figure 17: Laser detection system, from left to right to motion of the cantilever is shown and what happens when the tip reacts to a change in morphology. The PSD detects the change in height (middle) and the feedback loop adjusts the height via the motion system (right) [45]**.**

3.1.3 Interaction Forces

The interactions between tip and sample system result from a variety of forces. Depending on the distance and strength, different forces can be described for **AFM** measurements (see **Table 2**).

Table 2: Effective forces between tip and sample [45].

Tip-sample distance r	Effective forces	Dependence on potential (a, b, c … constants)
> 10 nm	Electrostatic/magnetic	$\frac{c}{r^2}$
10 to 5 nm	Van der Waals (dipole-dipole interactions)	$-\frac{a}{r^6}$
< 0.2 nm	e^- - e^- repulsion (Pauli principle)	$\frac{b}{r^{12}}$

Usually, experiments are performed at a distance between tip and sample of less than 10 nm, which neglects electrostatic and magnetic forces. The forces left can be combined into one formula (1): the Lennard-Jones potential V_{LJ}.

$$V_{LJ} = V_{ee} + V_{vdW} = \frac{b}{r^{12}} - \frac{a}{r^6} \tag{1}$$

The Pauli principle states that it is impossible for two electrons to occupy the same quantum state at the same location. They have to differ in at least one of the four quantum numbers. This is the reason why electron-electron interactions V_{ee} are repulsive and the tip is pushed away from the surface of the sample by this force. On the other hand, the Van der Waals contribution V_{VdW} is attractive, causing the tip to be drawn towards the surface of the sample. Van der Waals interactions have a longer range than the repulsive electron-electron interactions. So the tip is first drawn towards the surface sample and will then stay at a certain equilibrium distance where the attractive force and the repulsive force cancel each other out giving a potential minimum. If the tip is then pushed further towards the sample surface it will be repelled (see Figure 18).

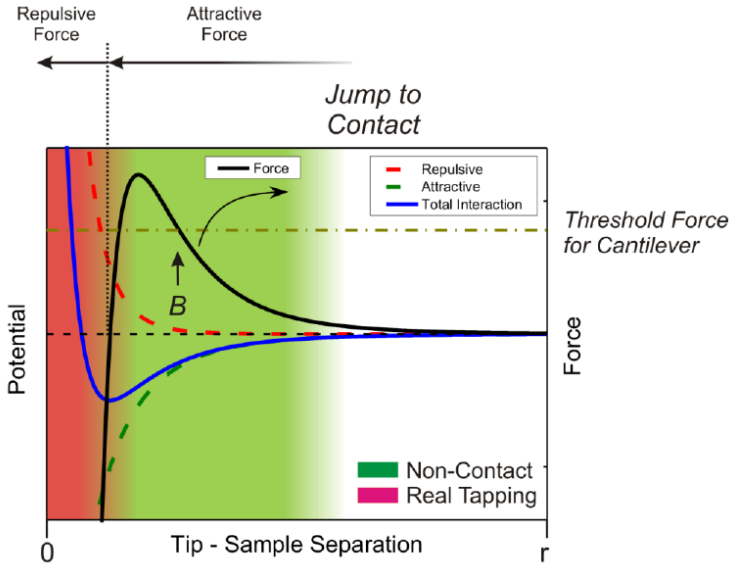

Figure 18: Diagram of how the attractive (green) and repulsive (red) potentials combine to a total interaction (blue) [45].

Under ambient conditions, capillary forces also have to be considered. For **AFM** measurements, water condenses from the atmosphere on the sample surface and can form a meniscus around the tip. This has several effects on the image quality. When the **AFM** was introduced in 1986 G. Binnig et al. [39] reported the covering of samples by water. Sometimes this can be a big problem, however in liquid environments this effect vanishes [40].

3.1.4 Operation Modes

There are a lot of operation modes that can be performed by the **AFM**, however in the thesis only Tapping Mode-based modes were used. In the following, tapping in air is described to derive the operating principles, and then application in liquid environment and fast scanning will be described.

3.1.4.1 *Tapping and Phase Mode*

For this mode the cantilever is oscillating over the sample. Therefore the tip is only tapping onto the substrates surface but not permanently toughing it which makes it good for investigating sensitive materials. The resonance frequency of the cantilever is set for oscillation. Depending on the type of cantilever the resonance frequency can range from 50 kHz to 1500 kHz. As a rule of thumb for classical cantilevers, lower resonance frequencies mean softer tips (exceptions are micro-cantilevers for high-speed scanning as discussed later). Soft means spring constants of 5 N/m and less. This is in accordance with the mechanical resonance where f is the resonance frequency formulated in equation (2), k is the spring constant and m is the mass [48].

$$f = \frac{1}{2\pi}\sqrt{\frac{k}{m}} \tag{2}$$

Before approaching the surface a fixed amplitude value of the oscillation has to be set. Higher amplitude values can increase image quality, and thin layers of water are more likely to be penetrated, but the risk of permanent tip damage is increased. When the tip is oscillating close to the surface while scanning it, the interaction forces between tip and sample surface cause damping of the amplitude (see Figure 19). The feedback system keeps the amplitude at a constant value thus the z-position of the cantilever has to be adapted accordingly. From this z-positioning, the topography (height image) is calculated by the software due to individual z values for each x/y-position in the scan range.

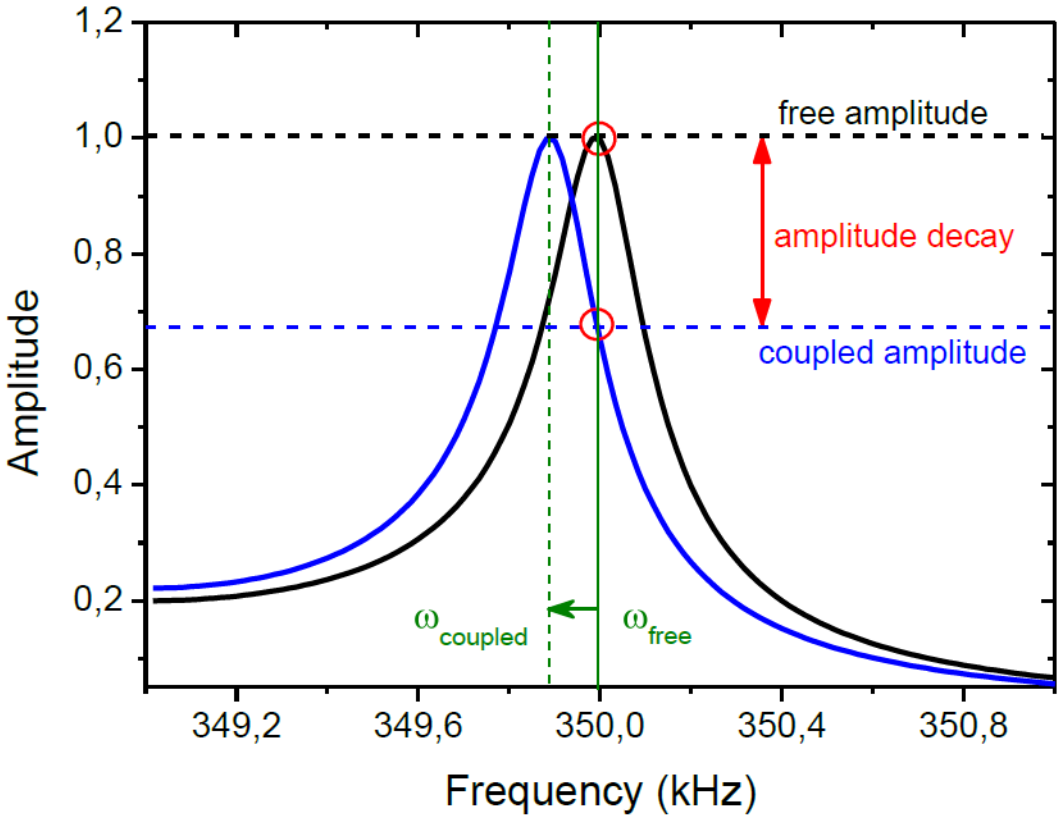

Figure 19: Resonance frequency of the free amplitude (black) and the coupled amplitude (blue) thus shifting the resonance frequency in tapping mode [45].

The interaction forces within interaction distance in tapping mode **AFM** are called attractive or repulsive working regimes according to their corresponding forces [48]. In the attractive regime mostly Van der Waals forces cause damping with the advantage of not toughing the surface. Therefore it is also considered as non-contact mode which is excellent for very sensitive materials. The only problem that arises is that imaging can be severely complicated by the water meniscus forming around the tip. This is prevented in the repulsive regime where the tip continuously "taps" the sample surface while Pauli-repulsion is predominant. In many cases, the repulsive regime delivers better image resolution because of the short range of the interacting forces. The downside of this working regime is the wear-off of the tip, thus making it dull, and also possible sample damage which strongly depends on the force exerted by the tip and the energy dissipation mechanism [49].
For more sophisticated measurements another operation method is possible: the phase mode. When the cantilever is excited to oscillation, there is a phase lag between the excitation and the actual oscillation of the cantilever. This information is dependent on composition or distribution of the material and can be used to gather additional information about the substrate (phase image). The advantage of phase imaging is that it is simultaneously acquired with the height information in tapping mode. For instance a sample that appears to be totally flat in the height image can be composed of crystalline and amorphous structures which are revealed in the phase image. Different chemical composition is also easily spotted in the change of phase lag. In Figure 20, the phase image emphasizes distinct topographical features [40].

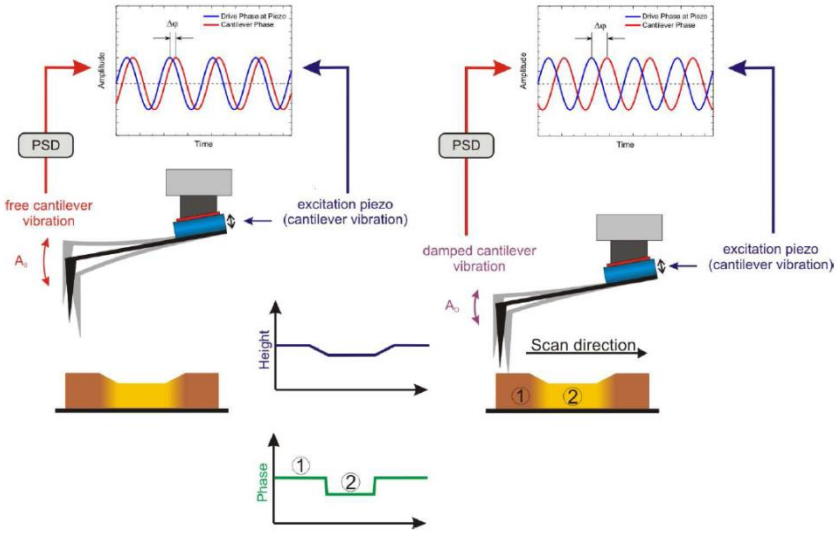

Figure 20: Operation scheme of AFM phase mode based on the phase lag between exciting and detected frequencies which change whenever the interaction forces vary (e.g. due to chemistry, structure or properties) [45]**.**

3.1.4.2 *Tapping Mode in Liquids*

Tapping mode in liquid **AFM** is a very powerful application allowing, for example, in-situ characterization of biological processes. In fact there is no alternative to biological activities observed with nanometre resolution in natural environments, which drove the development of the latest state-of-the-art instruments, such as the FastScanBio platform available at the **FELMI**. The downside is that with the liquid environment there are many issues to be aware of. There are new variables like double-layer forces that come into play, while single resonance behaviour of the cantilever is no longer true. Instead, a "resonance spectrum" emerges from the liquid environment and the resonance of the cantilever is shifted to a lower frequency. It is found, if at all, at a fraction of four to five (see Figure 21) of the former resonance frequency. Other frequencies do not represent eigenmodes of the cantilever but resonances of enclosing instrumental assembly interacting in liquid with one another. Moreover, the deflection of the cantilever is not symmetric any more, thus a sinusoidal wave approximation is not true and higher eigenmodes of the excitation frequency cannot be neglected any longer. Also the damping in liquid is much stronger than in air which, however, is the key for real high-speed scanning as ringing behaviour at morphological features is massively reduced allowing for fast vertical adaption [40].

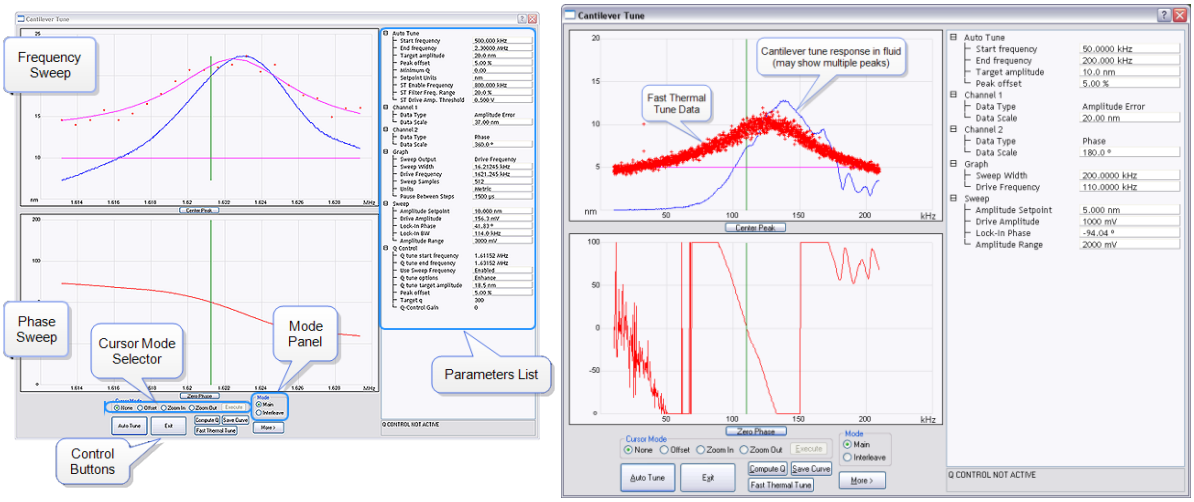

Figure 21: Characteristic resonance curve of a cantilever in air (left) and disfigure curve in liquid with a fast thermal tune which needs lots of experience to operate (right) [50]**.**

3.1.4.3 *Fast Scan Tapping*

The **AFM** scan speed is limited by many variables ranging from the instrumental resonance frequency, over cantilever aspects towards the environments in which the measurements are performed. While the first aspect can be solved by a smart mechanical design, and it is not particularly limiting, the two latter effects can be a problem. The main point is that the system needs to adapt the scanner position as fast as possible to topographical features. This requires a high oscillation frequency of the cantilever to allow for high scan speeds. Nowadays, this can easily be done via micro-cantilevers, with an area as small as 15 micrometre in length, allowing for resonances between 1 and 2 MHz. The most critical issue, however, is a sufficiently high damping. This can be understood since any oscillating systems needs some time before it reaches a stable oscillation after a topographical variation. There are two approaches to achieve this goal: ***1)*** special cantilevers which have a very high intrinsic damping (e.g. polymer cantilevers); and/or ***2)*** suitable environments which provide this damping. The latter is intrinsically provided by liquid conditions which enable high-speed scanning with frame rates up to 1 frame per second or even better. In our case, a new **AFM** was installed at the institute in 2014: the FastScanBio platform from Bruker Nano. The scan head of this instrument is shown in Figure 22, which is dedicated for high-speed operation in liquids. The right image gives a bottom view which also shows the dedicated micro-fluid cell which is specially designed to in-situ liquid investigations of a biological sample. Attached to the micro-fluid cell is an injection system allowing the operator to insert solutions containing, for example, enzymes. In chapter 6.1 the system, its capabilities and performance are described in more detail as an essential part of this thesis.

Figure 22: *FastScan Bio* hardware with micro-volume fluid cell mounted for biological AFM experiment front view (left) and from below (right) [50]**.**

X-Ray Diffraction

X-ray diffraction (**XRD**) is an analytical method that can characterize the lattice structure of materials [51–53]. According to Braggs's law, only constructive interference of diffracted X-rays from the lattice planes results in a detected signal following the equation:

$$2d\ \sin\theta = n\lambda \tag{3}$$

where λ means the X-ray wavelength used, d is the lattice spacing and θ is the diffraction angle. The detected signals show very sharp peaks for crystalline structures, broadened peaks for poly-crystalline and semicrystalline materials and very broad peaks for amorphous materials [54] due to the stochastically arranged distance of neighbouring structures. Therefore information about the present materials, their arrangement and the related degree of ordering can be accessed.

In this thesis we used **XRD** measurement to distinguish individual cellulose structures: Cellulose 1 and cellulose 2 have crystalline parts and can be differentiated as shown in Figure 23. Cellulose 1 has three typical peaks; two around $2\theta \sim 15°$ originating form 101 and $10\bar{1}$ netplanes and a sharper main peak at $2\theta = 22.7°$ that pertains to 002 reflex. A schematic of cellulose 1 crystallographic planes is shown in Figure 24. For cellulose 2, the 101 and $10\bar{1}$ reflexes are shifted away from each other, and 101 now occurs at 12° and $10\bar{1}$ at 20° [55–57].

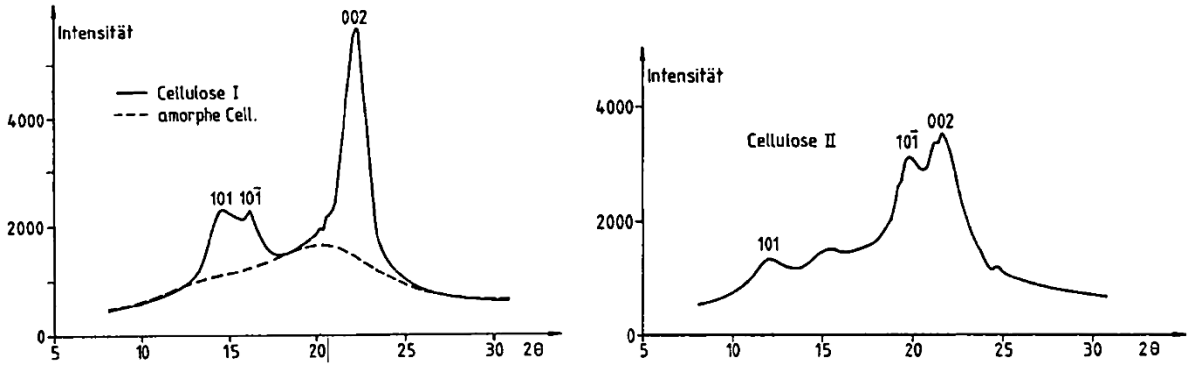

Figure 23: XRD spectra of cellulose 1 and amorphous cellulose (left) and cellulose 2 (right) [57]**.**

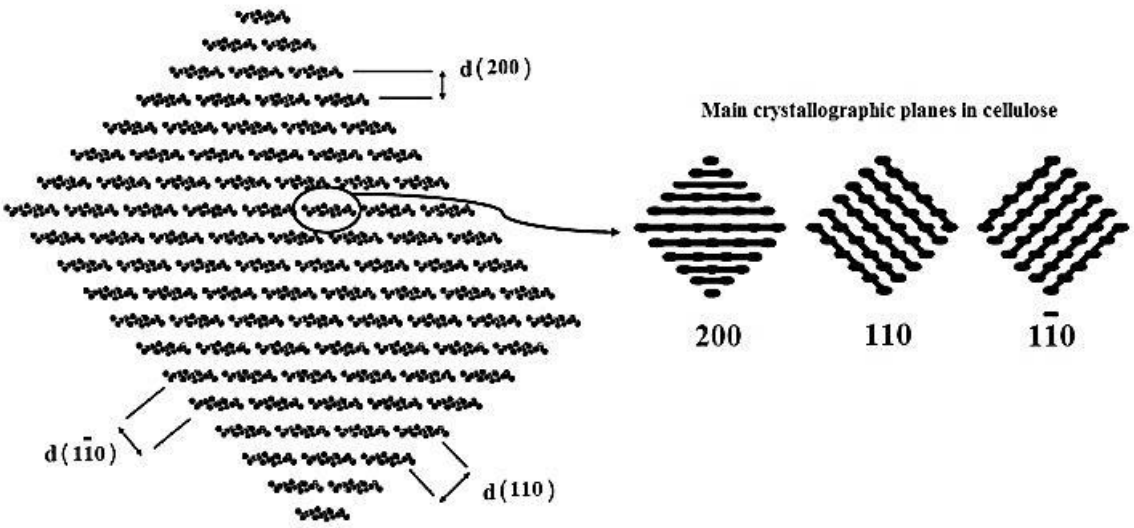

Figure 24: Schematics of cellulose crystallographic planes that are visible in XRD spectra [58]**.**

X-ray analyses were conducted on a Siemens D 5005 X-ray diffractometer (CuKα 1 radiation; Siemens, Munich, Germany) and supported by DI Thomas Ganner from the Institute for Electron Microscopy and Nanoanalysis.

3.2 Raman Spectroscopy

Raman spectroscopy is used to chemically identify incorporated materials and also to access chemical binding properties as well as their crystallinity in specific cases [56, 59–61]. This is achieved by exciting electrons in the specimen of interest into a virtual state with monochromatic light. When the electrons relax from these virtual states into higher or lower energy states, Stokes or Anti-Stokes shifted signals can be detected, which is the foundation for Raman spectroscopy [60]. Performing Raman spectroscopy on cellulose samples offers the opportunity to investigate the degree of crystallinity of cellulose and its crystalline structure [56] by typical peaks shown in Figure 25 [62].

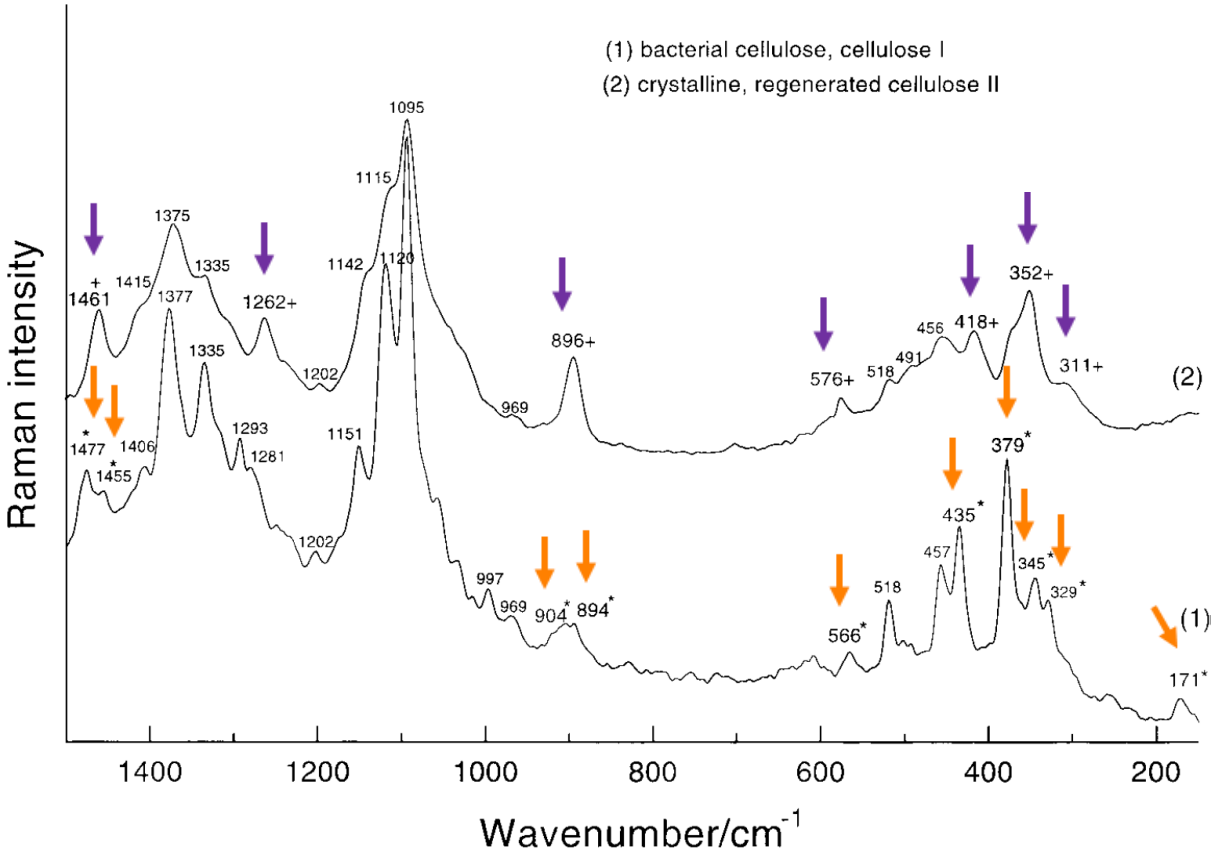

Figure 25: Raman spectra of cellulose polymorphs, typical frequencies for cellulose 1 (lower spectra 1) are highlighted with orange arrows and cellulose 2 (upper spectra 2) highlighted with purple arrows [9, 62].

Raman spectroscopy therefore expands **XRD** measurements by direct chemical identification as an essential part of a comprehensive characterization.

Raman investigations were performed on a LabRAM HR Raman (Horiba Ltd., Tokyo, Japan) by Boril Chernev at the Graz Centre for Electron Microscopy.

3.3 Transmission Electron Microscopy

In principle, transmission electron microscopy (**TEM**) can be compared to a transmitted light microscope (**LIMI**). While **LIMIs** resolution is limited by the wavelength of visible light in the range of 10^{-7} nm [63], **TEM** uses electrons according de Broglie wavelengths in the range of 10^{-12} nm depending on the primary electron energies used. Following the Rayleigh criteria for the simplified description of lateral resolution

$$\Delta d = \frac{1{,}22 * \lambda}{\sin \alpha} \tag{4}$$

where d is the resolvable distance, λ the used wavelength and α the opening angle during inspection, it follows that the much smaller wavelength for electrons (factor 10^5) allows resolution in the Å range and below [63]. With additional improvements concerning spherical/chromatic aberrations and highly monochrome primary energies, state-of-the-art **TEMs** can indeed provide lateral resolution in the subatomic range. The setup of a **TEM** is rather complicated but in principle consists of an electron source

(field emission for highest resolution), an optional monochromator, (corrected) condenser and objective lenses and suitable detectors for collecting a variety of electron species in different angles. Besides the unsurpassed lateral resolution, **TEM** inspection also allows for determination of crystal structures (electron diffraction) and chemical analysis by energy dispersive X-ray spectroscopy (**EDXS**) and electron energy loss spectroscopy (**EELS**) [63]. Although superior in their capabilities, one bottleneck is the sample preparation and in case of biological materials low contrast in those **TEM** images. For our situation we followed two approaches to slightly compensate these issues: *1)* preparation was carried out by directly preparing the cellulosic materials on nanometre-thin carbon films which eliminates further sample preparation; and *2)* we used classical staining approaches using uranyl acetate to increase the contrast from crystalline cellulose materials against an amorphous background. The intention for using **TEM** in this thesis was to provide an inside-view of thin layers which cannot be provided via surface techniques such as **AFM** or **SEM** but also to have a high-resolution technique to correlate particle shapes with **AFM** data to estimate convolution influences by the **AFM** tip.

***TEM** investigations were performed on a Tecnai F20 (FEI, The Netherlands) by Mag. Johanna Kraxner at the Graz Centre for Electron Microscopy.*

3.4 Scanning Electron Microscopy & EDX

Compared to a **TEM** a scanning electron microscope (**SEM)** is less complex although similar in the technical setup: An electron source (field emission gun for highest brightness) sends electrons through a lens system which de-magnifies, corrects, focuses and rasters a nanometre-sized electron beam across the sample surface [64]. The re-emitted electrons are collected by different detectors in each point which then forms individual images. Magnification is simply realized by a smaller area scanned during investigations. In principle, an **SEM** detects either low-energy secondary electrons (**SE**) or so-called back-scattered electrons (**BSE**) with broader energy distributions up to the primary energy used. **EDXS** can also be carried out to derive chemical information from the specimen. A problem in **SEM** is the penetration depth leading to mixed signals from the surface and the bulk depending on the primary electron energy and the specimen material. However, sample preparation is often simple by coating the specimen with a conductive layer, which is a huge advantage compared to **TEM**. Besides the disadvantage related to the convoluted surface information by depth, many samples also suffer from electron exposure. In our case we used **SEM** as a characterization technique for crystalline cellulose which turned out to be surprisingly stable under the electron beam concerning their morphology.

*Scanning electron microscopy was performed on a Gemini ULTRA 55 (ZEISS, Germany) and a Quanta 200 Environmental-**SEM** (FEI, The Netherlands) supported by Dr. Johannes Rattenberger, DI Thomas Ganner and DI Barbara Geier from the Institute for Electron Microscopy and Nanoanalysis and the Graz Centre for Electron Microscopy.*

4 Sample Preparation

As mentioned in the **AFM** sections, highest spatial resolution can only be achieved if the investigated areas are very flat. To be more specific, the lateral resolution strongly depends on the vertical feature heights due to the **AFM** tip geometry. It therefore follows that for accessing the molecular resolution the surface has to be nano-flat, which means surface roughness values of less than about 10 nm **RMS**. Furthermore, as outlined in the cellulose and enzyme section, a controlled internal structure by means of crystalline, amorphous and mixed properties is essential to study individual processes. The design and fabrication of such substrates was one of the main research goals in recent years. Mag. Judith Dohr, Timothy Aschl, and DI Thomas Ganner [8–10] first introduced the fractional solvent exchange cellulose (**FSEC**) material followed by the improved multiphase artificial cellulose substrates (**MACS**) [5]. Although successfully used in several studies and tunable as well as multi-phasic, the fabrication was rather time-consuming, the nano-flatness given only up to tens of micrometres and the crystal size control limited. Therefore, DI Stefanie Rošker and DI Thomas Ganner [10, 11] introduced the amorphous thin film cellulose (**ATFC**) which can easily be prepared via spin-cast processes followed by an acid-based conversion into fully amorphous, pure cellulose within less than 2 hours. The final step was the development of nano-crystalline thin film cellulose (**NCTFC**) which was then combined with the **ATFC** approach to fabricate a substrate which finally fulfils all demands: the semicrystalline thin film cellulose (**SCTFC**). The latter two approaches are the central element in this thesis while the formerly described materials are briefly introduced in the following [65].

4.1 Multiphase Artificial Cellulose Substrates – MACS

As described before, Avicel is not soluble in water. One of the few materials that can dissolve the highly crystalline Avicel source material is 1-N-butyl-3-methylimidazolium chloride **BMIMCl**, which is an ionic liquid or a molten salt (see Figure 26 a). The high acidic activity and concentration of chloride is capable of breaking the hydrogen bonds that tie together cellulose. Cellulose in **BMIMCl** were dissolved up to 15 wt.% and this concentration has been profoundly studied by Timothy Aschl [9]. In order to melt the ionic liquid it has to be heated up to 100 °C and has to be kept at this temperature for mixing for 24 hours. After mixing, some Avicel flakes are added to get a substrate that contains amorphous as well as crystalline cellulose. The resulting viscous and almost clear gel is then dried between objective glass slides separated by glass spacers to achieve a homogenous thickness (see Figure 26 b). The drying process takes one week, and later, the still present ionic liquid has to be removed by a fractional solvent exchange. This is done by washing the sample in H_2O/ethanol solutions with increasing ethanol concentration in multiple steps until in the last step only ethanol is used. The sample patches are stored in ethanol for further use (see Figure 26 c) until they can be cut into small pieces which are then embedded into epoxy resin (see Figure 26 d). When the resin has hardened, the sample is ready for ultramicrotomic cutting. First the resin block is made pointy at the position where the cellulose flake sits. Then some cuts normal to the block are performed in order to get the cross section flat for **AFM**. The last fine cut is done by a very sharp diamond knife which requires a lot of experience but then delivers a very flat surface at the embedded regions. The principle is easy to understand when looking at Figure 26 e. The resulting ultra-flat cut cross section is shown in a **SEM** image in Figure 26 f.

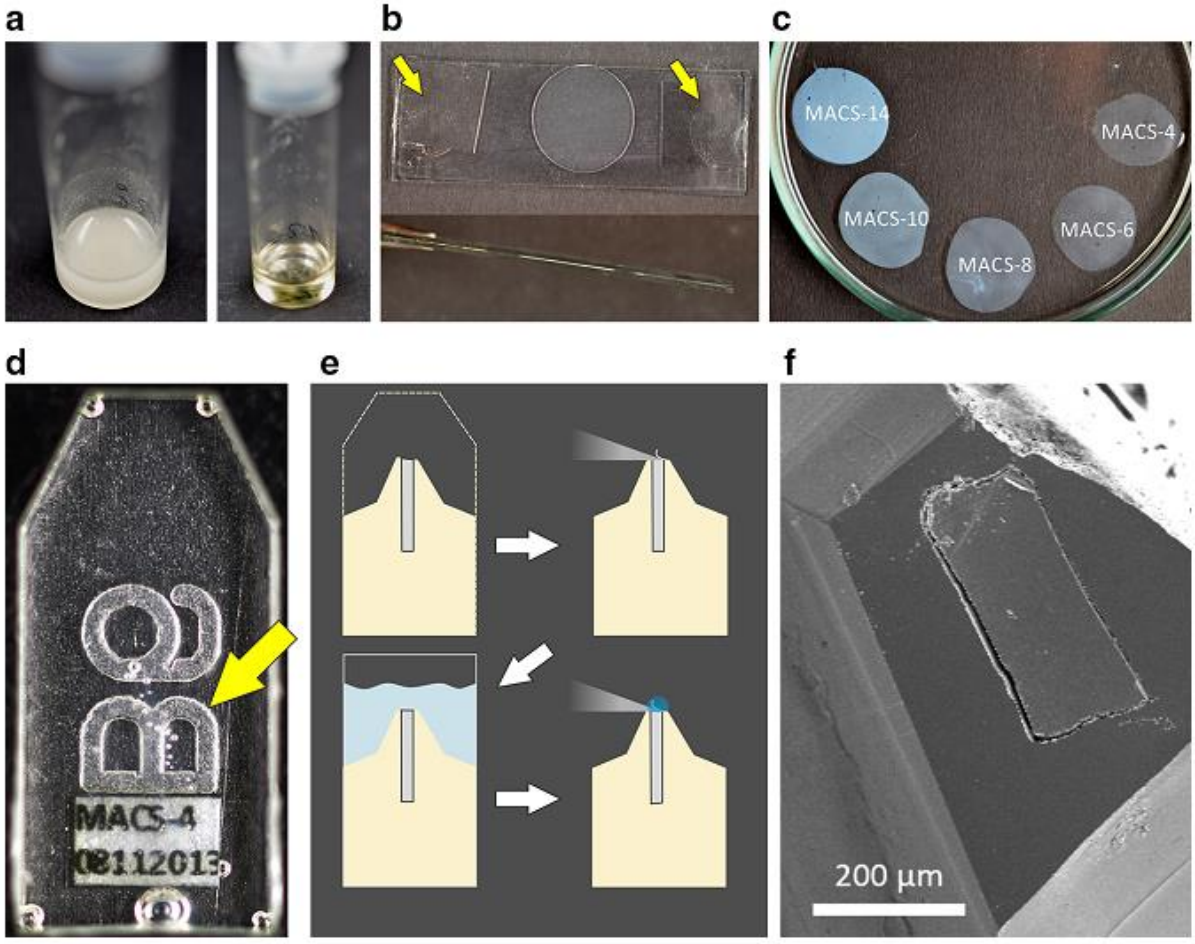

Figure 26: Shows a step-by-step procedure of MACS fabrication. It starts top left (a) with a solution of molten 1-Butyl-3-immidazolium chloride (BmimCl) as a solvent for cellulose. The resulting gel from 24 h mixing at 100 °C is then pressed immediately after mixing to a flat disc between glass (b). Glass spacers are used to create a uniform thickness (yellow arrows in (b)). After solvent exchange, MACS specimens are stored in ethanol (c), and with increasing crystalline content the transparency decreases. The specimen is cut with a sharp blade into small pieces which are then embedded in epoxy resin after they have been dried (d). To finally get an ultra-flat sample that can be investigated via AFM, a microtome preparation has to be carried out, which is schematically illustrated in (e). The product is shown in (f) imaged via SEM [5].

In former theses, this substrate is referred to as **MACS** [5, 8–10] where a tune ability of the crystalline content up to 25% could be demonstrated. For this thesis, we used a crystal content of 17% which is further called **MACS17**.

*The **MACS17** samples used for the investigations in this thesis were prepared by DI Thomas Ganner. Ultramicrotome preparation via an EM UCS-NT (LEICA, Germany) were performed by Ing. Claudia Mayrhofer at the Graz Centre for Electron Microscopy.*

4.2 Spin-Cast Preparation

Thin film preparation by spin cast is a conventional way to obtain thin, homogenous films. Depending on the spin parameter and the solvents used, thicknesses down to monolayers and below can be fabricated. For that, a small droplet of the relevant solution is placed on a sufficiently flat substrate like Si-wafers. Starting the spin-cast process leads first to the formation of a homogeneous film which then

evaporates dependent on the boiling point of the solvent used. Although a little difficult to handle, this method allows for very homogenous layers in a very reproducible way. For this thesis, we always used Boron doped Si wafers with a 3 nm SiO_2 top layer pre-cut to 10 x 10 mm^2 size. Each substrate was taken out of a sealed wafer box, cleaned with isopropanol soaked lens paper, dried with dry CO_2 spray, and immediately subjected to spin-cast preparation in a laminar flow box. By using this preparation method, DI Timothy Aschl, DI Thomas Ganner and DI Stephanie Rošker [9–11] succeeded in the fabrication of the **ATFC** substrates which provided surface roughness around 1 nm (**RMS**) on large areas above 100 x 100 μm^2. The detailed procedure is described in 6.3.2 due to the much more appropriate position for a fluent discussion.

5 Strategy Overview

The first part of this thesis was a top-down approach from cellulose source materials towards nanocrystalline cellulose (**NCC**) particles. Those particles were then investigated via **AFM**, **SEM** and **TEM** and further characterized with **XRD** and **RAMAN** spectroscopy. These **NCC** particles were then combined with thin film cellulose layers (**ATFC**) which have been developed in previous studies at the institute. The combination of both then allows the fabrication of semicrystalline thin film cellulose **SCTFC** with tunable **NCC** concentrations for enzymatic degradation experiments as a main outcome of this thesis. With the advantage of the new FastScanBio **AFM** it was possible to perform in-situ investigations on the thin film substrates in real time (please note; Related videos can be found on the digital storage devices that comes with this thesis). Experiments with **CBH1** and **CBH2** in sequential order were performed to investigate individual effects. Together with supernatant (**SVG**) experiments, the applicability of **SCTFC** substrates as close-to-nature materials was successfully proven. In addition to these well-understood model enzymes, a rather new enzyme – swollenin (**SWO1**) – was tested on existing **MACS** substrates and compared to **NCC** materials. These investigations should clarify the role of isolated swollenin on cellulose, and possible synergistic effects in the presence of **SVG** supernatants. Figure 27 summarizes the thesis activities for a visual overview.
As will be summarized at the end of this thesis, the successful development of **SCTFC** substrates closes the substrate activities at the institute as it completes the demand for very different substrates. A cellulose substrate toolbox has therefore been developed allowing for specific substrate selection depending on individual degradation experiments.

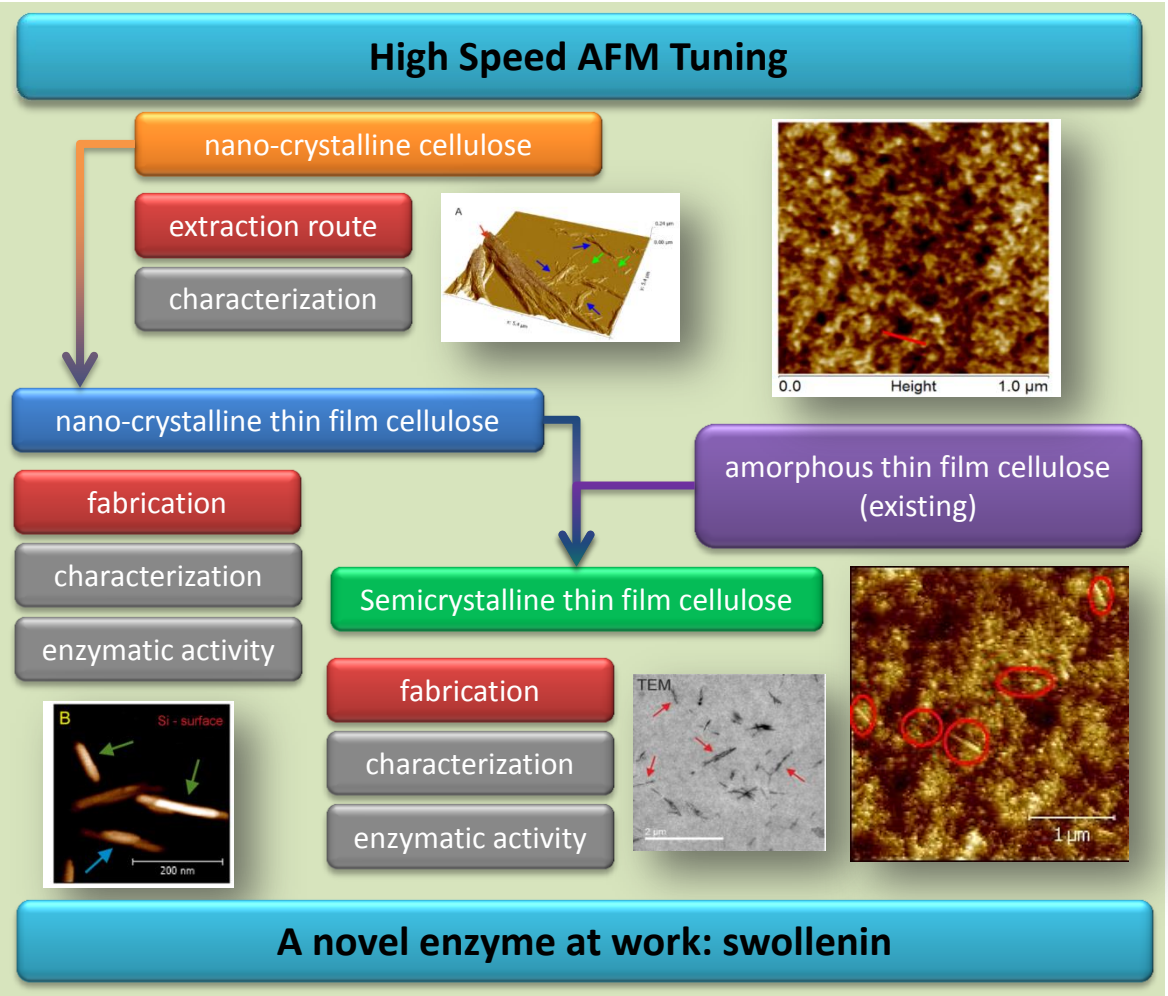

Figure 27: Overview of cellulose-based substrate development including existing (orange) and new (green) approaches presented in this thesis. Yellow symbols indicate enzyme experiments while purple boxes summarize according to characterization.

6 Experiments

6.1 FastScan Bio – Introduction

As this thesis was carried out with a new instrument (FastScanBio — **FSB**) at the institute, the first step of an in-depth study of the capabilities was needed as an integral part of this thesis. A picture of the device is shown in Figure 28.

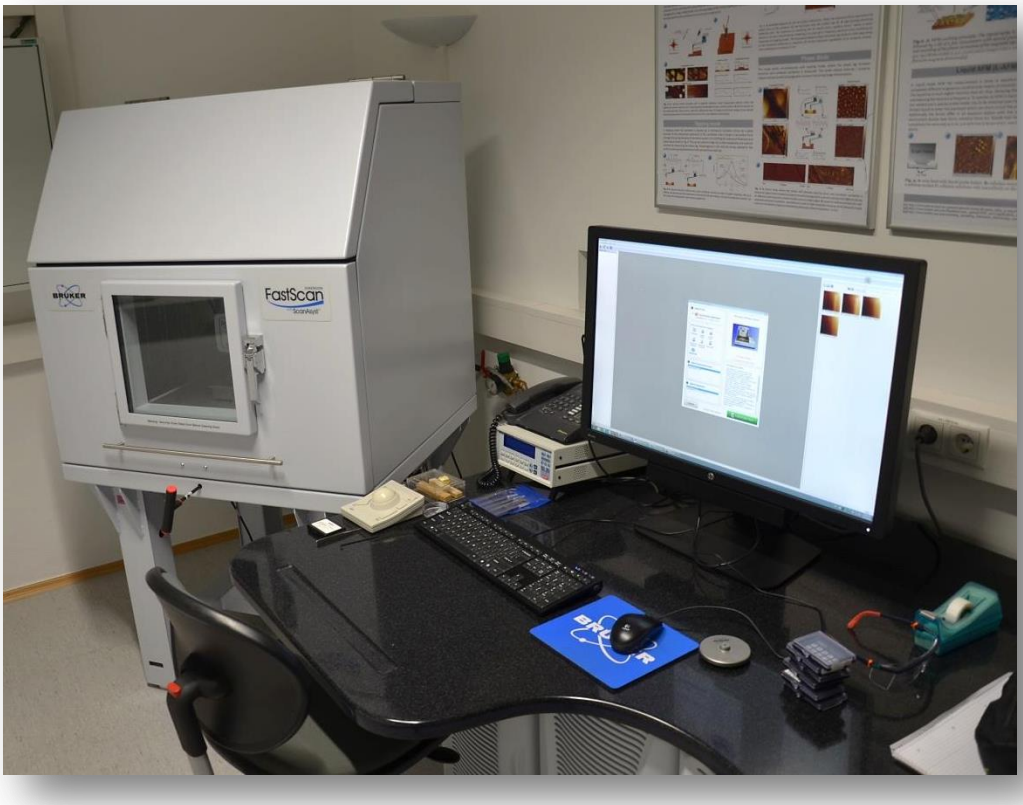

Figure 28: Workstation with the FastScanBio (FSB) at the Institute for Electronmicroscopy and Nanoanalysis.

This state-of-the-art **AFM** is specially designed for fast scanning in liquid environments, which makes it the perfect tool for biological experiments. Because the hardware and software had changed compared to the older Dimension 3100 **AFM** we had to perform some experiments to become familiar with this new device in order to explore the limitations. In more detail, we used the **FSB** performance in combination with our previously used liquid sample holder. The technical setup is shown in Figure 29 where all components are indicated. The results were initially compared to previous results as discussed in the following subsections.

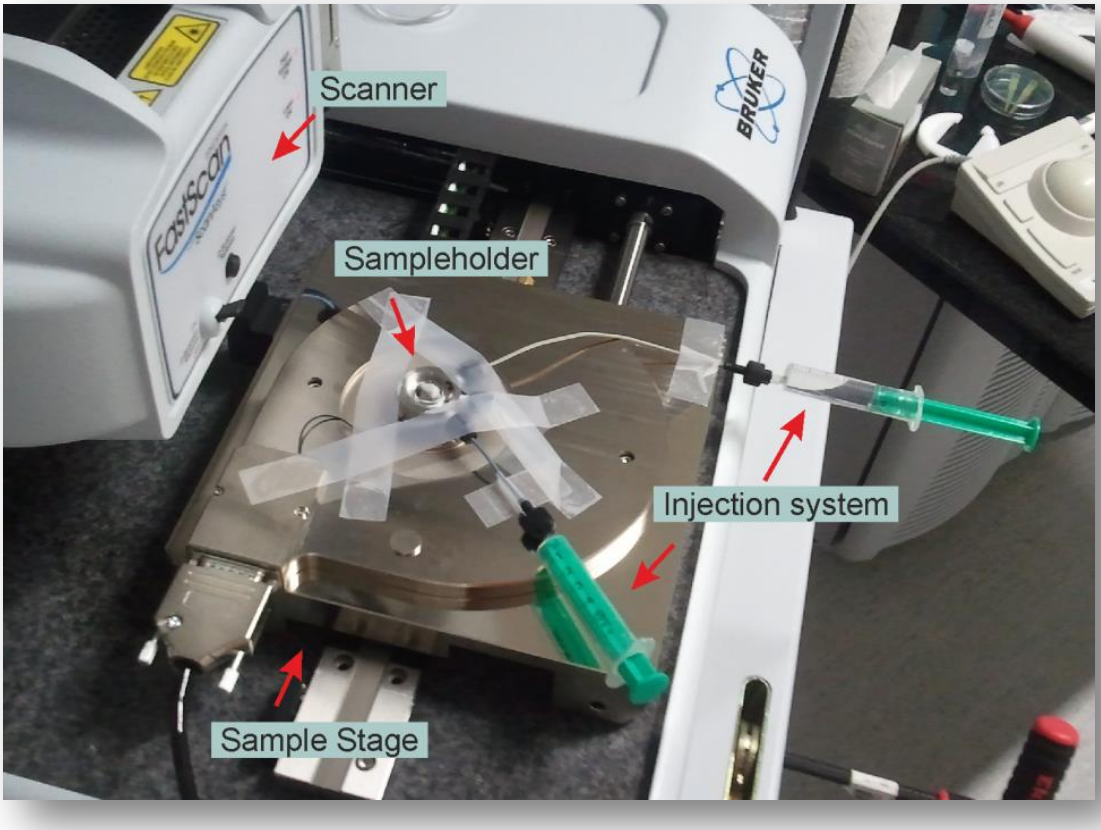

Figure 29: MACS sample holder installed on the sample stage of the FastScan Bio AFM.

6.1.1 Comparison to Dimension 3100

A major problem when working with the Dimension 3100 in liquids was sample drift. The **FSB** has, on the one hand, a very stable and soundproof enclosure and on the other hand, an active stage drift correction controlled by the software. This leads to very stable sample images which make interpretation and comparison much easier. The next thing that has changed is how the **PSD** is calibrated. With the Dimension 3100 most of the calibration had to be done by hand using mechanical screws. The operator had to switch between the computer and the Dimension 3100 instrument for full calibration. At the **FSB** everything is controlled via software and almost every step can be done automatically which makes it possible even for unexperienced users to calibrate the system when changing the cantilever. To put that into numbers, a change of the cantilever with the Dimension 3100 for an experienced user takes from 15 to 30 minutes while less than 5 minutes are needed at the new **FSB**. As laser positioning and boundary calibration is crucial when aiming for high-resolution imaging, the **FSB** advantages are essential for high reliability when approaching the molecular scale during imaging.

6.1.2 Software

The FSB software is also an enormous step forward. As shown by a screenshot in Figure 30, there is a workflow bar on the left side which guides the user step by step towards the real experiment. In a column next to the workflow a list of parameters appears before and during the scan process. In the middle, the main window shows the present workflow part which is active. In the case of the calibration, a live picture of the cantilever tip with adjustment options to the left of it is shown.

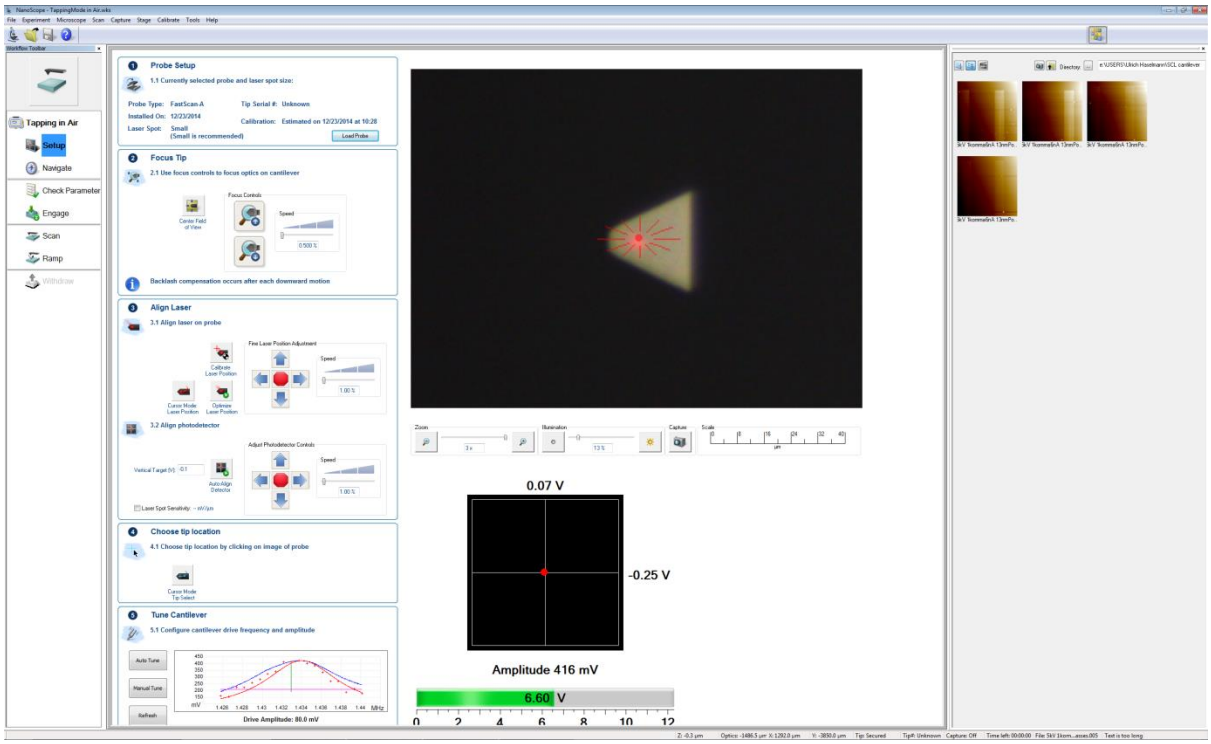

Figure 30: Overview of the new Nanoscope 9.1 software. In the left column a workflow is guiding the user through an experiment and the "Setup" step is selected. In the middle (main frame) the tip setup shows a well-calibrated "FastScan A" cantilever. In the right column the browser shows the record folder where thumbnails of recorded pictures are presented to the user.

6.1.3 Performance – Scan Rate

Without wishing to anticipate the results of the performance experiment, it is fairly easy to say the FSB does what it promises. The scan rate is increased a lot compared to the old dimension 3100 system. To show this in an easy illustration Figure 32 shows **AFM** height images of an **ATFC** sample. The scan size was 1 x 1 µm² and the investigation was done in a liquid environment with a Fast Scan DX shown in Figure 31. The scan speed increases, starting with 0.02 fps (frames per second) and rises to 0.5 fps in images A to D in Figure 32 respectively. With this test the very high resolution is demonstrated. Indicated with red arrows in image A are microfibrils in sub-10 nm. This resolution is not lost as the scan speed is increased. This was one of the first experiments with the new **FSB** and showed that the instrument can keep up stats promised by the developer.

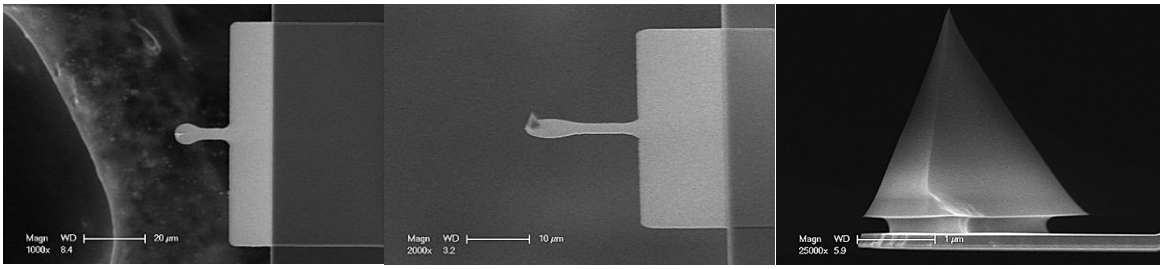

Figure 31: Cantilever Fast Scan DX from Bruker showing SEM images from the front end of the cantilever (left and middle image) and the tip (right image) [50]. The spoon-like shape is able to reflect enough light from the laser, while the smaller neck provides a very low spring constant for better imaging of soft material.

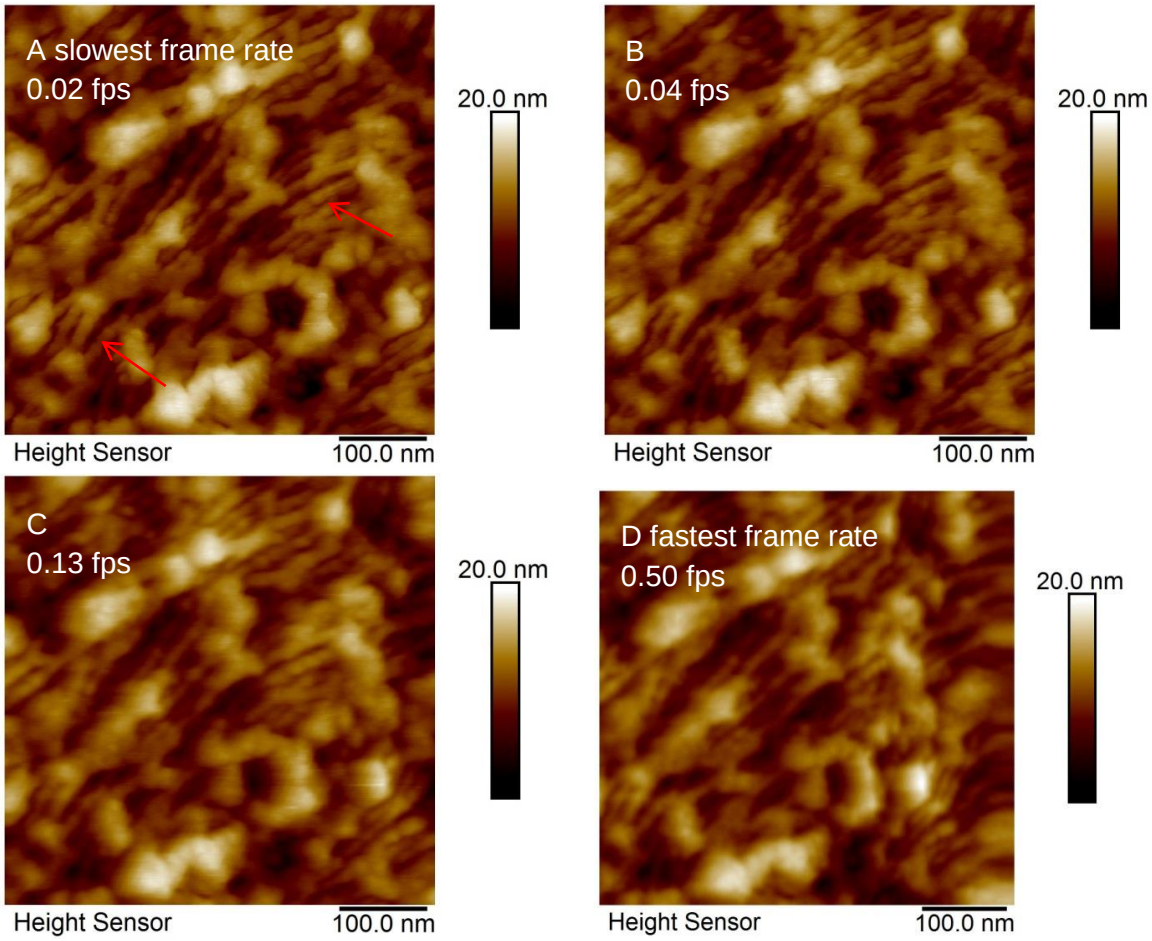

Figure 32: ATFC substrate imaged via AFM in liquid at different speeds (slowest A to fastest D); the frame rate is given in fps (frames per second). The very high resolution shows cellulose fibrils in sub-10 nm (red arrows in A). Even at a imaging speed increase of 25 times (A compared to D) the high resolution is not lost.

For our future purpose concerning enzymatic degradation studies we need an instrument which provides high-speed imaging. The Dimension 3100 had the disadvantage that we were very limited in scan speed. Therefore, it took many hours to acquire a few images. Bruker however promised that the **FSB** can provide far more images in less time without losing image quality, which can be observed in Figure 32. To quantify how fast the **FSB** can operate we used a SiO_2 reference sample and the recommended high-speed cantilever Fast Scan A as shown in Figure 33 and Figure 34 B respectively.

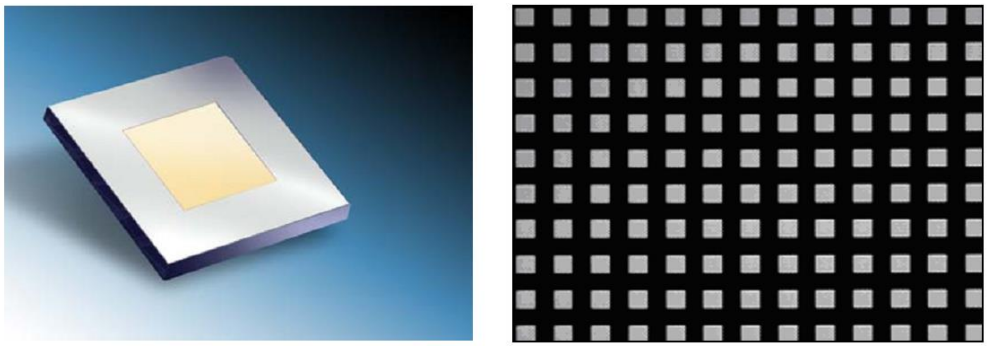

Figure 33: Silicon reference sample STR10 from VLSI Standards. Illustration of the 8 x 8 mm² sample (left) and right an illustration of pit pattern on the sample (right). The pit size is 1.2 x 1.2 µm² [66].

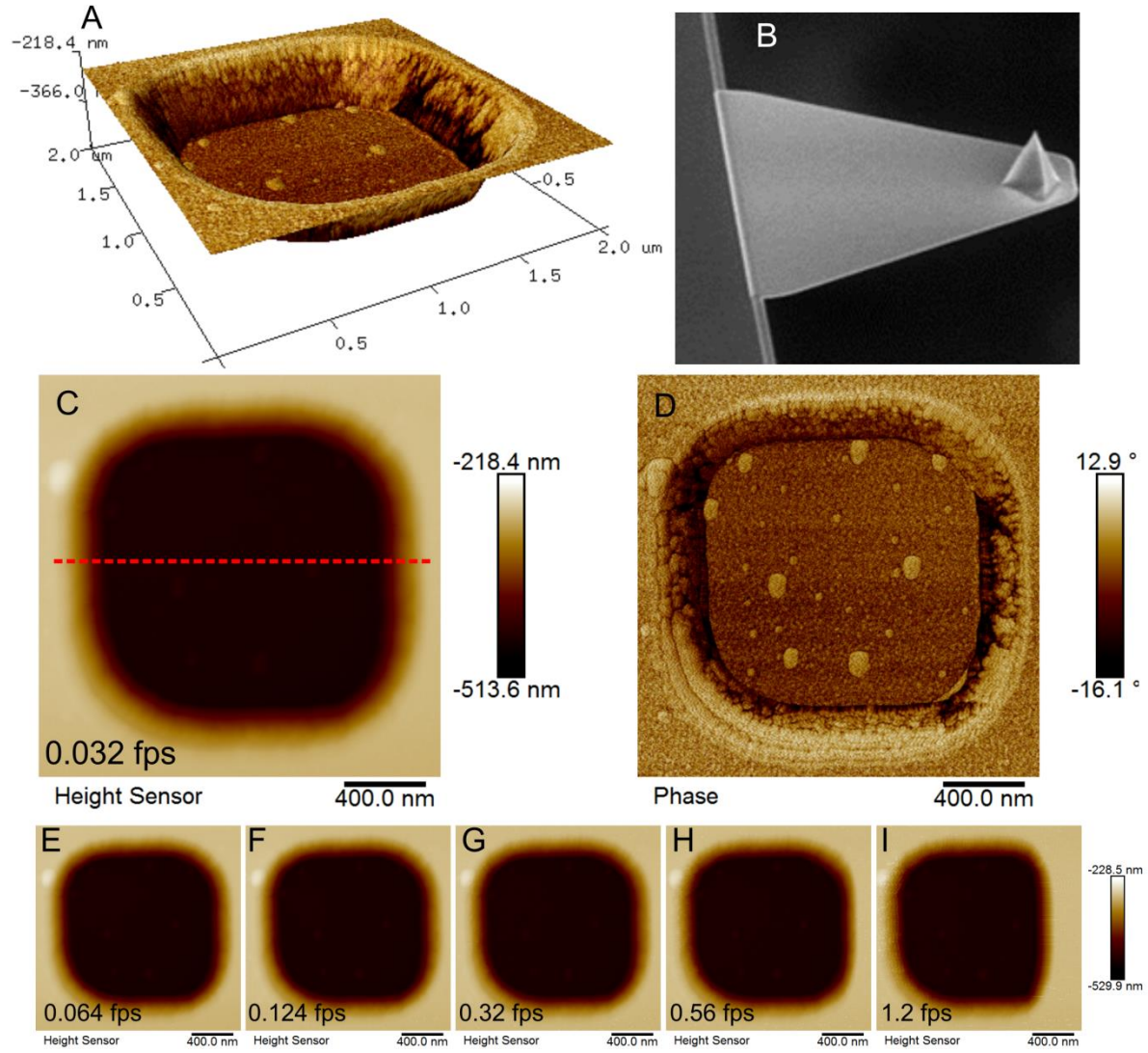

Figure 34: Performance test on silicon reference sample. A: AFM 3D image with phase overlay corresponding to C: Height and D: Phase image of one pit on the silicon reference sample. B shows a SEM image of the FastScan A cantilever tip used (from http://www.brukerafmprobes.com). E to F show images taken for performance evaluation. All images have a scan range of 2 x 2 µm² and the reference line measured to calculate the accuracy was taken in all images represented by the red dashed line in image C.

The background of this high-speed capability is the high resonance frequency realized by the small cantilever dimensions. Typically, these resonance frequencies lie in the range of 1.4 MHz for high-

speed air imaging compared to 300 kHz previously used with the Dimension 3100 platform. The triangular end of the cantilever is very small in Figure 34 B and therefore a very small laser spot is needed that only the **FSB** has. To evaluate the achievable frame rates, we started at a scan speed that was close to the limit for reasonable imaging with the Dimension 3100. An **AFM** image at this frame rate is shown in Figure 34 A as 3D (combines height with phase image as overlay), C as height and D as phase image. Next, we increased the scan speed step by step until the resulting image was not sharp any more (see Figure 34 E to I). Images were taken with 256 x 256 pixels. Only the scan speed was altered, and all other parameters were kept constant. This experiment was repeated for 2 µm, 5 µm and 10 µm scan-sized images. In Figure 35 the results are shown. Notice that in the graph the frame time is plotted rather than the scan speed. The reason for that is simply a more intuitive understanding of frame time (how long does it take to acquire one image?) than scan speed (µm/sec.). The right y-axis shows the frame time for the 10 µm images, and the left y-axis corresponds to the frame time of 2 µm images. A linear plot from left to right would give the frame time for the 5 µm images. The green shaded area indicates a frame time that results in accurate images. The yellow area indicates images that are not accurate any more, but could be accurate again if other parameters like tip force were altered. The red shaded area indicates frame times that are simply too fast for accurate imaging. The fastest image with accurate topographical information within the image was taken at 2 µm with a frame time of 1.7 seconds. This is a very good and promising result, because if we used a smaller scan range, faster imaging would be possible. Also this experiment was performed in air, which is – compared to liquid environments – the worst condition to make fast scans. This originates from the fact that in liquids the fluid-related damping is even higher, which enables faster tracking adaptions by the software.

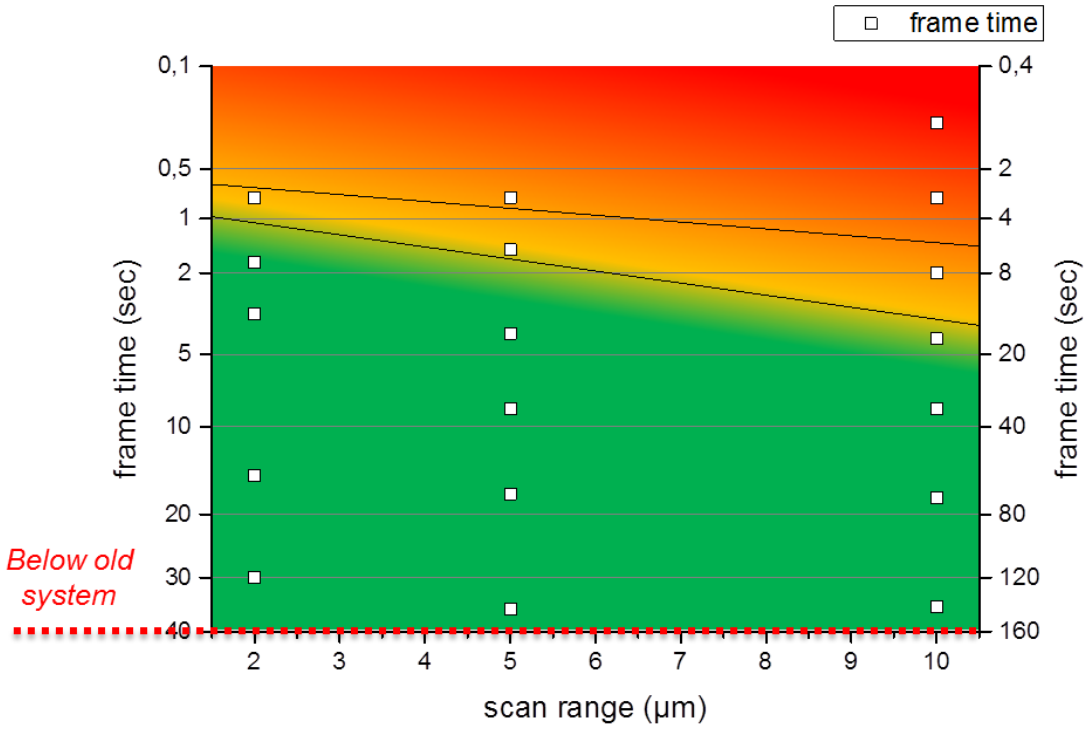

Figure 35: Diagram showing the results from the performance test of the Bruker FastScan Bio in air. Below the red dotted line would be the maximum speed of the Dimension 3100. Left y-axis corresponds to frame times of 2 µm images and right y-axis indicates frame times of 10 µm images. 5 µm images have frame times linear between both y-axes. The white squares show frame times acquired from images. The green shaded area means all images inside are

accurate. The red shaded area results in non-accurate images. The yellow shaded area means that here other parameters than the scan speed could be altered to achieve accurate imaging results.

To summarize these performance tests it can be stated that the new **FSB AFM** can achieve frame rates of less than 1 second in air and close to 2 seconds in liquids (≤ 2 µm scan range). This is an improvement factor of around 250 compared to the previous capabilities, which demonstrates the enormous step forwards in the field of real-time investigations.
Together with the other benefits described in the previous subsections, it is evident that the **FSB** platform is a very decent and reliable instrument, which features easy to use and automated calibration with a well-structured software that can squeeze out the high speed and excellent imaging quality of the instrument. All this comes with high resolution and a micro-volume cell, which is specially designed for bio-applications in liquid environments.

6.1.4 Performance – Dynamic Temperatures

To test the instrument's heating capabilities, a dynamic degradation experiments was set up. For that, previously developed **MACS** materials were used in combination with the liquid holder (see Figure 29) and a very soft Fast Scan DX probe (see Figure 31). The heater chuck of the **FSB** is shown as schematics in Figure 36. The Lakeshore temperature stage was set up to 40 °C and the temperature was controlled via a loop-back system using two sensors, one in the heating stage and one attached to the sample holder.

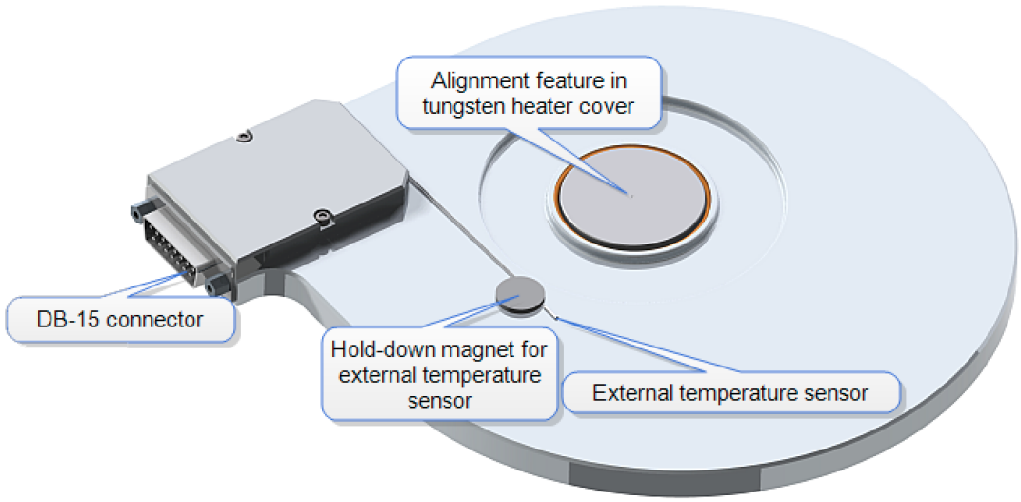

Figure 36: Schematics of the heater Chuck from the FSB [50]**.**

After a stable temperature was reached, the surface was first scanned without enzymes as reference and then incubated with **SVG**. Measurement parameters were resolution 1024 x 1024 pixels, scan range 10 x 10 µm² and frame rate 0.37 frames per minute. The results are summarized in Figure 37 and consistent with previous results [10]. First a very slow degradation is observable in the graph top left followed by rapid degradation after 1.5 h. Corresponding **AFM** images are given top right at all time points, which visualize the successive local degradation. In particular, the crack formation is observed in agreement with previously postulated degradation models [6]. The cross sections at the bottom in Figure 37 give individual cross sections along the dashed lines in the **AFM** images top right. The gradual degradation is clearly visible together with the fact that larger crystals are much

less affected. Although it is not in the scope of this section, the latter fact clearly demonstrates why a size control would be highly needed for enzymatic degradation experiments to prevent height variations of several 100 nm, which prevents high-resolution imaging towards the molecular scale. Please note: A short clip of this experiment can be found on the data-media file with the name: *"File 1 – Degradation of **MACS17** by **SVG** at 40 °C.mp4"*.

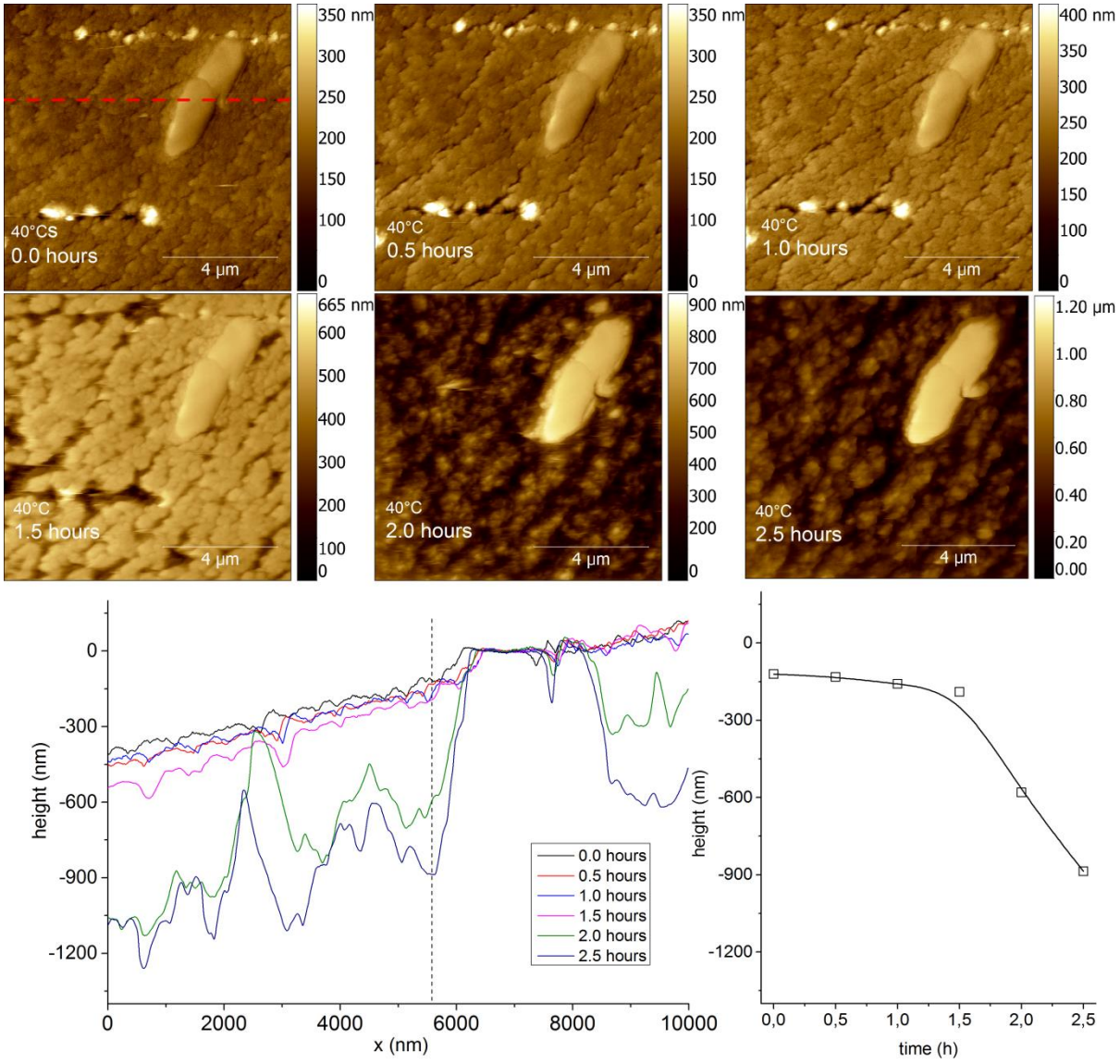

Figure 37: Degradation experiment conducted via AFM at 40 °C. A MACS substrate with a crystalline cellulose content of 17% was degraded with SVG. The AFM images in the top were taken at 0.37 fpm and show height images taken at certain times ranging from start 0.0 hours to 2.5 hours. The graph below left show line segments of each picture representing the red dotted line in the first picture. The graph below right shows the height loss at the dotted line from the top graph.

It can therefore be concluded that the high-speed capabilities are still available at elevated temperatures which is essential for comprehensive experiments. Besides the higher temperature increasing as expected, the degradation velocity v_d = 8 ± 3 nm/min with a factor of 10 times faster degradation compared to degradation at room temperature is v_d = 0.8 ± 0.3 nm/min [11].

6.2 Substrate – NCC

Before we consider the fundamental studies on the smallest cellulose crystallites, a short overview of previous activities is provided as they are an integrative part of this thesis. This provides a general picture of the idea which is substrate toolbox for specific in-situ bio-experiments.

6.2.1 Motivation

In 2009 the research on new substrates for fundamental cellulose studies started with the idea to improve the knowledge about cellulose as a source for second-generation biofuels. Second-generation biofuels are those that do not use raw material that could be used for food generation. Nowadays this topic is fuelled by the fact that global warming is immanent and the demand for carbon dioxide-neutral fuel will grow in the future to stop the rise in atmospheric carbon dioxide concentration. Therefore this research project is more important than ever.
So far, this research project has led to the **MACS** substrate (master's thesis of Mag. Judith Dohr, DI Timothy Aschl and DI Thomas Ganner [8–10]) and the recently successful development of **ATFC** substrates (master's thesis of DI Stephanie Rošker [10, 11]). All this research was carried out in cooperation with the Institute of Biotechnologies (**TU Graz**) led by Prof. Dr. Bernd Nidetzky. The intention back then was to close the gap between dynamic biochemical experiments and localized microscopy images which are mostly static. The information gathered via dynamic localized methods like **AFM** would give a much deeper insight in real time which was widely missing at that time.
The years of collaboration put the institute into a unique situation worldwide, which is based on two facts: ***1)*** demonstration of single enzyme imaging as shown in Figure 38 (single enzymes on rod-like cellulose nano-crystallites are indicated by green arrows); and ***2)*** the development of suitable substrates as a decisive element to enable point 1. The latter point turned out to be a major research topic at the **FELMI-ZFE** during recent years. A major issue with previously developed **MACS** materials was the lack of control concerning the cellulose crystals. This was the starting point of new activities with the aim of very flat surfaces with a controlled content of homogeneously large nano-crystals. DI Stefanie Rošker worked on the development of a fully amorphous cellulose substrate with nano-flat surfaces (**ATFC**) in detail. At the same time, DI Thomas Ganner successfully carried out the proof of concept concerning the fabrication of **NCCs** based on hydrolysis of filter paper with sulfuric acid [67]. The detailed characterization of the latter approach is part of this thesis and is described later. The main intention of this thesis was now to bring both the **ATFC** and the **NCC** together, which should fulfil the high expectations of a fully tunable but close-to-nature substrate.
In the following, the **NCC** fabrication is discussed in detail followed by the successful combination with **ATFC**. Finally, these new materials are then tested with model enzymes to prove their applicability for **AFM**-based in-situ studies in real time.

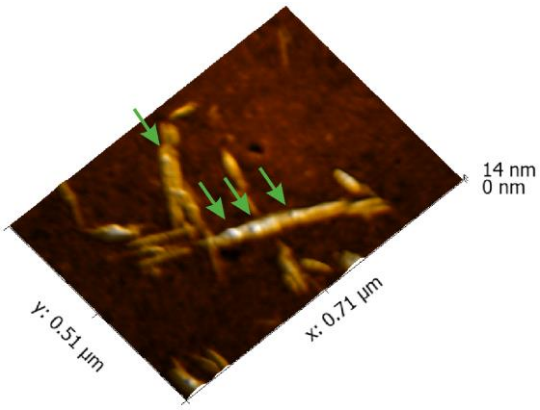

Figure 38: 3D AFM image showing rod-like NCCs with single enzymes on top, indicated by green arrows.

6.2.2 Synthesis of NCC

In order to extract crystalline parts of cellulose, a special type of preparation is used which yields the smallest crystalline units of the elementary cellulose fibril. Following literature protocols, we used acidic hydrolysis of conventional filter paper (with 100% cellulose content) to extract nano-crystalline cellulose [67], which are also referred to as cellulose nanowhiskers. This small needle-like and highly crystalline cellulose particles will then be used to fabricate a new type of substrate: the **SCTFC**.

To achieve that, cellulose from Whatman no. 1 filter paper is cut into small (1 x 1 mm²) pieces and put into 64 vol.% sulfuric acid at 45 °C for 45 minutes. The reaction is stopped by a 10-fold dilution with deionized water. Acidity of the solution is further reduced by multiple steps of centrifugation until a pH of greater than 1.5 is reached. To prevent cellular growth 0.1% sodium azide (NaN_3) is added to the solution and is stored in glass bottles as solution in a refrigerator until further use.

For characterization purposes, samples were not only taken at 45 minutes of hydrolysis. At 15, 30, 60, 90, 180 and 240 minutes smaller batches were taken. In order to differentiate between those batches in this thesis, the time is added as a number after **NCC**. For example **NCC** from the batch that was taken after 15 minutes is called **NCC15**. Please note that batch **NCC45** had a very dim supernatant after centrifugation so we also kept this batch and named is **NCC45ü**. We noticed that **NCC** tends to precipitate out of the solution if the batch rests for more than one day in the refrigerator. This was especially the case for all batches taken before 45 minutes of hydrolysis. Therefore homogenization prior to the investigation of the final solution via pulsed sonication for at least 1 minute is important to get reproducible results from characterization, otherwise **NCC** would agglomerate and form large clusters like a haystack, as in Figure 39. The **NCC** solutions have a concentration of 4.6 ± 0.3 g/l.

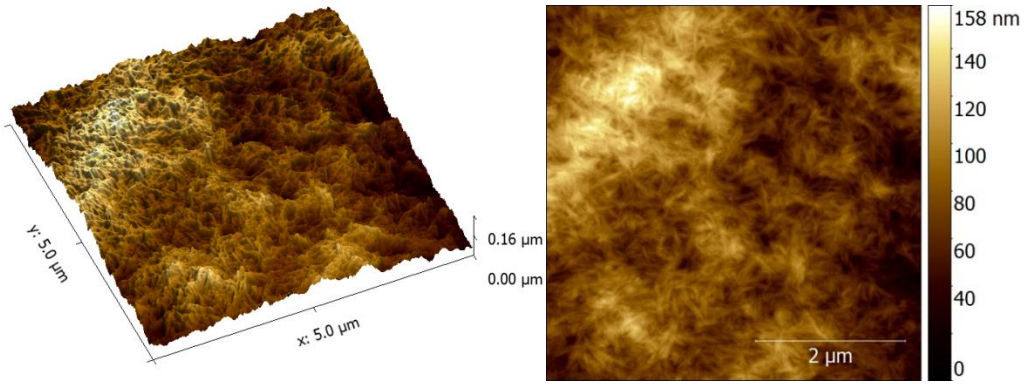

Figure 39: Agglomerated NCC as 3D AFM image left and right the corresponding height image.

6.2.3 Size Distribution of NCC

For the determination of size distributions, **NCTFC** substrates with **NCC15**, **NCC30**, **NCC45**, **NCC45ü**, **NCC60** and **NCC240** were spin cast on 10 x 10 mm² silicon wafers. Prior to preparation, the **NCC** solution was diluted 4 times with H_2O and was pulsed-sonicated for 1 minute because this concentration gives well-distributed thin films for investigation and **NCC** tends to agglomerate. Silicon wafers for spin cast were stored in 20 wt% potassium hydroxide (KOH) solution for 3 minutes. KOH etches the silicon wafer surface and makes it hydrophilic [68]. In a final step, substrates were cleaned via isopropanol and lens paper and dried with dry CO_2 gas. This method was needed to create a hydrophilic surface so that hydrophilic **NCC** adhered better when spin cast. Otherwise **NCC** would not stick to the surface of the Si-wafer. Typically, spin-cast parameters of acceleration to 3900 rpm in 4 sec and spinning at 50 sec at 3900 rpm. Samples created in this way are called nano-crystalline thin film cellulose (**NCTFC**) and appear to be blank silicon wafer, but **AFM** reveals the tiny crystallites which will be demonstrated in the experimental part of this thesis. Sometimes a small layer of H_2O can remain on the surface, which makes measurements in air rather complicated. To avoid that, the **NCTFC** sample can be stored at 80 °C for some time – at least 1 hour to remove any H_2O stuck. Those samples were then investigated via **AFM** and analyzed via the software Gwyddion [46, 47]. Figure 40A gives an **AFM** overview to get an impression of the film morphology. A closer look is given in Figure 40B showing the typical rod-like cellulose crystallites. As can be seen there is an affinity towards each other, which sometimes forms lateral or vertical **NCC** stacks as indicated by arrows. To provide statistically relevant data, at least 8 images as shown in Figure 40A were taken from each batch at the highest possible image resolution of 4096 * 4096 pixels at a scan range of 10x10 µm.

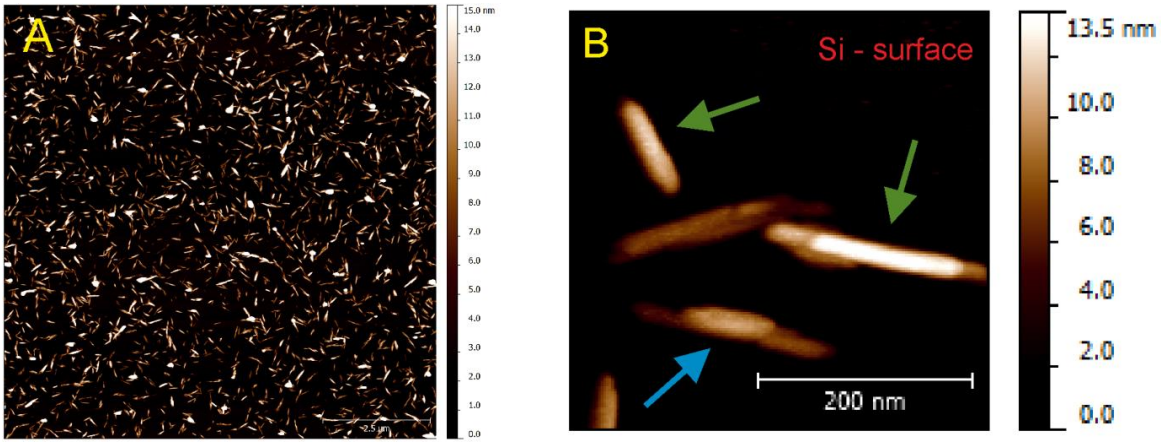

Figure 40: AFM height image, original image in high resolution (A) and a zoom in detailed image (B). Silicon surface in the background (black) as level zero and single NCC (green arrows) and two NCC sticking together (blue arrow).

Those images were then analyzed in detail with regard to their heights and lengths. The related error has been estimated to be below 5 nm, giving the statistics high relevance. Figure 43 gives the results concerning their lengths (left) and widths (right) together with their contribution for all batches at the same x-axes for direct comparison. Each plot consists of at least 200 individual grains followed by Gaussian fits (black line). The numerical results are summarized in Table 3. The first thing to notice is the decreasing size of the crystallites for increasing reaction times as expected. However, the observed length and widths shift of 250 nm → 130 nm and 30 nm → 20 nm, respectively, are comparably small, especially considering the strong increase of process times. The second detail to be mentioned

is the slightly higher values for **NCC30** and **NCC45** against the general trend. To determine whether this is real or an **AFM** artefact, the same samples were coated with a 10 nm iridium layer via chemical vapour deposition and subjected to **SEM** investigations as representatively shown in Figure 42.

Table 3: Results with size distribution of NCC grains from different reaction times. Left columns AFM data compared to right columns with SEM data.

AFM			SEM		
length					
	mean	stdv		mean	stdv
	[nm]	[nm]		[nm]	[nm]
NCC15	192.9	105.4	**NCC15**	251.6	107.9
NCC30	269.1	139.7	**NCC30**	233.9	93.6
NCC45	275.3	10.5	**NCC45**	225.6	76.8
NCC45ü	158.6	84.9	**NCC45ü**	147.1	58.1
NCC60	216.1	87.8	**NCC60**	192.9	64.9
NCC240	163.4	66.5	**NCC240**	126.9	51.9
Width					
	mean	stdv		mean	stdv
	[nm]	[nm]		[nm]	[nm]
NCC15	31.7	16.4	**NCC15**	30.6	9.5
NCC30	58.4	22.3	**NCC30**	28.6	7.9
NCC45	65.5	21.3	**NCC45**	27.3	7.8
NCC45ü	24.8	11.6	**NCC45ü**	20.3	5.7
NCC60	35.0	12.1	**NCC60**	29.6	8.7
NCC240	31.4	9.4	**NCC240**	18.7	5.5

The images have been analyzed giving the statistical results shown in Figure 44 for lengths and widths on the left and right, respectively. The first thing to notice is the general agreement with **AFM** data as summarized in Table 3. In particular, the absence of the increasing trend for **NCC30** and **NCC45** can be seen, which allows for the conclusion that **AFM** data seems to be convoluted by a dull tip. Figure 41 A and B give the **NCC** lengths and widths, respectively, versus the process times, which shows a trend of smaller grain lengths the longer the reaction time, while the width is only a little reduced. A final detail is the result of **NCC45ü** (supernatant batch), which forms very fine grains as a consequence of the final centrifugation during preparation. Due to the comparably small-sized variation observed for different process times, further experiments in this thesis have been carried out using **NCC45** batches. These crystals have lengths and widths/diameters of 225 ± 76 nm and 20 ± 5 nm, respectively. Although discussed later in this thesis, it should be mentioned at this point that correlated **SEM** and **TEM** imaging revealed practically the same **NCC** width distributions, which justifies the comparably small error of **AFM** investigations and therefore supports the numbers specified above.

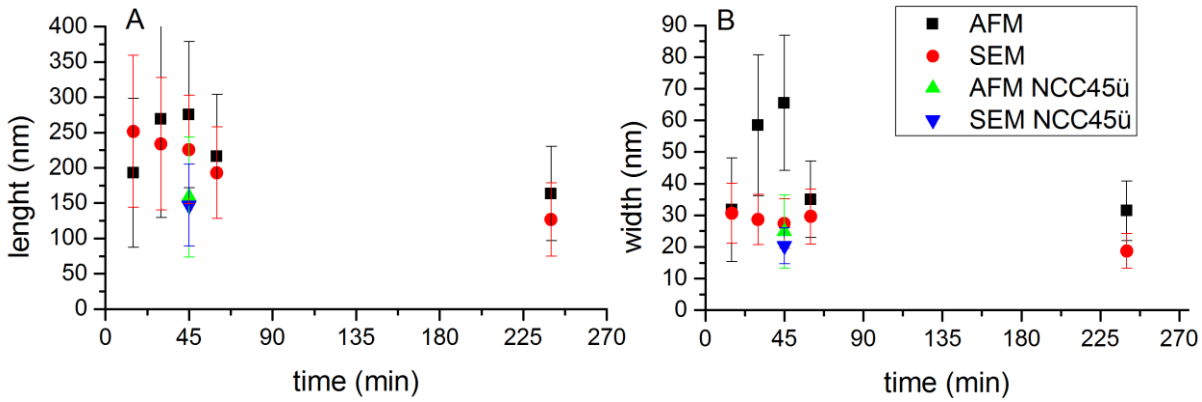

Figure 41: Size distribution of AFM (black) and SEM (red) versus the process time. A: length and B: width. NCC45ü are marked extra AFM (green) and SEM (blue).

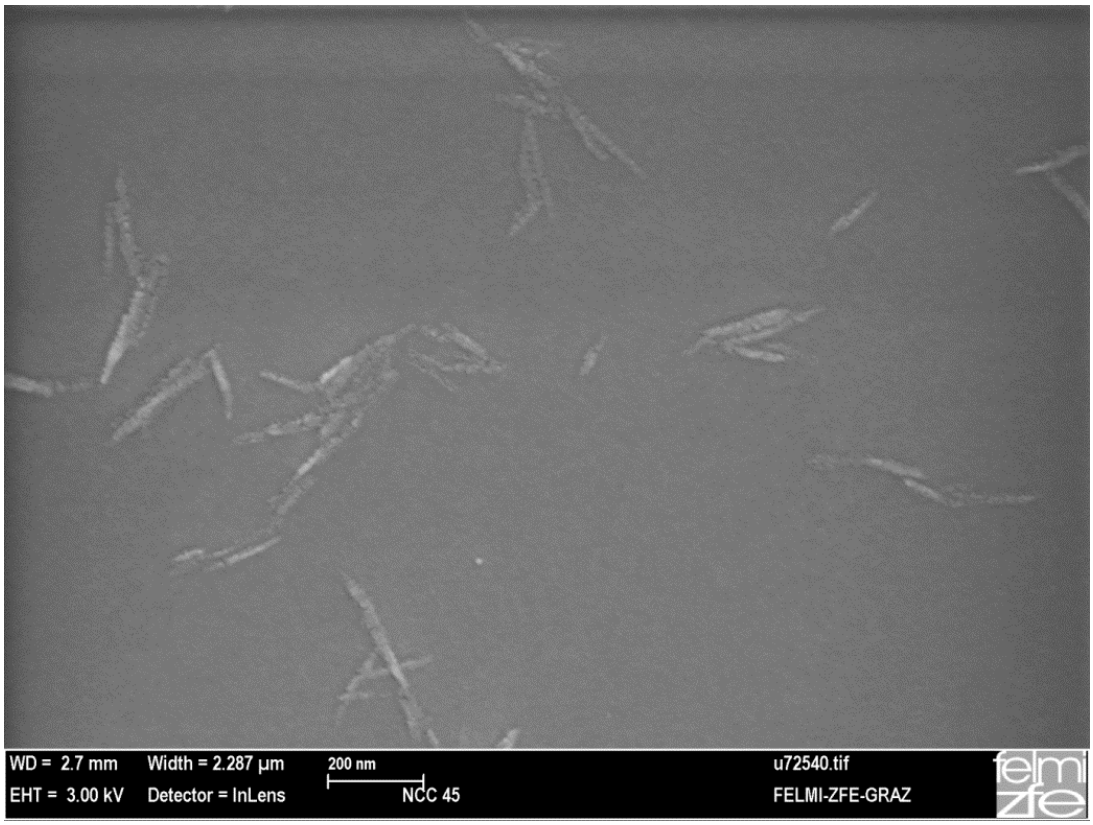

Figure 42: Sample NCC 45 image via SEM as a comparison to AFM size distribution.

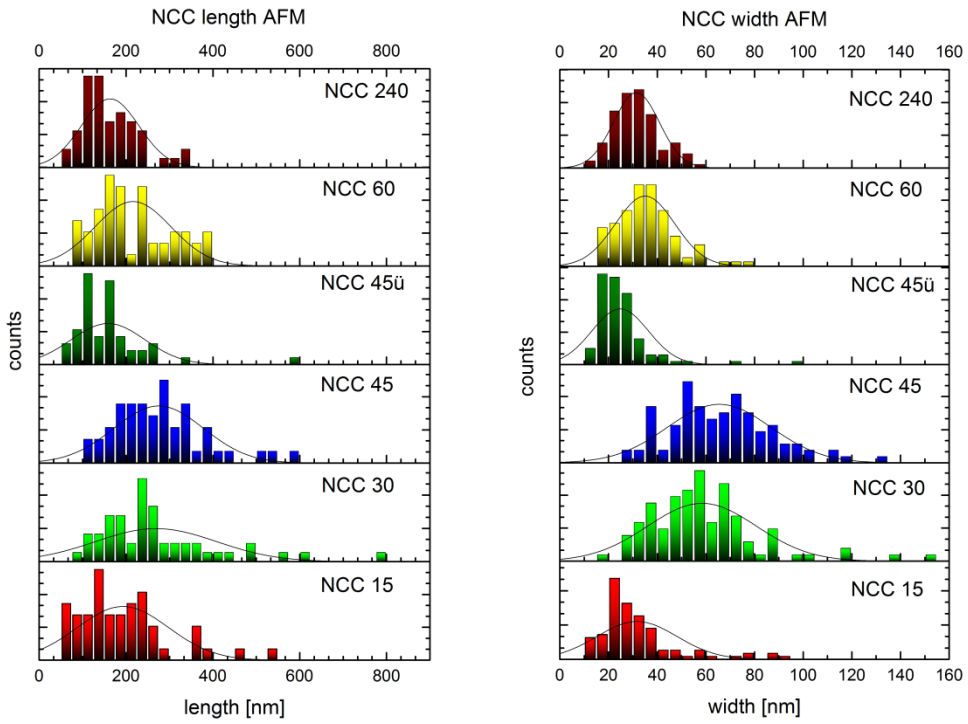

Figure 43: Size distribution measured with AFM of different NCC batches, grain length (left side) and grain width (right side)

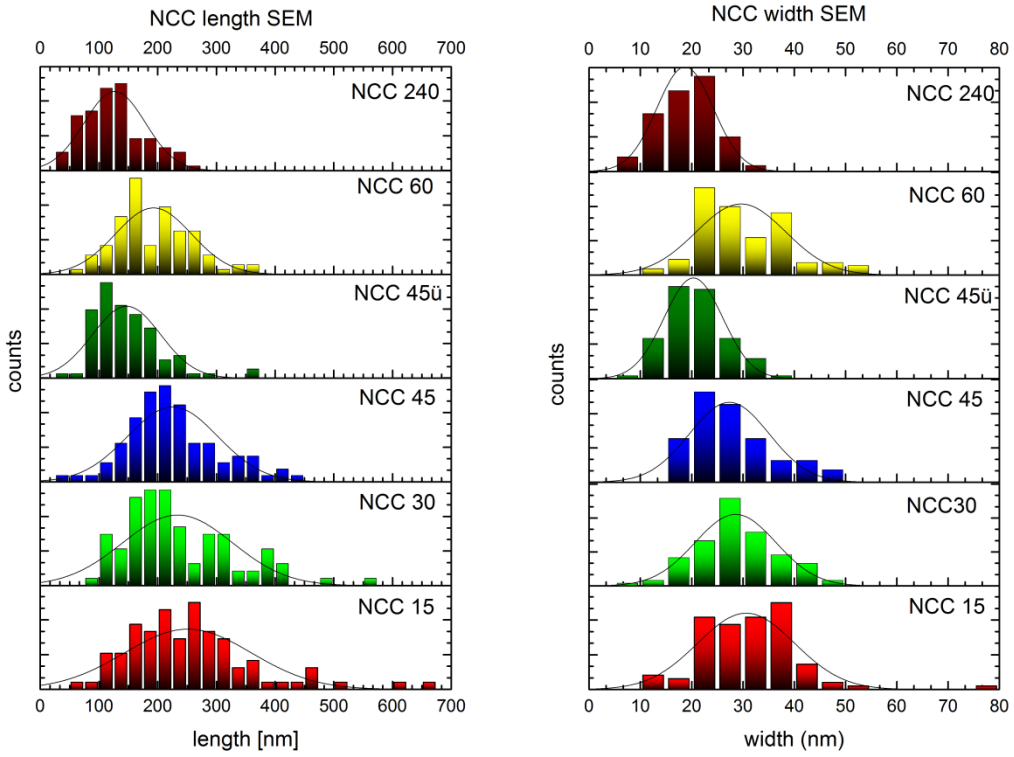

Figure 44: Size distribution measured with SEM of different NCC batches, grain length (left side) and grain width (right side)

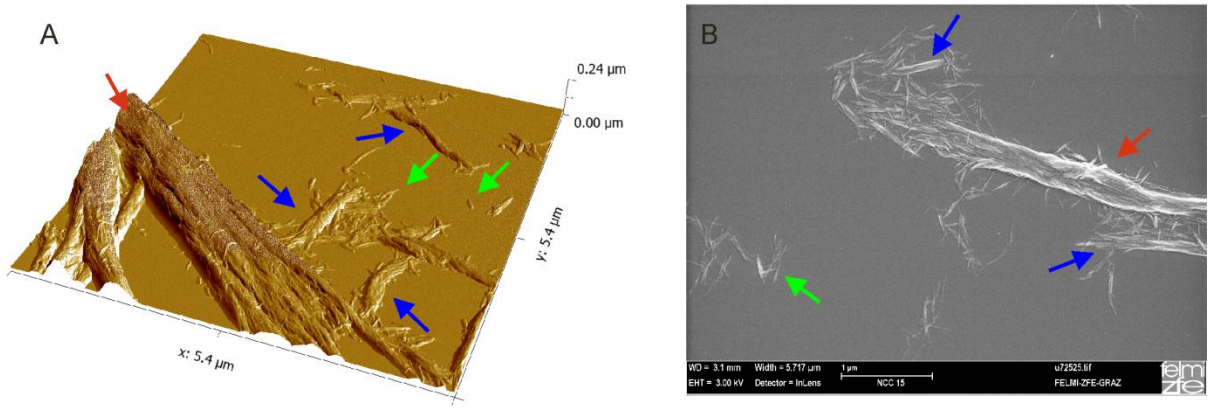

Figure 45: 3D Image of NCTFC with NCC15 sample made via AFM (A), SEM image of sample NCTFC with NCC15 (B), they show cellulose fibrils (red arrow) breaking into smaller fibrils (blue arrow) and finally remain as nano crystallites (green arrow)

NCC15 was found to be cloudy with some flakes swimming around, meaning the reaction was incomplete at the time that the batch was taken. Although not suitable for further experiments, this situation was highly interesting as we could observe half-broken cellulose fibrils via both **AFM** and **SEM** as shown in Figure 45. In the **AFM** 3D image (A) the edge of a big fibril is half broken down (red) and smaller fibrils down to **NCC** rest next to it (blue and green arrows). Corresponding **SEM** images (B) give similar results as indicated by the same colour code of arrows. This acts as direct visualization of the crystal breakdown towards smallest crystal units with a small-sized distribution. While morphological analysis is consistent with literature [69], the question remains as to whether this procedure indeed gives the expected cellulose from a structural and chemical point of view. Therefore, **XRD** and Raman characterization is needed as discussed in the following sections.

6.2.4 XRD of NCC

The intention for **XRD** investigations of **NCC** batches is to determine whether the crystalline structure of the source material is maintained. Through this, it can reveal differences which occur during fabrication based on hydrolysis processes. The source material is Whatman no. 1 filter paper, as mentioned above, and has a very high content of crystalline cellulose as the **XRD** reveals almost more than 99%. The **XRD** spectra of **NCC15**, **NCC45** and source material are directly compared in Figure 46. The **NCC15** and **NCC** 45 sample is made from 10 ml **NCC** solution, where most of the water is evaporated until only sludge remains, which can be put onto the **XRD** sample holder. The raw spectra have been baseline corrected and normalized to the strongest peak. Crystalline cellulose has a unique **XRD** spectra with two smaller peaks at 2θ angles of 14.9 ° and 16.6 ° caused by the (101) and the $(10\bar{1})$ crystal planes, respectively, and the main 2θ peak at 22.9 ° as a result of the (002) crystal plane (for more detail see [19, 70]). As can be seen, **NCC15** (top) and **NCC45** (centre) look identical and are moreover found in very good agreement with the reference measurement of the source material (bottom). These important results confirm that the applied syntheses route for the fabrication of nanocrystalline cellulose is capable of maintaining their original internal structure. Before a final comment on the material can be made, chemical measurements via Raman spectroscopy have to be carried out as discussed in the following section.

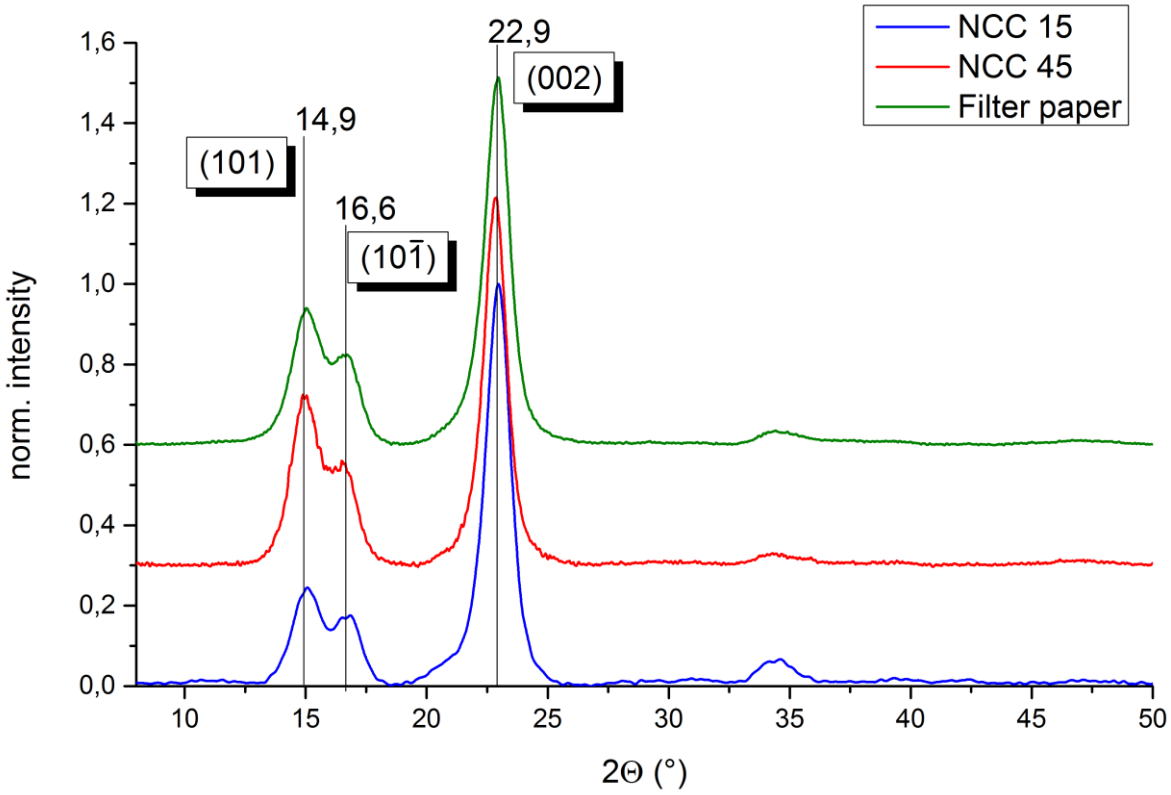

Figure 46: XRD spectra of NCC15 (top), NCC45 (centre) and filter paper as source material. All spectra have been baseline corrected and normalized to the strongest (002) peak at 22.9°.

6.2.5 RAMAN Spectroscopy of NCC

To gain information on the chemical nature, batches **NCC45** and **NCC45ü** (supernatant) were characterized via Raman spectroscopy and compared to the source material. For that, samples were prepared as follows. A silicon wafer was coated with 40 nm gold for better signal reflection. Afterwards a droplet of **NCC** solution was put onto the wafer and dried (see Figure 47).

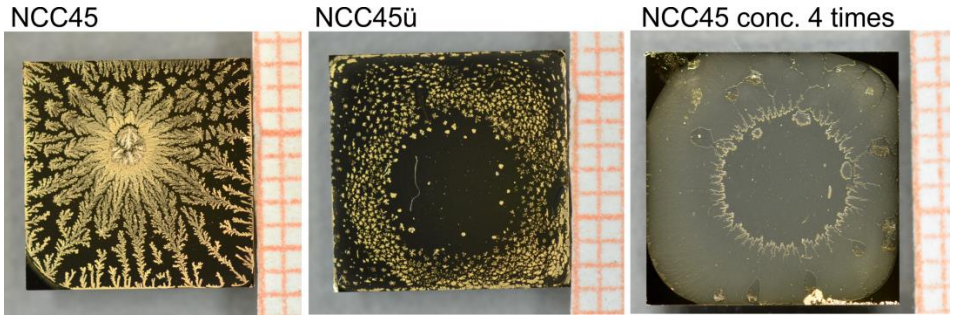

Figure 47: Sample ready for Raman investigation, left NCC 45, middle NCC45ü and right 4 times concentrated NCC 45.

The spectra are shown in Figure 48, which have been baseline corrected, **FFT** smoothed (5 points) and normalized to the strongest peak. To enable a direct comparison, the spectra have been stacked on top of each other. As can be seen, all batches reveal the peak at 1151 cm^{-1} which is related to crystal-

line cellulose I. In contrast, the amorphous peak at 1264 cm^{-1} cannot be found in any spectra. To investigate whether the latter peak cannot be seen due to the lack of intensity, a four-fold higher concentration of **NCC45** has been investigated as well (red curve), which also does not show any signs of a peak related to amorphous cellulose. However, an additional peak at 982 cm^{-1} can be recognized which could be identified as sulfate stretch [71] as a consequence of the synthesis route. The most important detail, however, is the very similar spectra compared to the crystalline source material (black curve), which again indicates that the original structure is maintained after the fabrication route towards **NCCs**.

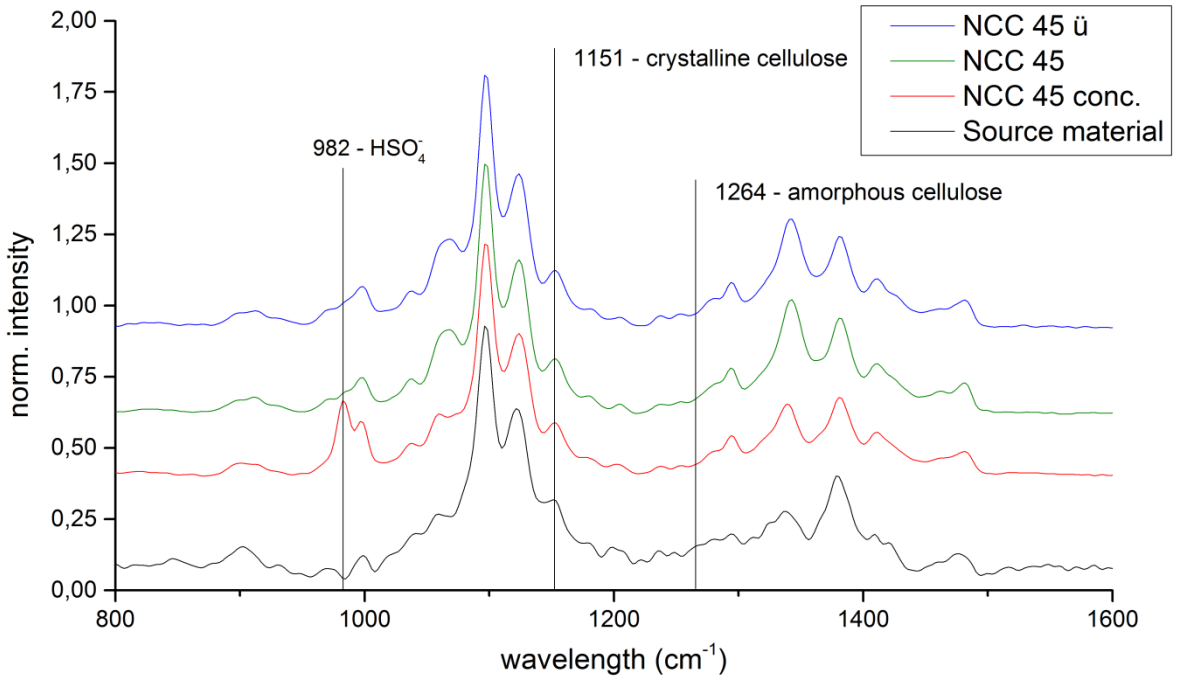

Figure 48: RAMAN spectroscopy spectra of NCC45, 4 times concentrated NCC45, NCC45ü and filter paper as source material. All are cellulose 1 with crystalline cell peak at 1151 cm^{-1} and lack of an amorphous peak at 1264 cm^{-1}.

Both **XRD** and Raman spectroscopy show convincing unambiguous results, which strongly suggest **NCCs** as crystalline cellulose as intended. This is the first main achievement of this thesis as a route was found to fabricate nano-crystalline cellulose with a comparably small length/comparable diameter distributions as confirmed via correlated **SEM** and **AFM** characterization.

6.2.1 TEM on NCC

Finally, **TEM** investigations were carried out to get a high-resolution insight for comparison with **AFM** results. A droplet of **NCC45** solution was put onto a carbon-coated **TEM** grid for 5 min and the remaining liquid was withdrawn using filter paper. Afterwards, the grid was stained with uranyl acetate for 2 min. The result is shown in Figure 49 where fine needle-like structures of nano-crystalline cellulose can be seen. These images revealed crystal widths in the same range as observed via **AFM** investigations specified above which, together with **SEM** imaging, confirms very small tip convolution during **AFM** investigations and therefore justifies the small error bars assumed.

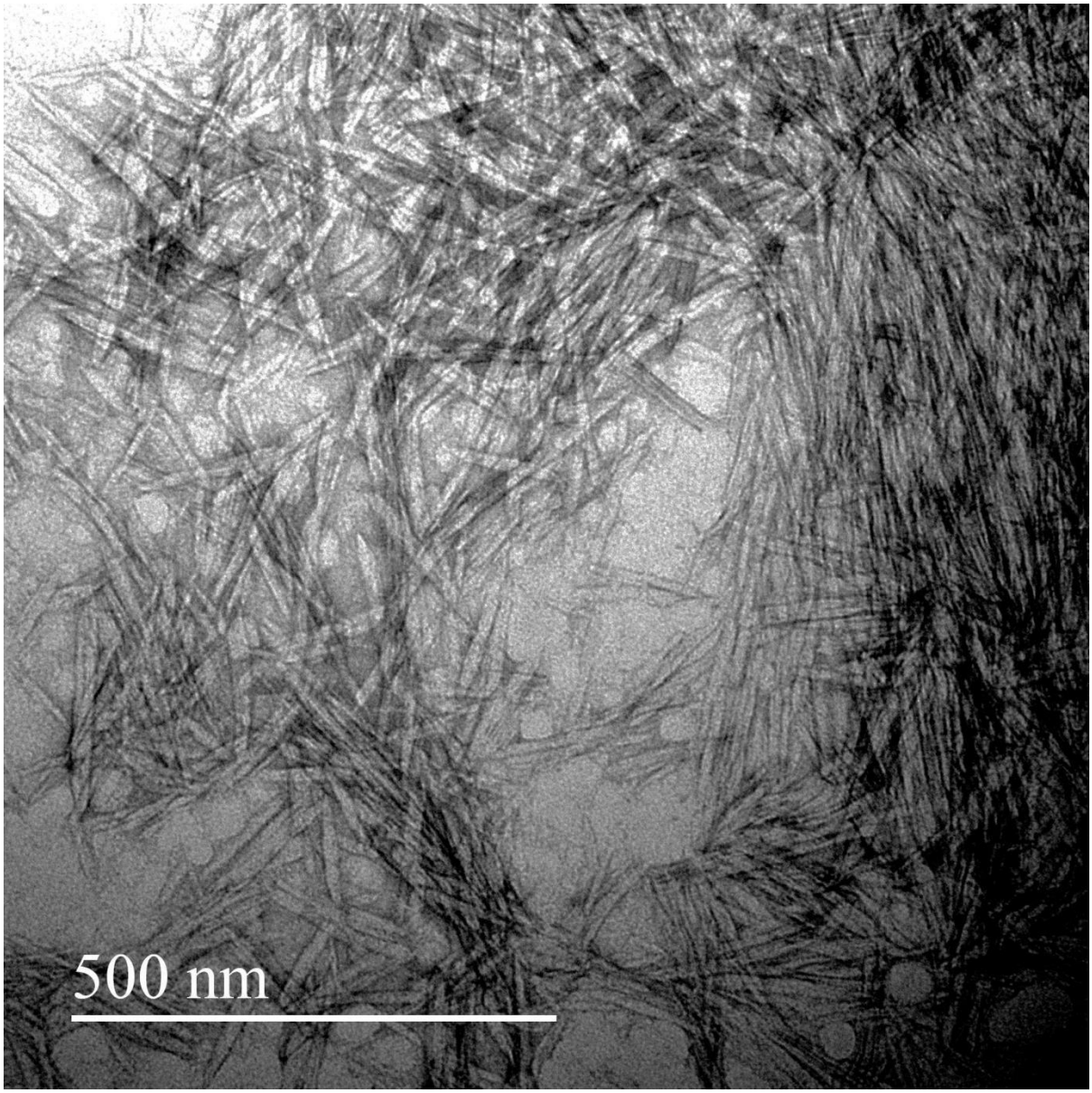

Figure 49: TEM image of NCC showing a haystack of crystallites. The sample was stained with uranyl acetate to increase contrast.

This achievement also enhances the already available cellulose substrate toolbox, as the material can be prepared via spin cast giving thin "particle layers" (nano-crystalline thin film cellulose, or **NCTFC**) as shown in Figure 38. Due to the chemical and structural peculiarities, such films are perfectly suited to individual enzyme experiments whenever highly crystalline nano-cellulose is the aim of the investigations. Finally, this material type represents the last missing part for a mixed amorphous/crystalline substrate as discussed in the next section.

6.2.2 Summary NCC

We could show with **AFM** and **SEM** investigation that the very small and highly crystalline cellulose particles have a narrow size distribution with lengths and widths/diameters of 225 ± 76 nm and 20 ± 5 nm, respectively. The synthesis of **NCC** takes about a day and batches can be stored for further use as a liquid solution in a refrigerator for later use. To ensure that these crystallites are indeed crys-

talline cellulose 1, **XRD** and Raman investigations were carried out. **XRD** data in Figure 46 and Raman data in Figure 48 illustrate this fact. In the **AFM** and SEM investigation, spin cast of **NCC** solutions (see Figure 50 3D Height image of 1 µm² area with phase overlay to enhance contrast) were used. In the next chapter, the spin coater will be used to make nano-flat thin films of cellulose.

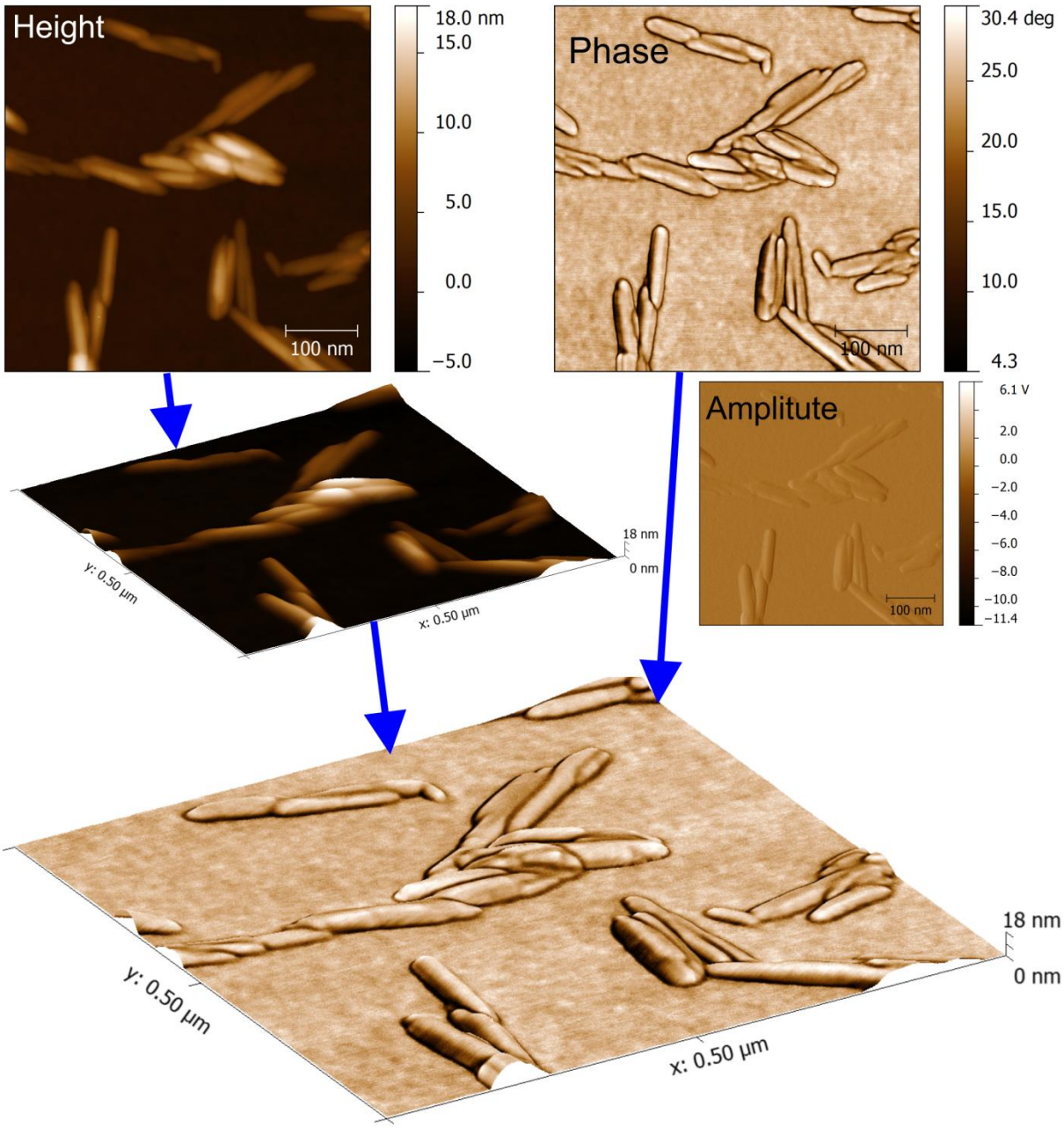

Figure 50: 3D AFM image of NCC45ü with phase data as colour overlay, showing highly resolved crystallites laying on the silicon substrate. Top left the AFM height image and right the phase image, below right a 3D image with just height information, below right the amplitude image and at the bottom the combined 3D height image with phase information as overlay.

6.3 Substrate – Spin Cast

Although the basic idea of spin-cast cellulose samples is not entirely new [72, 73], this thesis expanded existing principles using the crucial element of tunable contents of cellulose nano-crystals with a narrow size distribution. In the following, a short overview of previous activities is given where the so-called **MACS** substrates play a significant role. Then the new route is presented, which closes the missing gaps that are highly desirable for enzymatic in-situ investigations with real-time character. All spin-coating experiments were performed with a spin coater from *Laurell* shown in Figure 51.

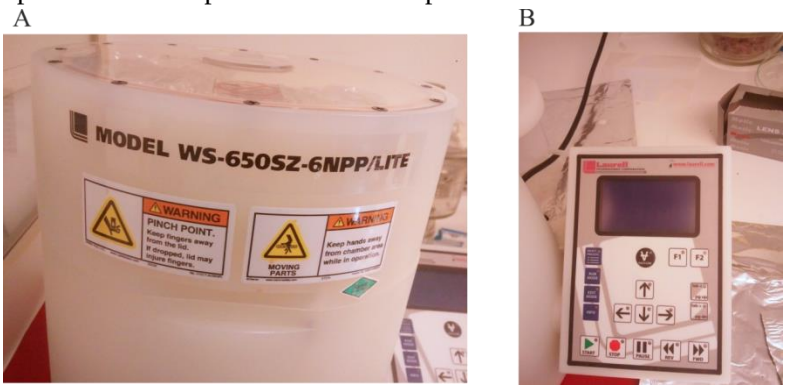

Figure 51: Spin coater used in this thesis was Model WS-650sZ-6NPP/lite from Laurell Technologies Corporation, Philadelphia, USA. A: Coating chamber, B: Controller.

6.3.1 Motivation

The main demands for absolute degradation quantification are thin (sub 500 nm) and flat (< 6 nm **RMS**) cellulose films which can be referenced to the underlying substrates (SiO_2 in our case). Although sophisticated in their smoothness and tune ability, **MACS** only allowed for relative degradation rates based on the variations from large cellulose crystals (µm sized) to surrounding areas. This was at least to a certain extent reliable as very large crystals are degraded very slowly [5]. Another handling disadvantage of **MACS** was that the ideal geometrical arrangement (XY plane perpendicular to the **AFM** tip) was almost impossible. **AFM** investigations can be more complicated and convolution from the cantilevers tip can be stronger when the sample is not planar rather than tilted. So investigations on a planar spin-cast sample are much simpler, in particular, because spin-cast cellulose samples can be perfectly placed on the **AFM** sample stages due to the enormously planar character of SiO_2 substrates. Secondly, **MACS** experiments used an in-house designed, variable temperature stage which was optimized for this type of substrates. However, the liquid level had to be kept in sight because otherwise the droplet could shrink so far that it loses contact with the scanner. In Figure 52 working in a droplet (A), which is in principle the same as working the **MACS** holder, is shown. The **FSB AFM**, on the other hand, has a micro-volume cell (see Figure 52 B, C) capable of performing experiments in liquid using only a very small amount of liquid. This micro-volume cell is sealed so no liquid can escape or evaporate. Only a small inlet and outlet lead towards and from the cell which are for the use of the injection system. Thirdly, the preparation time of **MACS** was crucial and typically ranged from 5 to 8 working days. Spin-cast cellulose, in principle, can be fabricated within an hour, which makes the entire procedure much more convenient.

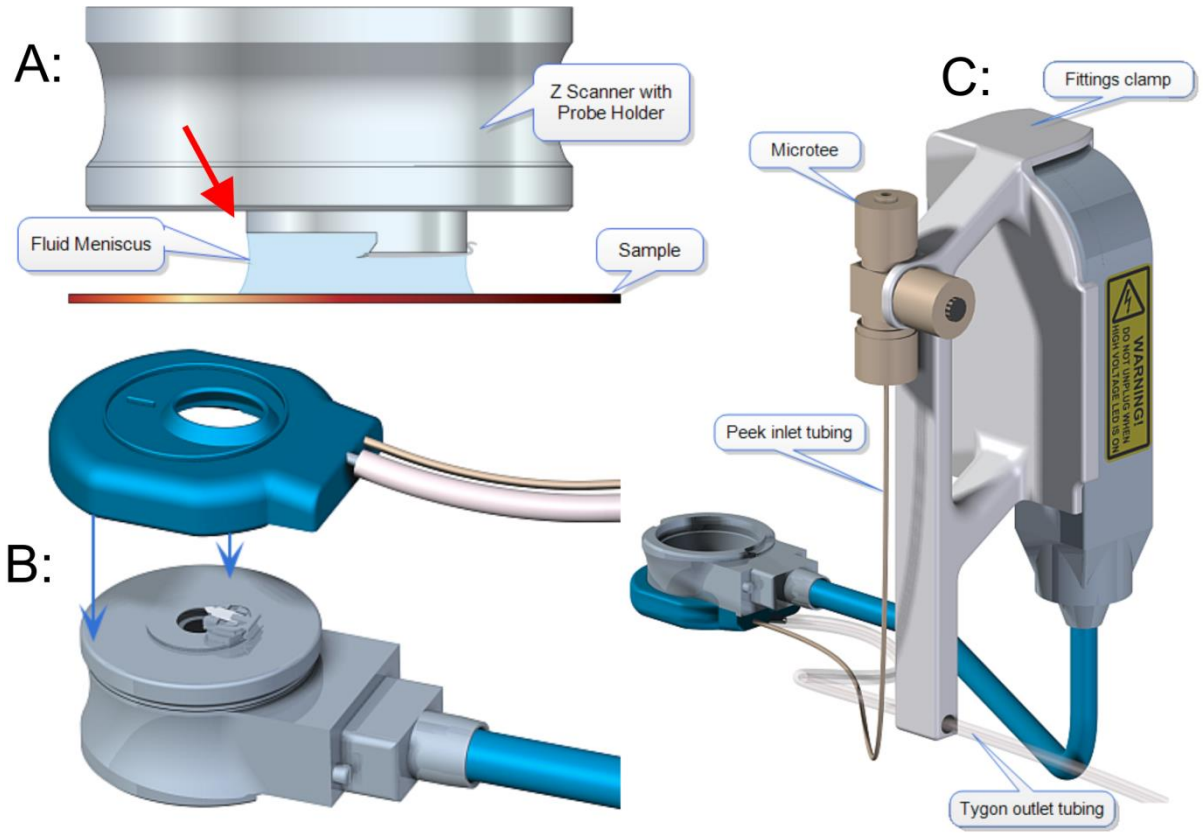

Figure 52: Schematics of working in a droplet (A) compared to the Bruker micro-volume cell. The micro-volume cell is mounted with its silicon fluid camber onto the FastScan Z scanner (B) and a clamp with inlet system for syringes is placed onto the Z scanner connector (C) [50].

The main reason for a new substrate, however, was the very wide grain size distribution of **MACS** ranging from 10s of nm to 10s of µm which was moreover hardly to control and never reproducible. Therefore, having amorphous and nano-crystalline thin film cellulose available is just a small step towards a combination which could solve many problems. This is the main part of this section in which both systems are described individually followed by the desired combination.

6.3.2 TMSC as Precursor for ATFC

The first step towards an ideal thin film spin-cast sample is the appropriate solution into which the desired material can be dissolved. Cellulose, however, is complicated or even not at all soluble in most solvents. One way to bypass this issue is the attachment of soluble side groups such as trimethylsilyl at the oxygen position of the side arms from polysaccharide chain. In the case of cellulose, these oxygen atoms would have a hydrogen atom, as can be seen in Figure 53. From the synthesis of cellulose with trimethylchlorosilane, trimethylsilyl cellulose or **TMSC** is received [74]. In this thesis former synthesized **TMSC** from Thomas Ganner and Manuel Eibinger were used throughout the study. **TMSC** can easily be solved in tetrahydrofuran (**THF**). The corresponding boiling point is in the range of 65 – 67 °C, which is ideal for spin-cast preparation towards homogenous and flat cellulose films. In this thesis **TMSC** is used as a precursor of thin film substrate of pure amorphous cellulose.

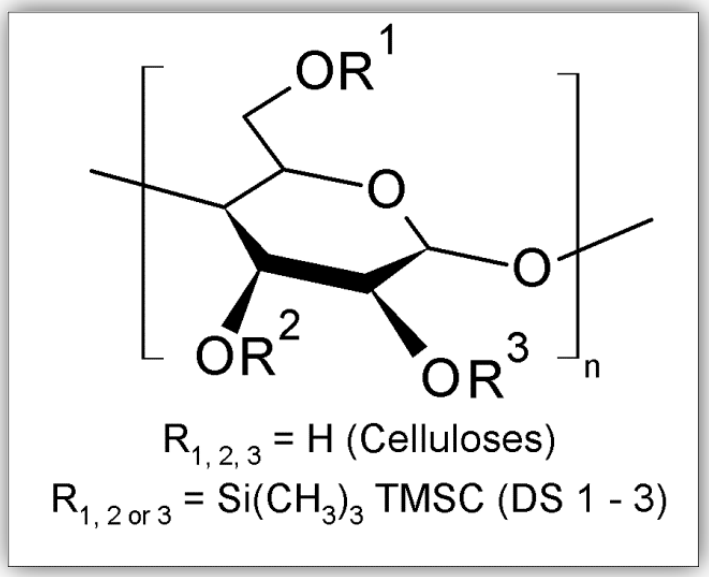

Figure 53: Single glucose monomer constitute in case of all residuals being hydrogen cellulose and in case of 1, 2 or 3 residual being trimethylsilyl TMSC.

The substitution of hydrogen at OH groups otherwise responsible for strong H-bonding is thereby not present any more [75, 76]. As a silylated derivate of cellulose, solvability in various solvents is given. We used Tetrahydrofuran (**THF**) to dissolve **TMSC** as a solution for spin-cast processing. In this way thin films of TMSC can be produced, as solution **TMSC** (20 g/l) was dissolved in **THF** and sonicated (*BANDELIN SONOPLUS HD 2200 with rod MS 72*) for 10 minutes. Prior to preparation, the solution is sonicated again for 1 minute and is spin-coated on the former processed silicon wafer substrates with a linear acceleration to 4400 rpm in 4 seconds, followed by 30 seconds of constant spinning. After the spin-cast procedure, the trimethyl silyl residuals have to be removed. This process is called regeneration [77] or curing of cellulose which is performed via HCl(g). In the curing step, the film is exposed to HCl(g) in a camber with a light vacuum applied by a water suction pump. Within the camber, the HCl(g) is resubstituting the Trimethylsilylgroups with H to get cellulose thin films. Structurally the special preparation yields the amorphous unordered form of cellulose and hence so-called amorphous thin film cellulose (**ATFC**). Without the synthesis of **TMSC** this process has the advantage that samples can be prepared very quickly in a few hours. However with fast evaporating solvents like **THF** the step between applying solution and starting the spin-cast process has to be taken very quickly, otherwise inhomogeneous layers appear as seen in Figure 54. Only one of ten samples deliberated a good thin layer, the main reason being a high room temperature due to a hot day. At normal room temperature this does not happen.

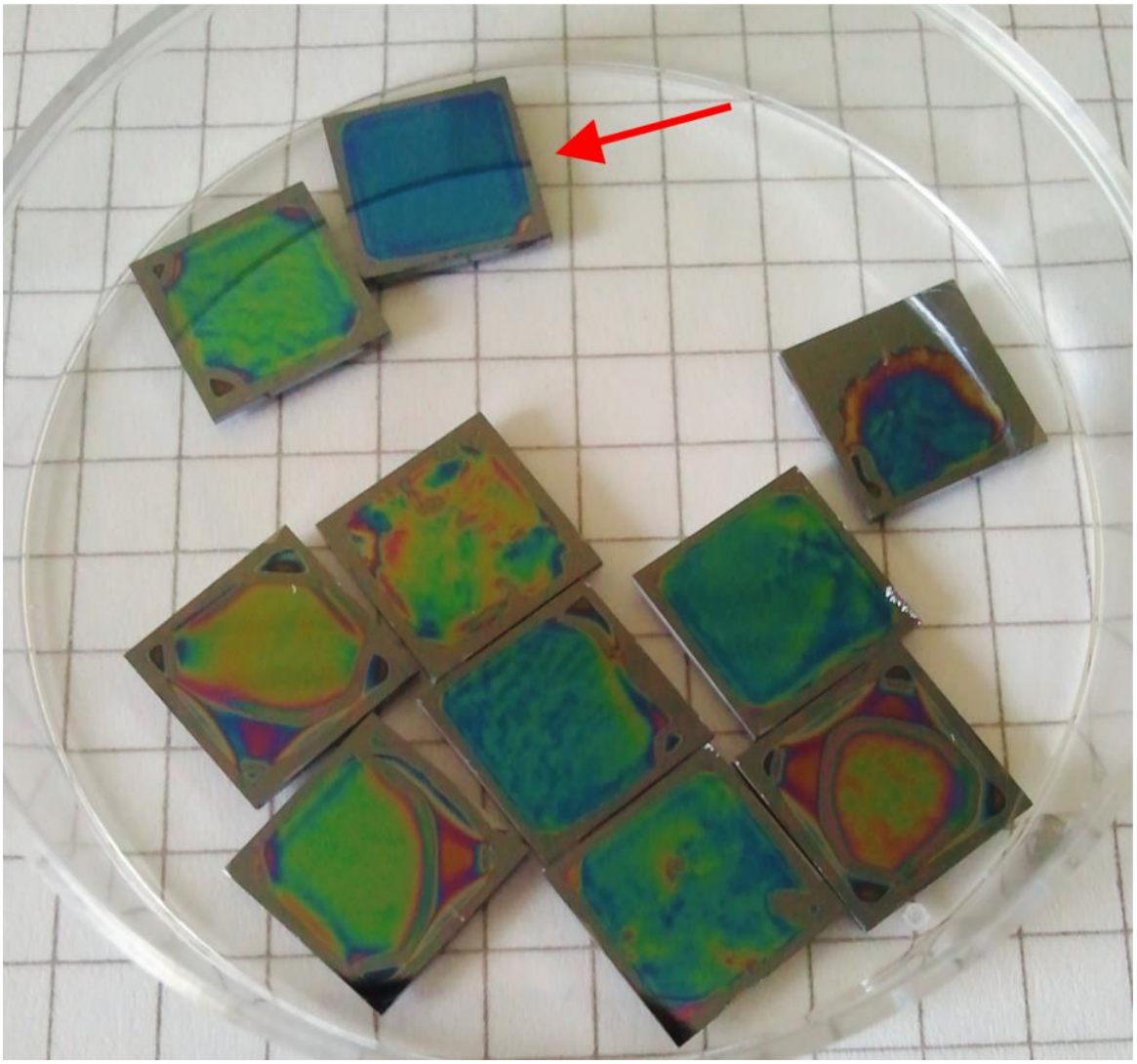

Figure 54: ATFC Colourful thin layer, perfect thin layer sample (red arrow)

In the curing process the hydrochloric acid gas makes a nucleophilic reaction exchanging the silyl residual against hydrogen, giving rise to shrinkage in layer height, which is significant due to the large size of trimethyl silyl compared to a single hydrogen atom. In Figure 55 a thin film layer of **TMSC** is shown before curing (left) with a layer height of 392 nm and after curing (right) with a layer height of 162 nm, which represents the **ATFC** substrate. The layer has a yellowish to brownish colour depending on layer thickness while the black background represents the silicon wafer as shown in Figure 55.

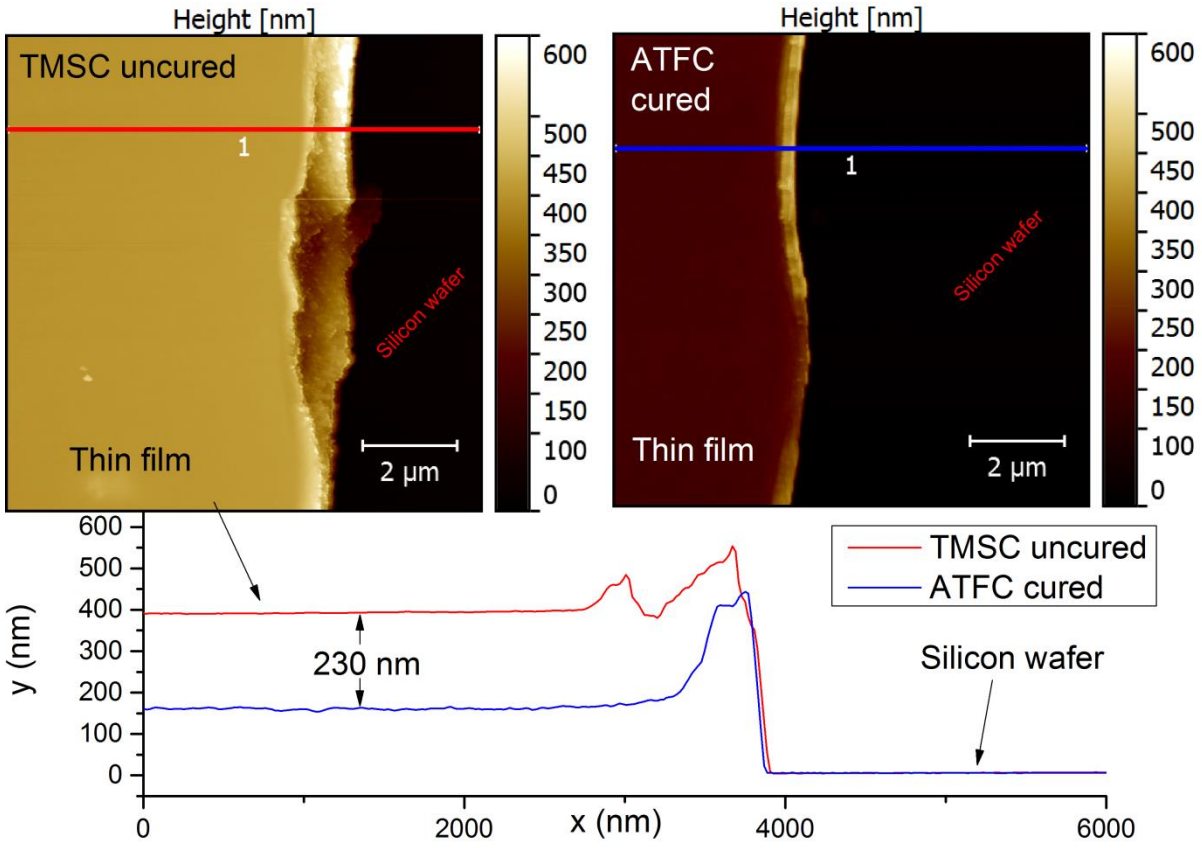

Figure 55: Direct AFM comparison of TMSC layers before (top left) and after (top right) HCl curing. The lower graphs are cross-sectional profiles along the lines in the AFM images (red for TMSC and blue for ATFC) following the same colour code.

The lower graph in Figure 55 gives cross-sectional profiles along the indicated lines in the upper **AFM** images. The layer height difference of about 230 nm corresponds to shrinkage of about 59%. However, the layer surface is still nano-flat (6 nm **RMS**) and pore-free/crack-free, as can be seen in Figure 56. The latter aspect is also crucial for high-resolution imaging during real-time, in-situ **AFM** measurements and therefore of particular importance.

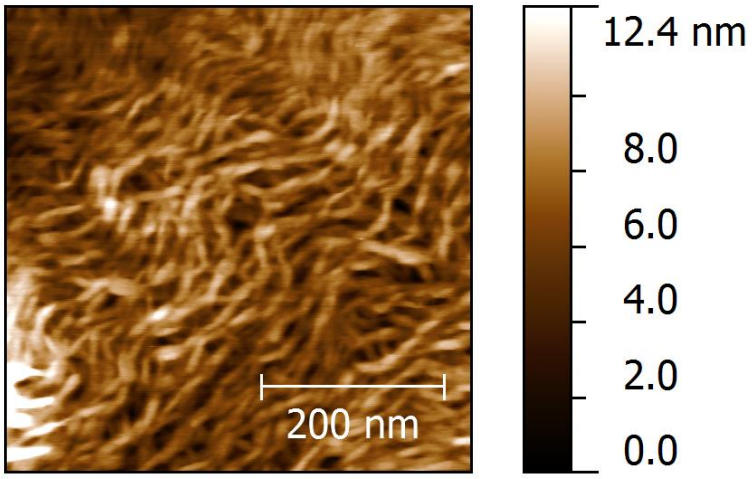

Figure 56: High-resolution ATFC AFM height image showing nano fibrils. Image size is 500 x 500 nm² [9]**.**

6.3.3 Combination of TMSC with NCC for SCTFC

Now the final step is carried out by means of mixing **TMSC** solutions (towards amorphous cellulose) with **NCC** solutions (crystalline contributions) as discussed in chapter 6.2.2. on page 43. Prior to addition to **TMSC**/**THF** solution, the **NCC** solution was pulsed-sonicated for 1 minute because **NCC** tends to agglomerate. For the final sample solution 2 ml of the 20 g/l **TMSC**/**THF** solution was mixed with 10 µl of 18.4 g/l **NCC** solution via sonication for at least 1 minute. This solution with typical concentrations of 0.184 mg **NCC**/40 mg **TMSC**/2 ml **THF** is now ready and can be used for spin cast as if it were a normal **THF** solution. Therefore the procedure to create semicrystalline thin film cellulose (**SCTFC**) is the same as for **ATFC**. For that, 10 x 10 mm^2 SiO_2 substrates were used, which were taken from sealed wafer boxes under a laminar flow box. Typically, spin-cast parameters of acceleration to 4400 rpm in 4 sec and spinning at 30 sec at 4400 rpm were used, which gave homogeneous films. To tune the film thickness itself, the overall **TMSC**/**NCC** concentration in the solvent can be adapted to provide film thicknesses from sub-100 nm to 500 nm while the spin-parameters have been found to be of minor influence [11].

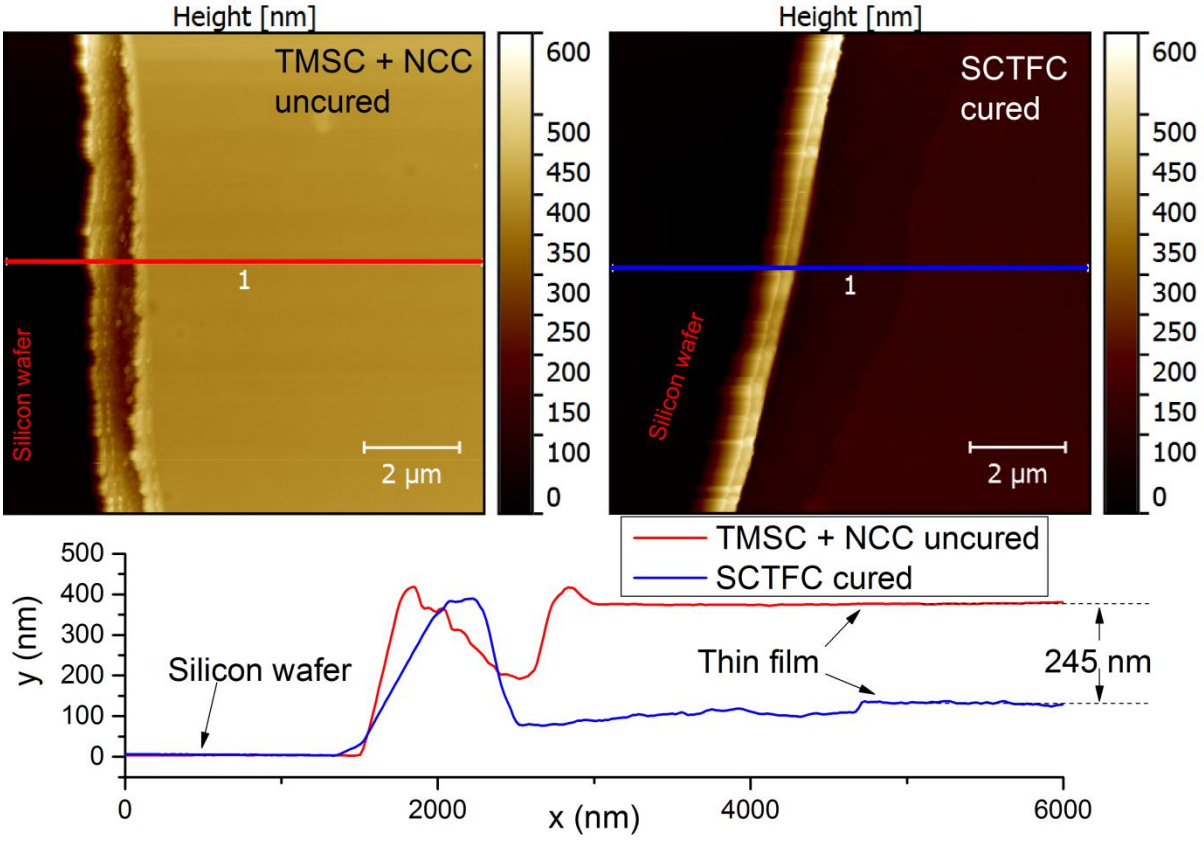

Figure 57: Direct AFM comparison of TMSC – NCC layers after spin-cast preparation (top left) and SCTFC films after HCl curing (top right). The lower graphs are cross-sectional profiles along the lines in the AFM images following the same colour code.

After spin casting, the films were subjected to the curing process by which the created thin film is exposed to HCl(g). This is done in a camber with a light vacuum applied by a water suction pump. The silicon wafer is placed away from the 3 mol/l HCl solution. Within the camber the HCl evaporates and the gaseous HCl resubstitutes the Trimethylsilylgroups at the oxygen with hydrogen to get

cellulose thin films [75]. Structurally the special preparation yields the amorphous unordered form of cellulose and hence amorphous cellulose while the **NCC** is not affected by the HCl and stay embedded in the amorphous matrix. The result is now semicrystalline thin film cellulose (**SCTFC**). Figure 62 shows a **TMSC**/**NCC** film before (top left) and after (top right) HCl curing together with cross-sectional profiles at the bottom following the indications in the upper **AFM** images. As can be seen, the initial layer height of 376 nm is decreased to 131 nm for the final **SCTFC** films meaning shrinkage of 65%. Figure 58 furthermore gives the first direct evidence that the intended multi-component approach was successful. The **AFM** images reveal **NCCs** embedded in the amorphous matrix as expected while the overall surface roughness is still very low (10 nm **RMS**). This image was made the unique peak force mode option of the **FSB**. In the images on the left, laterally resolved modulus (top), deformation during scanning (centre), and energy dissipation (bottom) information are revealed which fully confirms the small parts as crystalline parts: higher modulus, less deformation and less energy dissipation. Also of importance is the minor change of structural composition after curing.

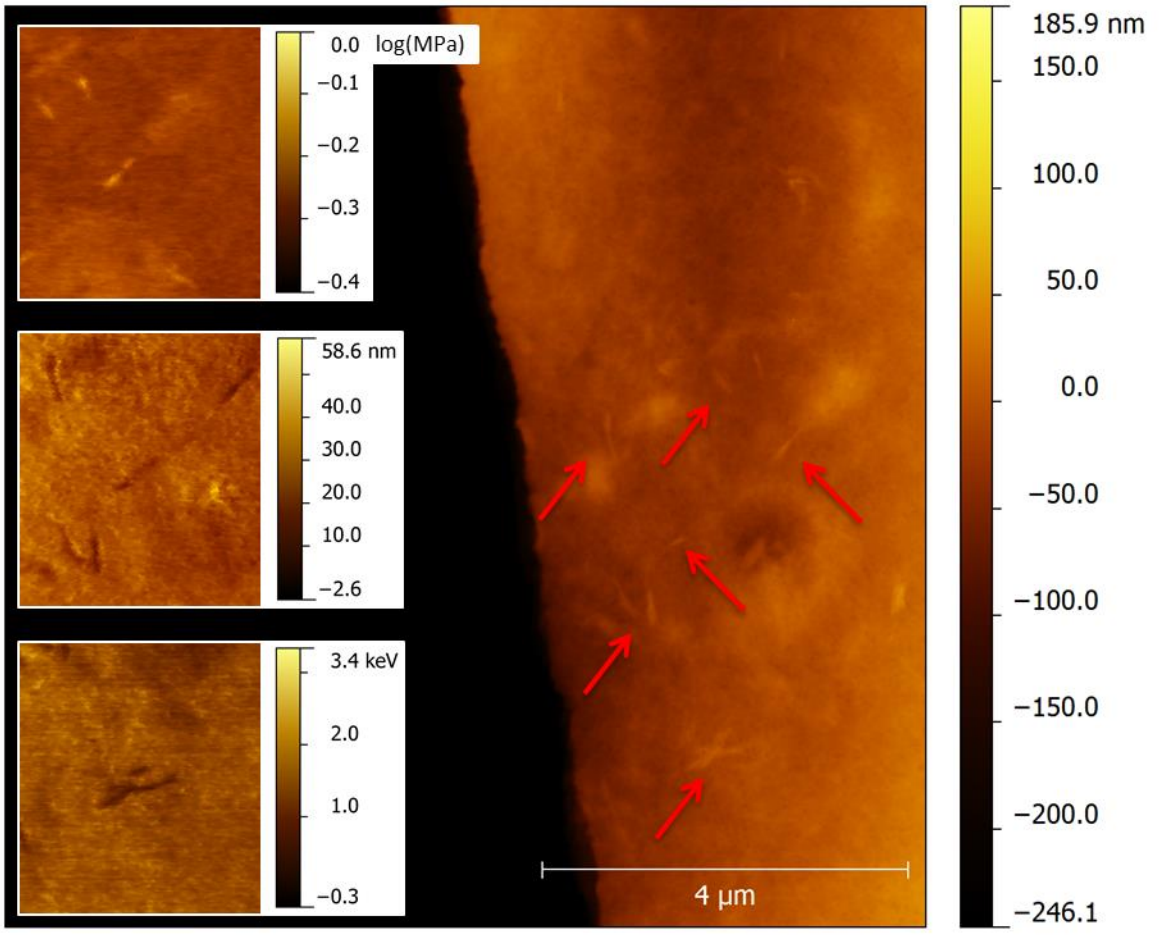

Figure 58: SCTFC substrate revealing the embedded NCC crystals (red arrows) in the fully amorphous matrix. The images on the left are based on the unique peak force mode option of the FastScanBio platform revealing laterally resolved modulus (top), deformation during scanning (centre), and energy dissipation (bottom) information which fully confirms the small parts as crystalline parts: higher modulus, less deformation and less energy dissipation.

To obtain information on the inner distribution, **SCTFC** films were spun onto glass slides and after curing transferred to a **TEM** grid and subjected to **TEM** investigations as they provide a transmission projection through the film. Such films were not stained and still show a good contrast during **TEM** investigations which are shown in Figure 59. As can be seen, the **NCCs** are often isolated when they are embedded, which confirms the intention of well-spread single **NCC** sitting in an amorphous cellulose matrix.

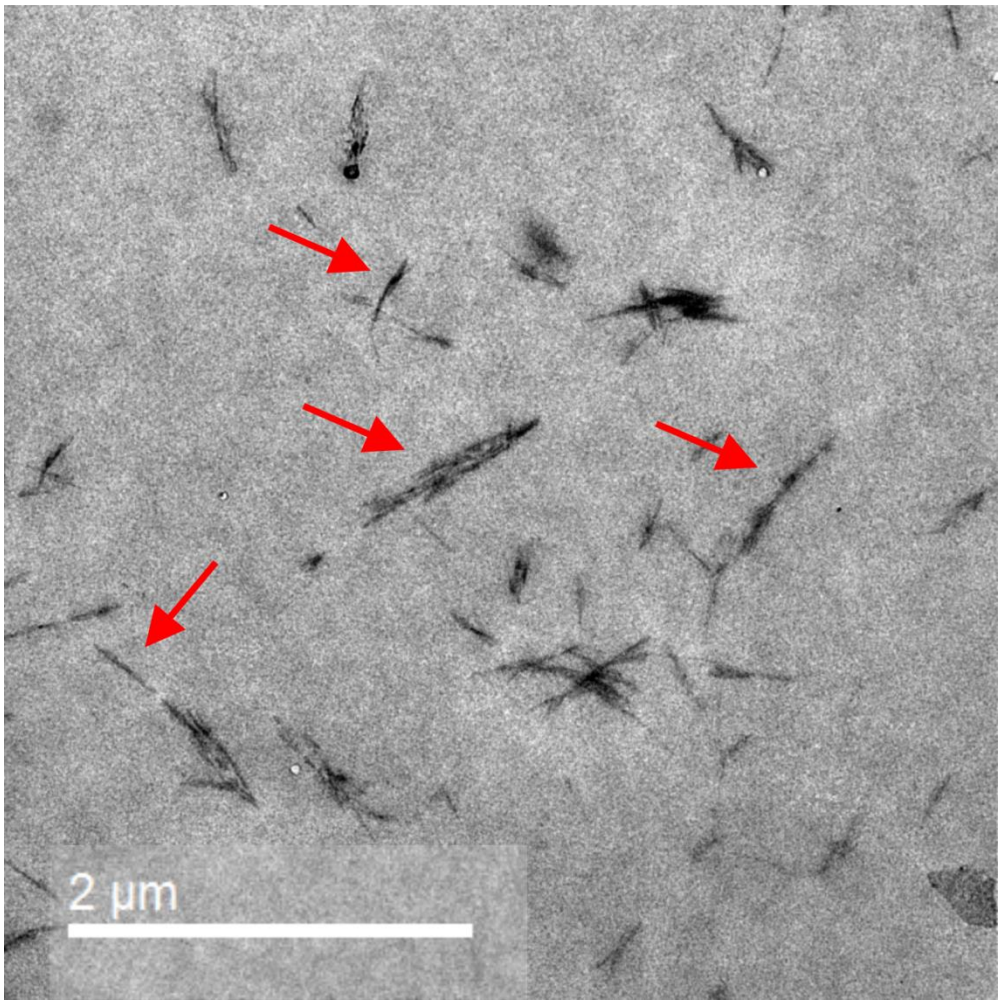

Figure 59: TEM image showing NCC grain indicated by red arrows.

Therefore a comprehensive picture is drawn which confirms that the **TMSC**/**NCC** approach allows for the fabrication of **SCTFC** films with nano-flat surfaces and embedded **NCCs** down to single-fibre embedding. Furthermore, it is possible to tune the crystalline content and film thickness via concentration adaption which is representatively shown in Figure 60. The amount of **NCC** solution before mixing with **TMSC**/**THF** solution was varied, thus changing the overall **NCC** to amorphous cellulose ratio. The graph below the images in Figure 60 shows the correlation between variations of added **NCC** solution with a visible number of **NCC** grains in **TEM** images.

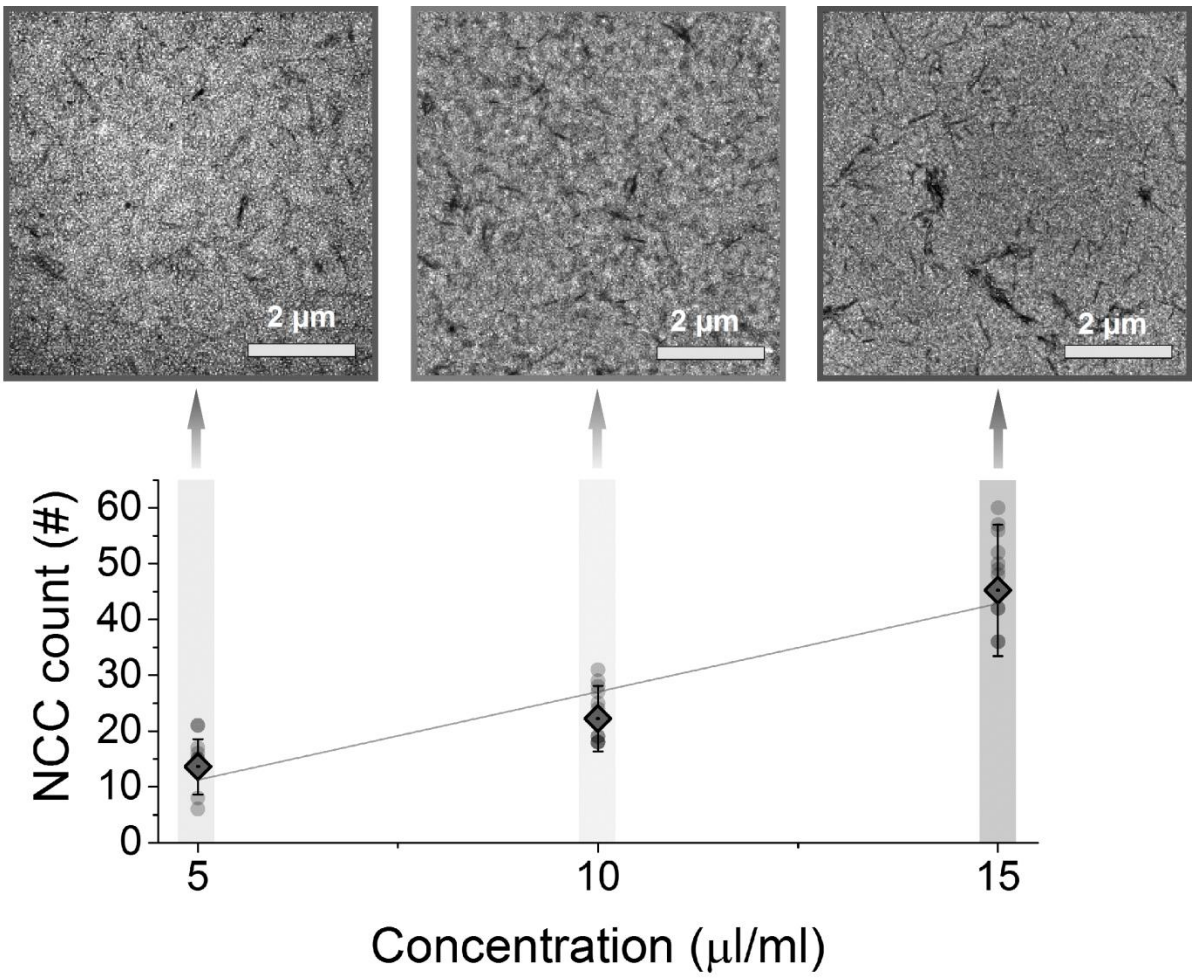

Figure 60: Concentration variation in SCTFC imaged via TEM. The graph to the lower part shows counts of NCC correlating with NCC solution concentrations used for the spin-cast solution. The corresponding images can be seen above.

6.3.4 Summary: Fully Tunable SCTFC Substrates

As a main achievement of this master's thesis, a substrate has been developed which provides ***1)*** nano-flat surfaces (<10 nm **RMS**) over large areas (> 100 µm^2); ***2)*** nano-crystalline cellulose particles which are embedded in a fully amorphous matrix; and ***3)*** tunability concerning the crystalline content and film thickness (50 – 500 nm). These semicrystalline thin film cellulose (**SCTFC**) substrates are based on the combination of **TMSC** solutions and **NCC** dispersions in organic solvents. Detailed investigations within this thesis have confirmed the fully crystalline cellulose character of **NCCs** from structural (**XRD**) and chemical perspectives (**RAMAN**). Morphological investigations (**AFM**, **TEM** and **SEM**) revealed crystal lengths and diameters of 225 ± 76 nm and 20 ± 5 nm, respectively. Together with previous studies confirming the fully amorphous character of **TMSC** films, **SCTFC** films could be fabricated. A detailed look via **AFM**, **SEM** and **TEM** finally consolidated the intended film properties. The only thing missing is degradation experiments via enzymes, which are needed to give this fully tunable, artificial cellulose substrate the attribute "close-to-nature" which is described in the following sections.

6.4 Enzymatic Degradation on SCTFC Substrates

Many investigations of enzymatic activity on cellulose with enzymes from the fungus *Trichoderma reesei* were carried out on pulp cellulose [31]. This research gave rise to the identification of many different types of enzymes from the supernatant of *Trichoderma reesei* including their functionality and shape. But there are still a lot of unknown enzymes and only a few people are working with **AFM** to gain in-situ knowledge of the enzymatic activity. This might be because substrate requirements are very high for **AFM** in liquid environments and also difficult to handle from a technical point of view and in terms of experience. At this point the material development activities at the **FELMI-ZFE** which became a major research area during recent years are relevant. Previously developed substrate types, namely **FSEC** [10, 11] and **MACS** [5] have already led to a deeper insight into fundamental processes. However, whenever a step forward was achieved new demands on the substrate arise. This finally led to the definition of an ideal substrate which was realized in this thesis: semicrystalline thin film cellulose (**SCTFC**). So far, the thesis has described the fabrication and its chemical, structural and morphological characterization, which is very promising. However, in this final part of the thesis the question is addressed as to whether this substrate also shows the expected chemical and structural behaviour during enzymatic cellulose degradation. This has been done via well-understood enzymes by means of individual and collective exposure of different enzyme species. As will be shown, these experiments were successful, which gives the **SCTFC** substrate a close-to-nature character which was the intention of this thesis. After that, a rather new enzyme – swollenin – will be investigated regarding its activity on cellulose. At this point the new **FSB** comes into play, which turns out to be the key for related real-time investigations.

6.4.1 SVG on SCTFC

As mentioned in chapter 6.3.1, one big advantage of **SCTFC** substrates compared to previously used **FSECs** and **MACSs** is the possibility to determine absolute volumetric degradation rates due to the defined layer thickness. In Figure 61 a degradation experiment is summarized using **SVG** supernatants in a sodium acetate buffer solution at room temperature (24 °C). First, reference images without the supernatant **SVG** were taken. Next, 200 µl supernatant with a concentration of 20 µl/l was flushed through the liquid cell. Notice that the micro-volume cell only has a volume of 63 µl so more than double the volume of the cell was added to make sure that the right concentration was preserved. After incubation, the morphology was dynamically imaged at scan rates of 0.6 frames per minute at a scan range of 10 x 10 μm^2 by using a FastScan C cantilever. Please note that a movie of a dynamic 5 h degradation experiments can be found on the attached digital storage *("File 2 - Degradation SVG on SCTFC.mp4"*). The top curve in Figure 61 shows measured volumes at a given time while the solid curves are a b-spline for optical recognition of the trend. As can be seen, during the first 2 hours the degradation is very slow until after about 3 hours the degradation rate increases rapidly. This behaviour is consistent with the results found in former experiments on other substrates [3, 4, 7]. The bottom row in Figure 61 gives **AFM** images before incubation (label 1) as well as after 2 h (label 2), 3.5 h (label 3) and 5 h (label 4). The dark areas represent the silicon wafer (done by a fine scratch) while brighter areas show the **SCTFC** layer during degradation. The degradation can be well identified and also revealed that the layer is not homogeneously degraded but starts with pinholes, which then accelerate the local degradation rate. This is consistent with previous studies in which acceleration/deceleration behaviour was found and described in detail [4]. As the mentioned studies have been

performed on a very different substrate which is barely processed – and by that close-to-nature – but still in agreement with the observations described here, these first results suggest that **SCTFC** substrates behave like natural cellulose.

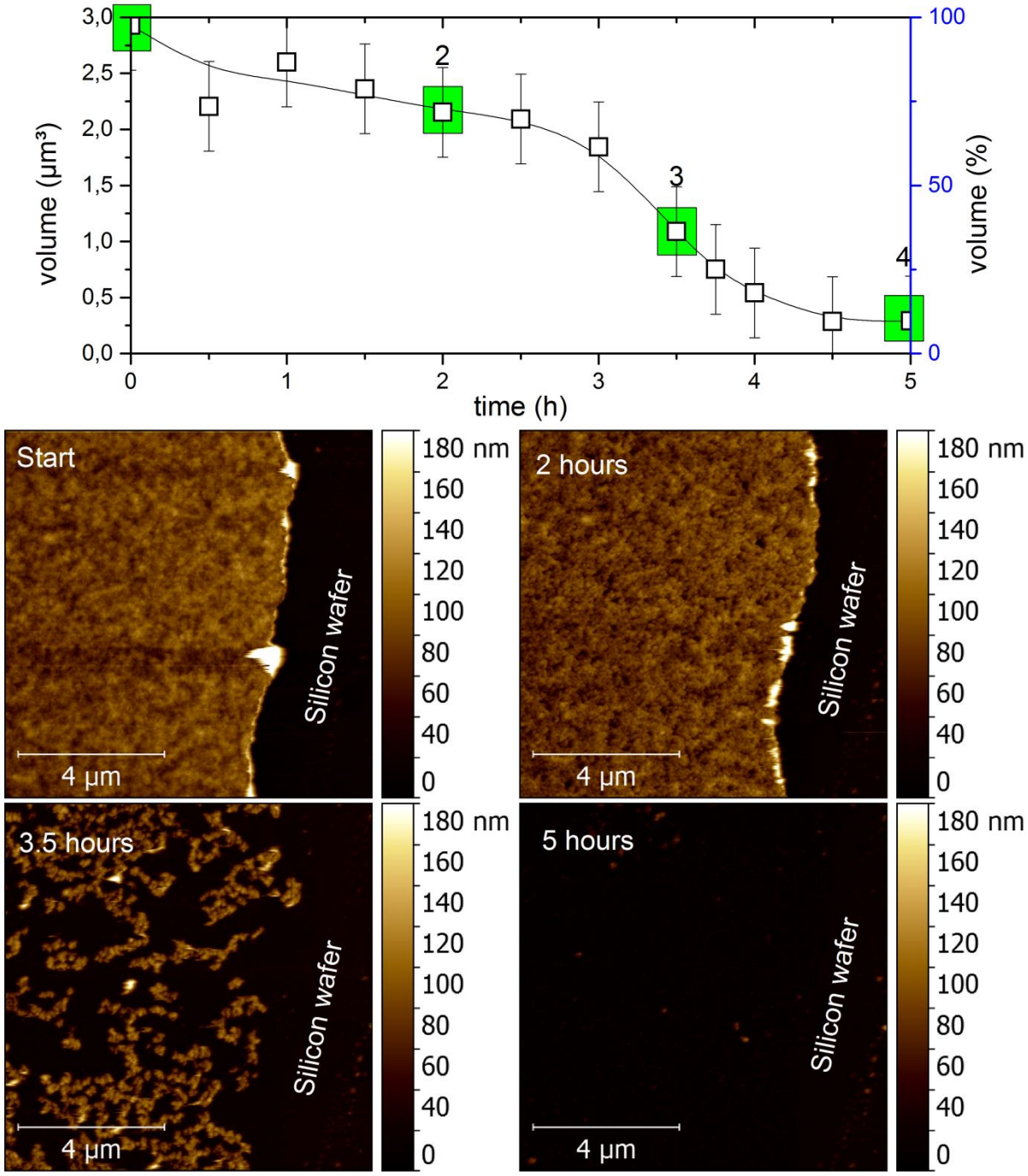

Figure 61: Degradation of SCTFC with supernatant SVG imaged via AFM. The graph (top) shows the volume loss of the thin film over time. The AFM height images (below 1 to 4) show the image corresponding to the point in the graph marked with a number and a green background.

To get a closer structural insight during degradation, Figure 62 shows an **AFM** image after 5 hours **SVG** degradation. As can be seen, the small **NCC** particles (confirmed with phase information top left) are excavated during hydrolysis which is consistent with previous high-resolution studies on a different close-to-nature substrate [3]. This not only further confirms the close-to-nature character of

SCTFC substrates but also impressively demonstrates the capabilities of the high-speed **AFM** as the scan rate was at 0.62 frames per minute but clearly resolved the **NCC** particles.

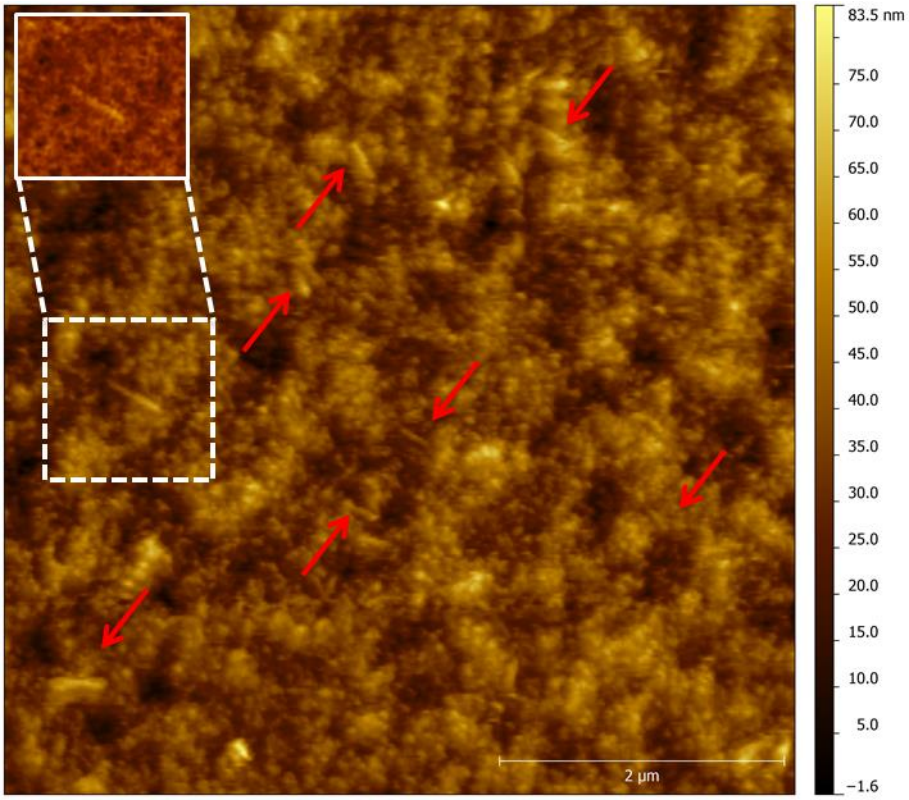

Figure 62: AFM height image of SCTFC during an enzymatic degradation. As can be seen, several NCC grains were excavated by the enzymes (red arrows) which have been proven as crystalline material via AFM phase imaging as representatively shown by the top left inset.

6.4.2 Sequential CBH1 and CBH2 on SCTFC

Adding individual enzyme solutions sequentially gives detailed information on which cellulose parts of an enzyme are active and if synergetic effects occur which either inhibit or boost the overall activity. **SCTFC** substrates were used for such experiments in combination with well-studied **CBH1** and **CBH2** enzymes [25, 30, 78]. While crystalline cellulose is mainly degraded by **CBH1** the amorphous cellulose is degraded by **CBH2** [7]. The setup included the micro-volume cell in combination with a sodium acetate buffer solution at 24 °C. Scan parameters were scan range 10 x 10 µm², scan rate 0.62 frames per minute and a FastScan DX cantilever was used. A short clip of this experiment can be found on the enclosed digital media *("File 3 - Sequential Degradation with **CBH1** and **CBH2** on SCTFC.mp4")*. Figure 63 summarizes the results by means of time-dependent volume loss (top) and **AFM** images at some points (below). As can be seen after exposing the **SCTFC** films to **CBH1** there is first a slight increase which indicates a swelling effect caused or might just be an **AFM** tip artefact. A reason for swelling could be that **CBH1** with affinity to crystalline cellulose tries to reach **NCC** grain in the amorphous matrix, which lifts the amorphous cellulose. But the more reasonable explanation is that the tip picks up cellulose fragments which change the tip shape and length thus increasing the measured volume. In the following, there is very small volume loss as **CBH1** is known to primarily act on crystalline regions which are mostly buried in the amorphous matrix as a key feature of

SCTFC. The observed volume loss can therefore be attributed to surface-exposed **NCCs**, which are expected to be low in total numbers. However, when adding **CBH2** after 3 hours, the expected decay is found after a certain activation time, which is needed to first excavate **NCCs** from the matrix. Once that has happened, the activity becomes very high due to synergistic effects, as observed before [4, 6, 7]. A closer look at the morphology during degradation is given in the lower part of Figure 63. Comparing the reference measurements (left image below the graph) with the situation after 3 h (image to the right) **CBH1** incubation reveals no drastic change of the thin film. After 3 h activity with **CBH1** and **CBH2** it becomes evident that degradation rate increases and also that the layer is not homogeneously degraded (see left image at the bottom of Figure 63). First pinholes appear which then accelerate the local degradation rate. Finally, shortly before the entire film has been degraded (7.6 h right bottom image) it can be seen that only islands of cellulose are not yet degraded.

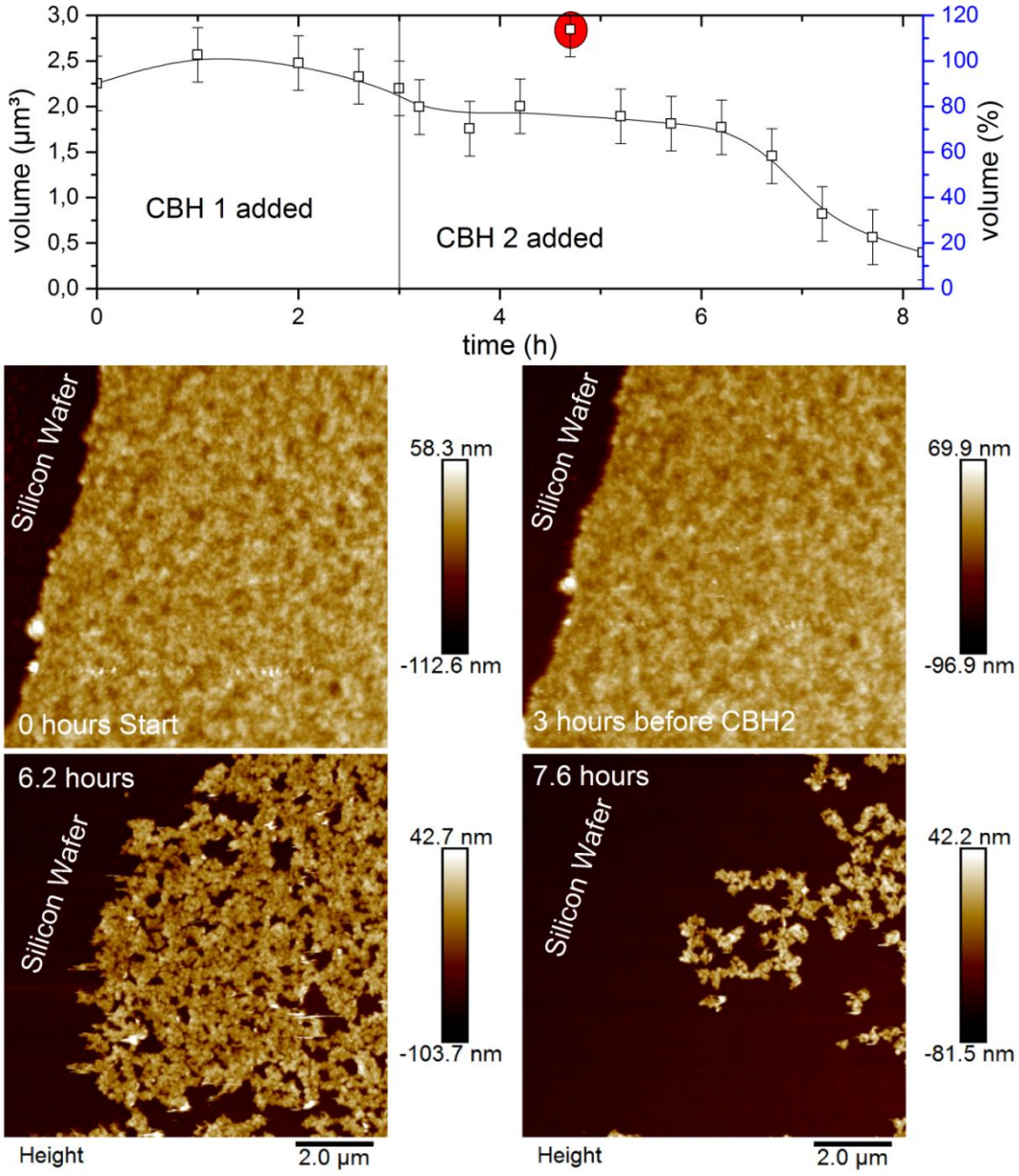

Figure 63: Sequential degradation experiment measured via AFM. The graph on top shows calculated layer volumes from the recorded images (squares) and a graphic interpolation between the squares (line), and one outliner is marked with a red circle. Below AFM height images from the experiment are shown at different points in time.

At the end a comment on image quality has to be made: As small cellulose fragments are dissolved they tend to stick to the cantilevers tip, which is a major problem in liquid when measuring cellulose in liquid. The problem increases when cellulose is digested, weakening the structural integrity of the thin film. This softens the cellulose further and makes it easy for the tip to pick up fragments. This results in image artefacts and can lead to corrupt measurement in the case of the square in the graph of Figure 63 (marked by a red circle shortly before hour 5).
In summary, the last two sections confirmed that the **SCTFC** substrate developed in this thesis fulfils the intended requirements. In particular, the enzymatic degradation experiments show the expected behaviour, which finally gives the substrate the close-to-nature character. This is in agreement with structural, chemical and morphological results gathered in this thesis. The cellulose substrate toolbox at the institute is therefore successfully expanded by nano-crystalline and semicrystalline thin film cellulose named **NCTFC** and **SCTFC**, respectively. In the following, the former is used to perform new experiments on a novel enzyme system.

6.4.3 Swollenin on Cellulose

As mentioned above, swollenin is a novel enzyme system which is thought to swell cellulose material, which then leads to improved diffusion capabilities of enzymes and therefore to an increased degradation efficiency [35, 79]. In this section we test this hypothesis and will demonstrate that swollenin works a little differently than expected. Swollenin was tested on plant cellular matter like steam-pretreated corn stover and it is suggested that swollenin plays a role in amorphogenesis [37]. Therefore our first attempt was to test swollenin on **NCC** to see if the crystalline cellulose is disrupted and we expect to see amorphous cellulose.

6.4.3.1 *Swollenin on NCC – AFM*

As a first step, we have to investigate the degradation/modification activity of swollenin on the crystalline parts. As **NCCs** represent the smallest crystalline cellulose parts it becomes evident that the **NCTFC** systems are an ideal bottom-up approach. For that, three different samples of **NCTFC** based on **NCC45** were produced. One was left untreated as a blank reference (dry conditions), the second was incubated with **BSA** (Bovine serum albumin, a serum protein derivate from cows as reverence with absolute no activity on cellulose) and the third was incubated with swollenin further denoted as **SWO1**. **BSA** and **SWO1** samples were incubated for 20 hours at a temperature of 40 °C and concentrations of 20 mg/l each. After that the **NCTFC** samples were rinsed with H_2O dried using CO_2 gas very gently so that only a weak gas flow would hit the sample. Samples were stored in petri dishes for safe and clean transportation until investigation via **AFM**. Figure 65 shows the results for all systems with respect to length and width distribution left and right, respectively. As can be seen, the swollenin does not degrade **NCCs** at all. Compared to blank reference it shows practically identical size distributions of **130 ± 62 nm and 26 ± 9 nm** for lengths and widths, respectively. **AFM** images were made under dry conditions and with a FastScanA cantilever. One image for overview with scan range of 10 x 10 µm² and high resolution of 2048 x 2048 pixels and 9 smaller images with scan size 1 x 1 µm² and resolution of 512 x 512 pixels was taken for each position on a sample. The scan speed was chosen in a safe area to ensure high resolution, for example it took about 3 minutes to record a small image. Three different positions were investigated per sample, one near the middle and two at an outer point but different sides of the sample. Figure 64 shows a typical blank, **SWO1** and **BSA AFM** height image with red arrows pointing out **NCC** grains. The small structures in-between are proven as solu-

tion-related impurities during pre-experiments. While these investigations can rule out a degradation activity of swollenin on crystalline cellulose, **AFM** cannot determine whether amorphization takes place. Therefore, structural investigations via **XRD** are needed as discussed in the following section.

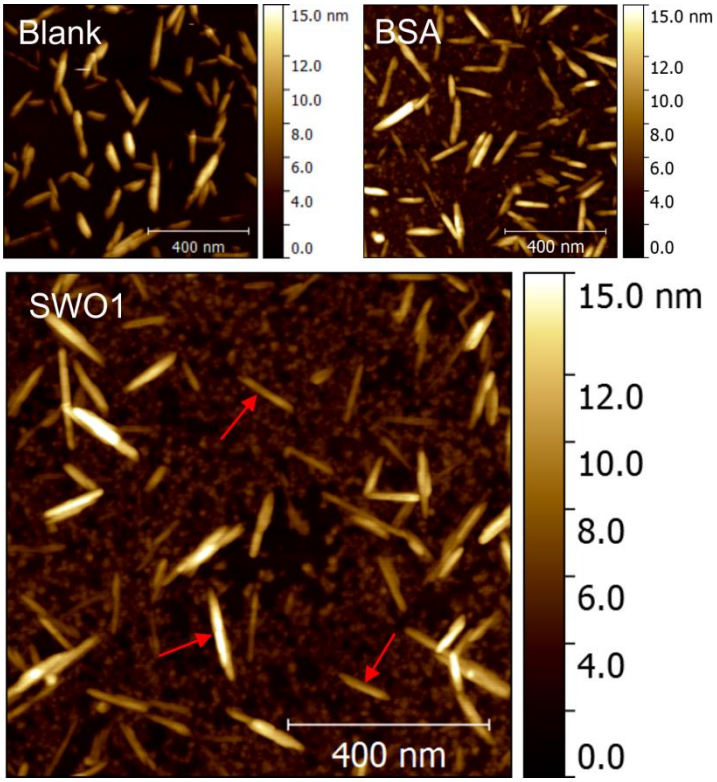

Figure 64: Typical AFM height images from the incubation experiment were SWO1 (lower image) and were tested on NCC45 to see an effect. Red arrows indicate NCC grains. As reference a non-incubated dry sample (top left) and a BSA incubated sample (top right) were investigated for direct comparison. The small grainy features have been identified as solution impurities during pre-experiments on flat surfaces.

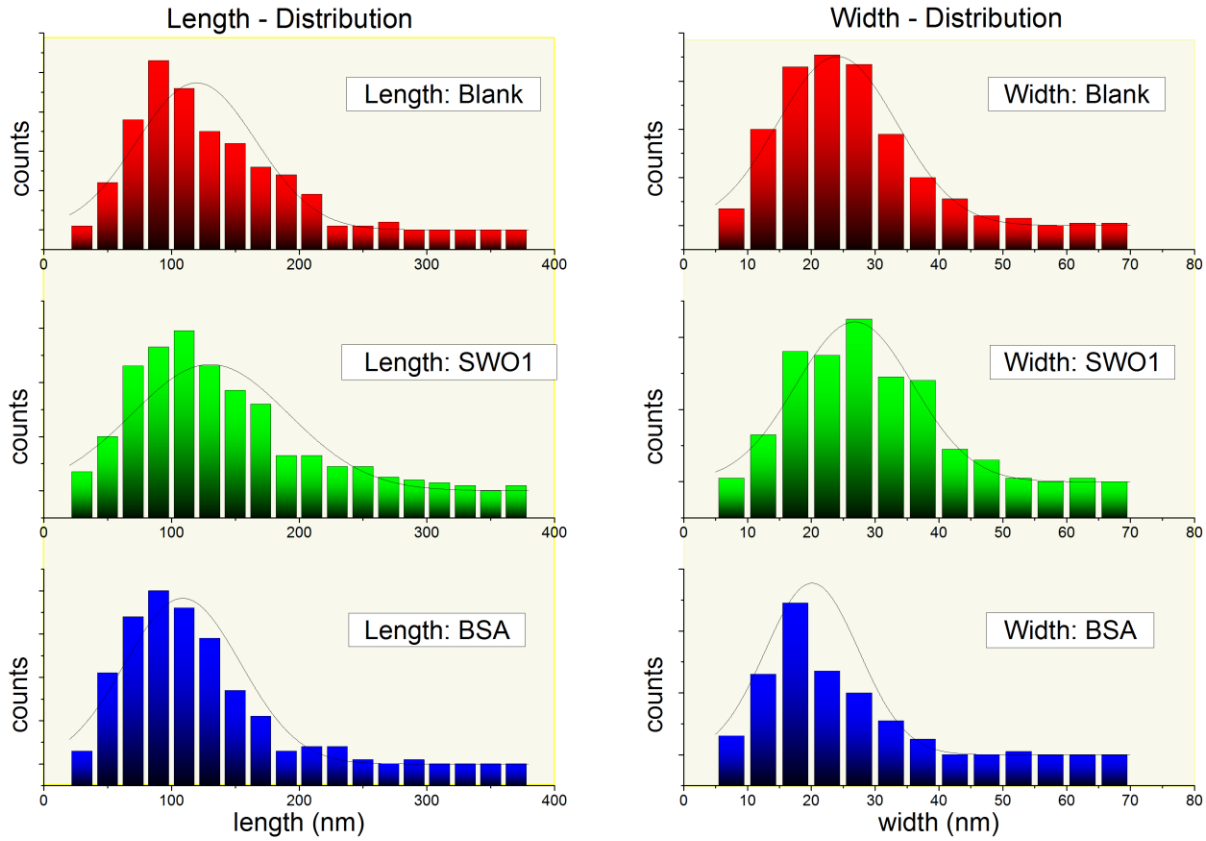

Figure 65: AFM based length (left) and width (right) distribution for NCC45 in untreated (red), SWO1 incubated (green) and BSA incubated (blue) samples after 20 hours at 40 °C.

6.4.3.2 *Swollenin on Avicel - XRD*

Next, **XRD** has been used to investigate structural influences of swollenin on highly crystalline cellulose 1. In analogy to the **AFM** measurements, 20 h incubation at 40 °C and the same concentration of 20 mg/l has been carried out, followed by **XRD** characterization. Figure 66 shows the reference compared to the 20 h incubated sample. The spectra have been background corrected, **FFT** smoothed (5 points), normalized to the strongest peak and for ease of view stacked over each another. As can be seen they look widely identical and show typical peaks around angle 2Θ = 14.7 °, 16.6 ° and 22.7 ° corresponding to (101) and ($10\bar{1}$) and (002) crystal planes of cellulose 1 respectively. Amorphization was not observed and a corresponding broad peak ranging from 2Θ = 10 ° to 30 ° with a maximum around 20 ° is not present [80]. In summary it can be concluded that **XRD** measurements are in agreement with **AFM** characterization, which strongly suggests that swollenin is neither chemically degrading nor amorphizing highly crystalline cellulose, which are the first slightly contradictory results compared to the main intention of this enzyme. Therefore we can proceed to mixed crystalline/amorphous cellulose substrate to investigate the swollenin influence on amorphous areas in the presence of crystalline parts.

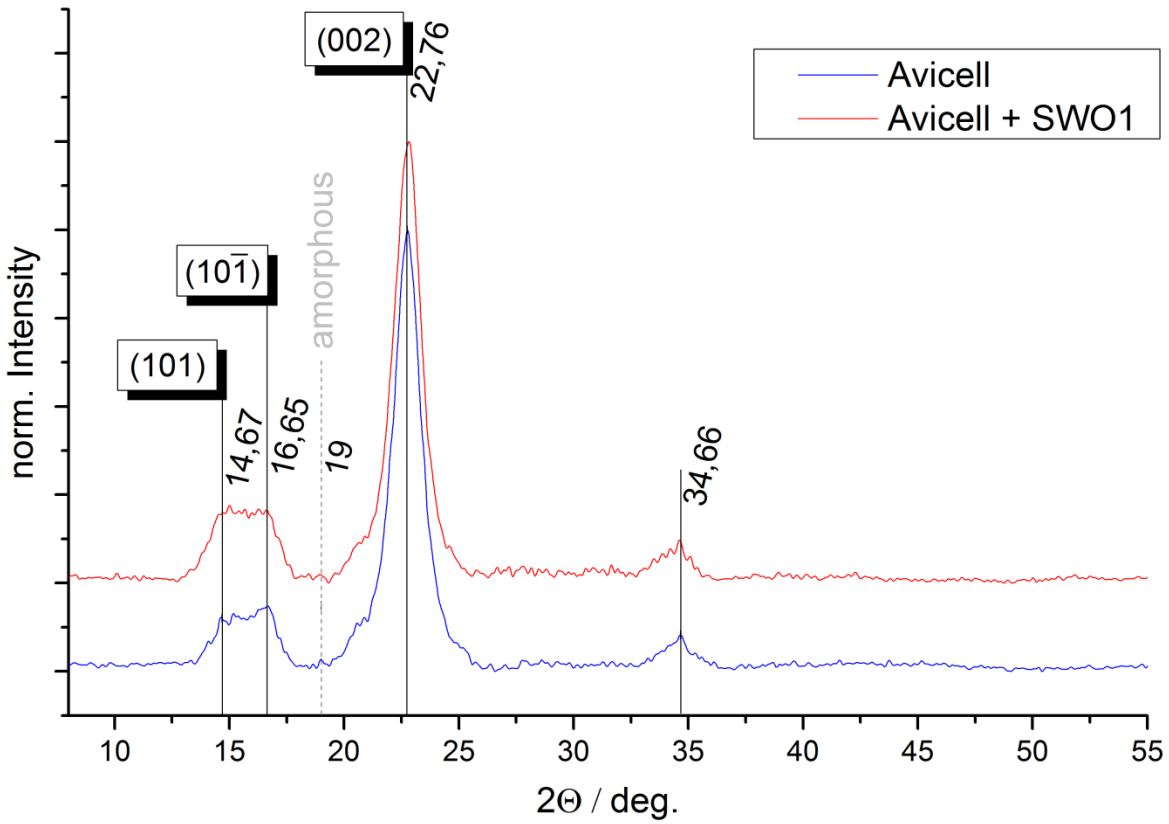

Figure 66: XRD investigation of Avicel 20h SWO incubated at 40 °C (red line) in direct comparison to an untreated reference sample (blue line). Spectra have been background filtered, FFT smoothed (5 points), normalized to the strongest peak and offset for ease of view. Crystalline cellulose 1 peaks are indicated by their miller indices at present 2Θ angles. At the dashed line an amorphous peak would have its maximum and it would range from 10 to 30 ° [80]**. Both spectra show typical crystalline cellulose 1 spectra.**

6.4.3.3 *Swollenin on Multiphasic Substrates - AFM*

For these types of investigations, **MACS** materials were chosen from the toolbox due to its easy recognition of large crystals, which are embedded in a fully amorphous matrix as discussed in detail by Ganner et-al [10]. In more detail, a sample with 17% crystallinity was selected as it provides micrometre-sized crystals. After cutting with the microtome the sample was immersed in H_2O and stored in the refrigerator for one day until the sample was transferred to the liquid holder shown in Figure 29 with sodium acetate buffer added for usage in the **FSB** together. Images were acquired continuously finding appropriate areas consisting of large crystals and amorphous areas as shown in Figure 67 by a height (left) and phase image (right) which identifies the surrounding areas as amorphous, however the contrast is not very strong and needs an experienced eye. Next, a comparable high tip force was used to generate a scratch across the crystal. This can be seen in the top left image of Figure 67 together with the encircled crystal (red dashed line). The scratch has been made deliberately to have an orientation marker in case of crystal degradation.

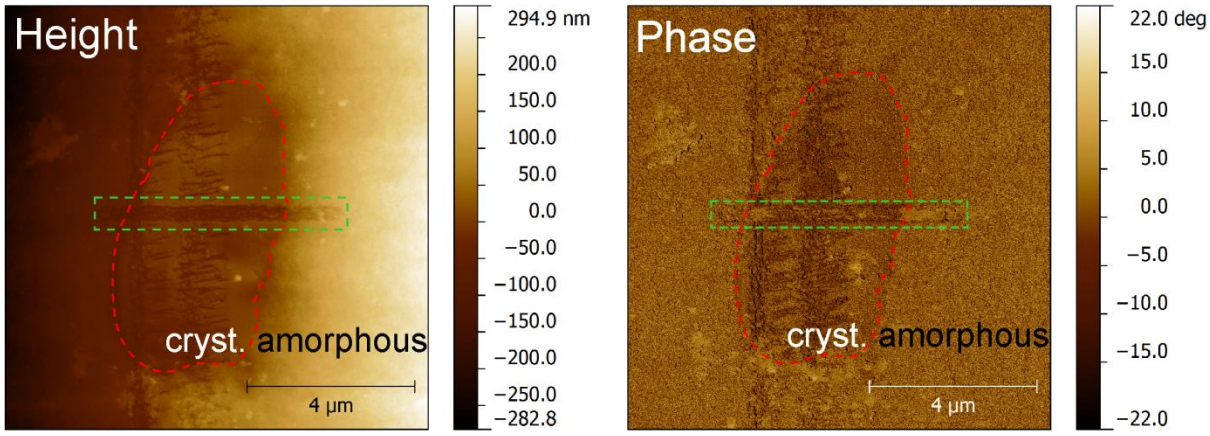

Figure 67: AFM height (left) and phase (right) images of a MACS17 sample before SWO1 incubation. The crystalline cellulose embedded in the amorphous matrix is highlighted by a red dashed line cycle on both images. The green dashed line rectangle indicates a scratch that was induced by applying high tip force to create a maker in case of crystal degradation.

After acquiring the reference image, the sample was incubated with a 20 mg/l **SWO1** solution for 15 minutes followed by further imaging to see the first effects. The results can be seen in the top right image of Figure 68 which looks very similar to expectations for such short incubation time. Even after 1 hour of incubation, no effect can be identified, which is shown left in the next row of Figure 68. To accelerate a possible activity, the incubated sample was put into an incubator heated to 40 °C for 24 hours and again imaged afterwards. The result is shown in Figure 68 second row right which shows a virtually identical image compared to the reference images. To get more detailed information concerning degradation possibilities, cross-sectional profiles were taken across the embedded crystal. To always measure the profile at the same position the scratch caused by high tip force mentioned above was deliberately used. The scratch is schematically indicated in the left image of Figure 67 and in all **AFM** height images in Figure 68 by a green dashed line rectangle. The results are shown together in the graph at the lower part of Figure 68 in black, red and green for reference, 1 h after incubation, and 24 h after incubation, respectively. To distinguish between crystalline and amorphous areas, the crystalline area of cross-sectional profiles is shaded light red. As is evident from this direct comparison, there is practically no activity on crystalline or amorphous regions. While the former was already expected as described in the previous chapters, the latter was slightly unexpected as swollenin was intended to infiltrate amorphous regions and make them swell as the name implies. However, no such tendencies could be found on numerous samples including fully amorphous thin film cellulose substrates as described in chapter 6.3.2.

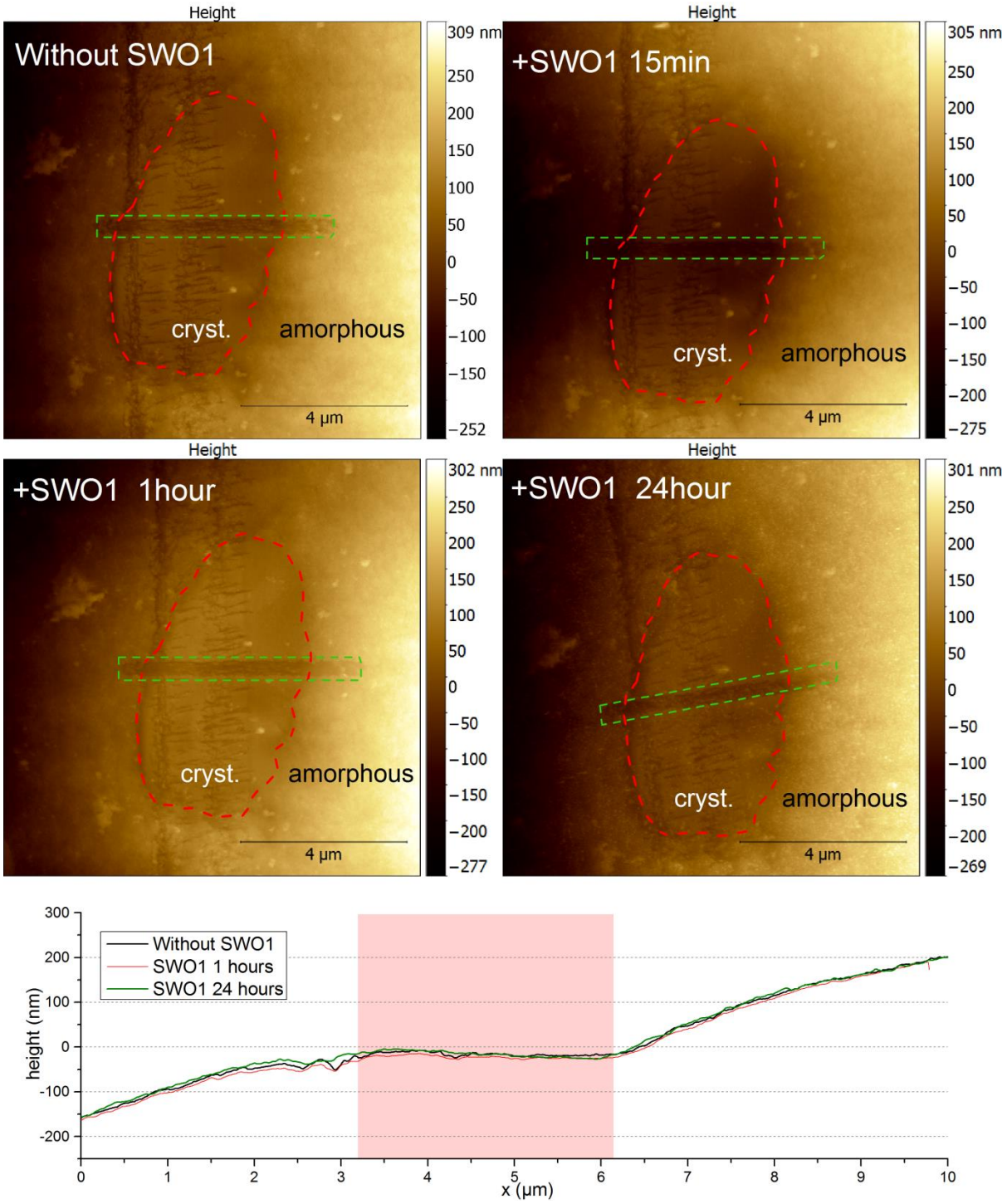

Figure 68: Sequential swollenin incubation of multiphasic cellulose substrates (MACS). The two top rows gives AFM height images in buffer solution (top left), after 15 min SWO1 incubation (top right), and after 1 h SWO1 incubation at 24 h for accelerated activities (row below from left and right). The dashed, red line encircles the crystal as identified in Figure 67 embedded in an amorphous matrix. The horizontal scratch was made deliberately for orientation with respect to cross-sectional profiles shown as green dashed line rectangle in the AFM images. The lower graph shows these profiles together with a light red shaded indicating crystalline (x = 3 - 6 µm) and the other amorphous region. It is evident that there is practically no degradation on crystalline or amorphous regions.

The next step was adding **SVG** to investigate whether ***1)*** the swollenin modified the cellulose surface to reduce or even inhibit classical supernatant reactions; or ***2)*** there were existing synergistic effects between swollenin and **CBH1**/**CBH2**/**EG** supernatants. For that we directly added **SVG** with a con-

centration of 20 mg/l after the last measurements discussed above. Figure 69 summarizes the results and shows the degradation behaviour in the top left part. The degradation velocity of v_d = 0.7 ± 0.1 nm/min is a bit lower, but within limits of degradation experiments performed by Rošker et al. [11] with **SVG** on **MACS** that have v_d = 0.8 ± 0.3 nm/min . A short clip of this experiment can be found on the enclosed digital storage *("File 4 – Degradation with SVG of MACS 17 after 24h SWO incub.mp4"*). The top right **AFM** height image in Figure 69 gives the surface after 4.5 h as the last measurement point again with the encircled crystal as discussed above and shown in Figure 67 and Figure 68. Besides the fact that it looks like the degradation starts right away, which is an effect that has also been found in degradation experiments with solely **SVG,** the excavation of larger crystals is evident as observed before on such substrates [4, 5]. The lower part of Figure 69 again gives a direct comparison of height cross sections taken from the area near the deliberate scratch indicated by the green dashed rectangle in the **AFM** image top right. Here, the degradation becomes evident, which primarily takes place at amorphous regions while the crystalline area indicated by the light red shaded does not degrade. From these results we can now derive the following facts: ***1)*** swollenin does not swell cellulose equally whether it is amorphous or crystalline, proven by 24 hour incubation at 40 °C, ***2)*** the degradation of cellulose by supernatant **SVG** is not affected by swollenin v_d is, although slightly lower within limits of comparable degradation experiment that distinguish only in the absence of swollenin [11].

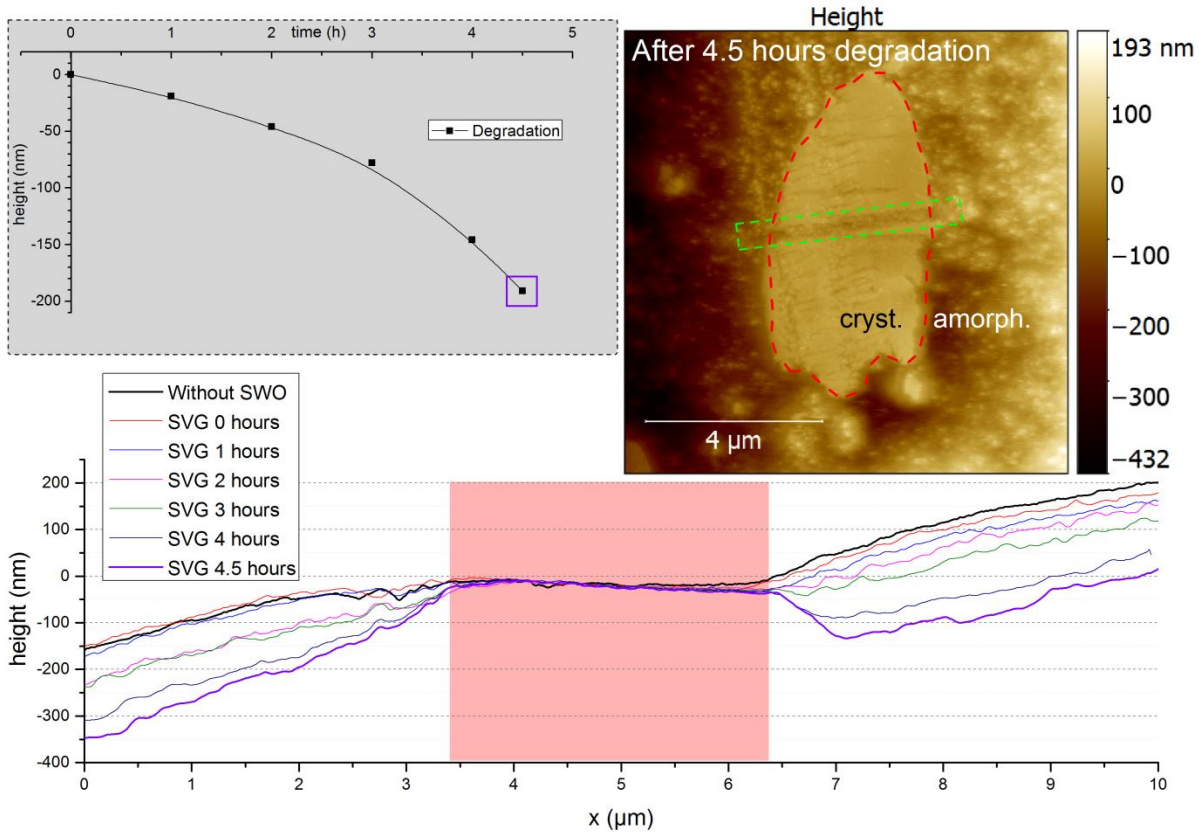

Figure 69: Follow-up experiment degradation of MACS 17 sample with SVG and measured via AFM. The graph marked with a grey background (left top) shows the degradation rate extracted from line profiles of AFM images. The height image (top right) shows the substrate at the end of the experiment after 4.5 hours. Corresponding to Figure 67 and Figure 68 the crystalline cellulose area is again circled with a red dashed line and the deliberate scratch is indicated by green dashed line rectangle. Long graph (lower part) shows line profiles taken from images near the deliberate scratch at different points in time, the light red shaded area corresponds to the crystalline area seen inside the red circle in the height image (top right).

6.4.3.4 *Summary: Swollenin*

Comprehensive insight via different methods strongly suggests that swollenin shows no significant interaction with cellulose. First we showed that on **NCC** after 20 h incubation at 40 °C with **SWO1** no change in crystallite size or shape occurred. This was once more proven by structural investigation via **XRD**. Avicel was also incubated there for 20 h at 40 °C. Because we found swollenin inactive on crystalline cellulose particles, the **MACS** substrate was chosen from the toolbox to check if swollenin shows activity on amorphous cellulose. And last but not least, because swollenin did not show activity on amorphous cellulose either, degradation experiments have been performed to investigate whether swollenin has a synergistic affect with **SVG**. Because this experiment showed the same degradation velocity of $v_d = 0.7 \pm 0.1$ nm/min which was within limits of degradation experiments performed by Rošker et al. [11] with **SVG** on **MACS** that have $v_d = 0.8 \pm 0.3$ nm/min, no further experiments that would have been carried out on **SCTFC** with single and sequential enzymes were initiated. To combine all acquired data, swollenin was found to be inactive on primitive cellulose and all reported effects [35, 37, 79] seem to be related to other components integrated in the plant cell wall.

7 Summary and Outlook

The main intention of this master's thesis was the development of cellulose-based substrates dedicated to real-time atomic force microscopy (**AFM**) investigations in liquid environments. To allow spatial resolution towards the molecular scale for fundamental studies, such substrates have to fulfil several demands: ***1)*** nano-flat surfaces (< 10 nm **RMS** roughness) over large areas (> 100 μm^2); ***2)*** fully amorphous and/or fully crystalline character; ***3)*** tunability of the crystalline content in amorphous matrices together with defined sizes of cellulose nano-crystals; and ***4)*** a *close-to-nature* character concerning their chemical and structural peculiarities. In this context it is important to mention that this thesis expands already available cellulose substrates at the Institute for Electron Microscopy and Nanoanalysis (**FELMI**, **TU** Graz), namely fractionate-solvent-exchange-cellulose (**FSEC** 2009 – 2012), multiphase-artificial-cellulose-substrate (**MACS** 2011 – 2014), and amorphous-cellulose-thin-film-cellulose (**ACTFC** 2012 – 2014). Although these substrates have individual advantages and were successfully used for specific purposes, none of them could fulfil all the demands at the same time. The broad knowledge gathered during their development, however, led to a new approach which had the potential to reach the goal of a high-fidelity cellulose substrate. In more detail, the idea was to first develop a route for the extraction of nano-crystalline cellulose with a narrow size distribution. Next, such crystals were thought to be combined with fully amorphous **ACTFC** substrates acting as an embedding matrix. This, hypothetically, should fulfil all demands for an ideal cellulose substrate: multiphasic, tunable, nano-flat cellulose. As shown in this thesis, this approach was not only successful concerning the substrate fabrication itself but also allowed new investigations which were not possible before.

Prior to the substrate development, however, the thesis concentrated on the ramp-up and the excessive testing of a new atomic force microscope which was installed at the **FELMI** in 2014: the *FastScanBio* (**FSB**) from Bruker Nano. This instrument is dedicated to high-speed scanning in liquid conditions down to the molecular scale. Therefore, as a first step the capabilities were tested and compared to the previously used **AFM** in chapter 6.1 which included speed tests in combination with elevated temperatures. It could be impressively demonstrated that frame rates close to 1 second can be achieved without significantly losing spatial resolution. Although a considerable investment in time, this performance tuning was needed for further achievements in this study.

In the second part, an extraction route for nano-crystalline cellulose (**NCC**) was developed and optimized. As described in detail in chapter 6.2, **AFM**, scanning electron microscopy (**SEM**), transmission electron microscopy (**TEM**), X-ray diffraction (**XRD**), and Raman spectroscopy have been used to provide a detailed insight into morphological, chemical and structural aspects of **NCC** substrates. In more detail, a route was found which allows the extraction of cellulose nano-crystals with lengths and widths of about 225 ± 76 nm and 20 ± 5 nm, respectively, which are dispersed in organic solvents. The latter then allows spin cast-based film preparation leading to homogenously distributed nano-crystals on flat surfaces: nano-crystalline-thin-film-cellulose substrate or **NCTFC**. Degradation experiments with well-known enzymes revealed identical behaviour as reported for natural cellulose, which confirmed the *close-to-nature* character in agreement with chemical and structural investigations. **FELMIs** substrate toolbox has therefore successfully expanded by a new type of cellulosic material which is perfectly suited to investigating activities on thin layers of cellulose nano-crystals.

The third part of this thesis finally combined **NCCs** with previously developed **ATFC** materials. The latter uses a cellulose precursor which is dissolved in organic solvents. This allows combination with the NCC dispersion before spin casting, followed by an HCl curing step which finally converts the thin layer into pure cellulose. The results can be considered the main achievement of this thesis: the semicrystalline-thin-film-cellulose or **SCTFC** substrate. As described in detail in chapter 6.3, final

films reveal surfaces with less than 10 nm **RMS** roughness even over large areas of hundreds of micrometres. High-resolution **AFM** imaging together with **TEM** and **SEM** investigations confirmed the dispersed distribution of **NCCs** in the amorphous matrix as intended. By adapting the relative **NCC** concentration in the **ACTFC** precursor solution, a tuning of the crystalline content in the substrate became possible. On the other hand, the total concentration of **ACTFC** precursor and **NCC** enables the control of the film thickness ranging from about 50 nm up to 500 nm and more. Finally, detailed enzymatic degradation experiments with well-known cellulases were conducted. As described in detail in chapter 6.4.1 and 6.4.2, individual degradation mechanisms were found in agreement with natural cellulose reported in literature. By that, the *close-to-nature* aspect of **SCTFC** substrates has been confirmed, which further expands the cellulose substrate toolbox by a unique material as intended for this master's thesis.

The final step was the application of the new substrates (**NCTFC** and **SCTFC**) for a novel enzyme: swollenin. As discussed in 6.4.3, **AFM** and **XRD** could successfully disprove the hypothesis that swollenin degrades and/or amorphizes cellulose crystals as speculated in literature. Furthermore, dynamic high-speed **AFM** was used to further disprove an accelerated degradation for mixed amorphous/crystalline materials which was also hypothesized in literature. More detailed investigations on a molecular level are planned for the future which include nano-mechanical studies to prove/disprove local swelling functionalities which gave this new enzyme its name.

In summary, the main achievements of this thesis are threefold. Firstly, a semicrystalline thin film cellulose (**SCTFC**) substrate has been developed which provides flatness on the lower nanoscale with tunable cellulose nano-crystal contents embedded in an amorphous matrix with a tunable film thickness. Together with the close-to-nature properties, this substrate type is ideally suited to high-speed, high-resolution **AFM** investigations in liquid environments with particular relevance in the field of enzymatic cellulose degradation. Secondly, **FELMIs** toolbox of cellulose substrates has been expanded by nano-crystalline thin films (**NCTFC**) and semicrystalline thin films (**SCTFC**). The ideal substrate can therefore be chosen depending on the individual purpose ranging from fully amorphous, fully crystalline, and semicrystalline with variable crystal sizes from the nanometre to the micrometre scale on enormously flat surfaces. Thirdly, light was shed on the activity of a new enzyme called swollenin and, together with the new substrate types, it could be shown that this enzyme neither amorphizes crystalline cellulose nor accelerates degradation activities in the presence of classical enzymes.

As an outlook it can be stated that we came a little closer to single enzyme tracking on seconds time scale due to the successful development of the high-fidelity **SCTFC** substrate. In terms of cellulose materials it must be mentioned that although superior in their qualities, one detail is still missing: the capability to fabricate such materials in specific places with defined shapes. This would be highly interesting with respect to bioelectronics applications such as localized sensors, which require cellulose coverage. Such attempts are currently ongoing and the first results are very promising as micrometre-sized, fully amorphous cellulose structures have been successfully fabricated.

8 List of Abbreviations

AFM	atomic force microscope/microscopy
AGU	anhydroglucose units
ATFC	amorphous thin film cellulose
BGL	β-glucosidase
BMIMCl	1-N-butyl-3-methylimidazoliumchlorid
BSE	back-scattered electrons
CBD	cellulose-binding domain
CBH	cellobiohydrolase
CBM	carbohydrate-binding module
EC	enzyme commission number
EDX(S)	energy dispersive X-ray (spectroscopy)
EELS	electron energy loss spectroscopy
EG	endo-glucanase
FELMI	Institute for Electron Microscopy and Nanoanalysis of TU Graz
FFT	fast Fourier transform
FSB	Fast Scan Bio (AFM instrument from Bruker)
FSEC	fractional solvent exchange cellulose
GHF9	glycosyl hydrolase family 9
LIMI	light microscope/microscopy
MACS	multiphase artificial cellulose substrate
NCC	nano-crystalline/crystallite cellulose
NCTFC	nano-crystalline thin film cellulose
NMR	nuclear magnetic resonance spectroscopy
PSD	position sensitive photodetector
RMS	route mean square (for roughness analysis)
SCC	spin-cast cellulose
SCTFC	semicrystalline thin film cellulose
SE	secondary electrons
SEM	scanning electron microscope/microscopy
SVG	supernatant from *Trichoderma reesei*
TEM	transmission electron microscope/microscopy
TMSC	trimethylsilyl cellulose
XRD	X-ray diffractometry
ZFE	Graz Centre for Electron Microscopy

9 Bibliography

1. Keppel-Aleks G, Wennberg PO, O'Dell CW, Wunch D (2013) Towards constraints on fossil fuel emissions from total column carbon dioxide. Atmos Chem Phys 13:4349–4357. doi: 10.5194/acp-13-4349-2013
2. Wodon Q, Burger N, Grant A, Liverani A (2014) Climate change, migration, and adaptation in the MENA Region.
3. Eibinger M, Ganner T, Rosker S, Kracher D, Haltrich D, Ludwig R, Eibinger M, Ganner T, Bubner P, Ros S, Kracher D, Haltrich D, Ludwig R, Plank H, Nidetzky B (2014) Cellulose Surface Degradation by a Lytic Polysaccharide Monooxygenase and Its Effect on Cellulase Hydrolytic. doi: 10.1074/jbc.M114.602227
4. Bubner P, Dohr J, Plank H, Mayrhofer C, Nidetzky B (2012) Cellulases dig deep: in situ observation of the mesoscopic structural dynamics of enzymatic cellulose degradation. J Biol Chem 287:2759–65. doi: 10.1074/jbc.M111.257717
5. Ganner T, Aschl T, Eibinger M, Bubner P, Meingast A, Chernev B, Mayrhofer C, Nidetzky B, Plank H (2014) Tunable mixed amorphous–crystalline cellulose substrates (MACS) for dynamic degradation studies by atomic force microscopy in liquid environments. Cellulose 21:3927–3939. doi: 10.1007/s10570-014-0419-8
6. Bubner P, Plank H, Nidetzky B (2013) Visualizing cellulase activity. Biotechnol Bioeng 110:1529–49. doi: 10.1002/bit.24884
7. Ganner T, Bubner P, Eibinger M, Mayrhofer C, Plank H, Nidetzky B (2012) Dissecting and reconstructing synergism: in situ visualization of cooperativity among cellulases. J Biol Chem 287:43215–22. doi: 10.1074/jbc.M112.419952
8. Dohr J (2011) Enzymatic degradation of superflat cellulose surfaces. Nano Optics Department (Karl Franzens University of Graz), in collaboration with the Institute for Electron Microscopy and Nanoanalysis. 100
9. Aschl T (2013) Tunable artificial cellulose substrates for in situ AFM investigation of enzymatic degradation. Graz University of Technology, Institue of Electron Microscopy and Nanoanalysis in collaboration with the Graz Centre of Electron Microscopy. 96
10. Ganner T (2012) Enzymatic cellulose degradation via atomic force microscopy in liquid environments. Graz University of Technology, Institue of Electron Microscopy and Nanoanalysis in collaboration with the Graz Centre of Electron Microscopy. 110
11. Rošker S (2013) Fabrication of multiphase artificial cellulose substrates for AFM based real time investigations of enzymatic degradation. Graz University of Technology, Institue of Electron Microscopy and Nanoanalysis in collaboration with the Graz Centre of Electron Microscopy. 86
12. Davison A, Blaxter M (2005) Ancient origin of glycosyl hydrolase family 9 cellulase genes. Mol Biol Evol 22:1273–84. doi: 10.1093/molbev/msi107
13. Payen A, Persoz JJ-F (1833) Mémoire sur la Diastase, les principaux Produits de ses Réactions, et leurs applications aux arts industriels. Ann chim phys 53:73–92.
14. Schwarz JCP (1973) Rules for Conformation Nomenclature for Five- and Six-membered Rings in Monosaccharides and their Derivatives. 505–508.
15. Hesse M, Meier H, Zeeh B (2005) Spektroskopische Methoden in der organischen Chemie, 8th ed. New York 2:512. doi: 10.1007/BF01524624
16. Kadla JF (2008) Biomass Fundamentals: Cellulose & Hemicelluloses. http://www.ncsu.edu/biosucceed/courses/biomass/biomass-introduction-course-material/module12/Module 12.pptx.
17. Nishiyama Y, Langan P, Chanzy H (2002) Crystal Structure and Hydrogen-Bonding System in Cellulose Iβ from Synchrotron X-ray and Neutron Fiber Diffraction. J Am Chem Soc 124:9074–9082. doi: 10.1021/ja0257319
18. O'sullivan A (1997) Cellulose: the structure slowly unravels. Cellulose 4:173–207. doi: Chemistry and Materials Science

19. Park S, Baker JO, Himmel ME, Parilla P a, Johnson DK (2010) Cellulose crystallinity index: measurement techniques and their impact on interpreting cellulase performance. Biotechnol Biofuels 3:10. doi: 10.1186/1754-6834-3-10
20. Blackwell J, Marchessault RH (1971) Infrared spectroscopy (of cellulose), structure studies. Cellul. Cellul. Deriv. part 4. Bikales and Segal; Wiley Interscience, pp 1–37
21. Wertz J-L, Bédué O, Mercier JP (2010) Cellulose science and technology. Epfl Press
22. Klemm D, Heublein B, Fink H-P, Bohn A (2005) Cellulose: fascinating biopolymer and sustainable raw material. Angew Chem Int Ed Engl 44:3358–93. doi: 10.1002/anie.200460587
23. Pérez S, Samain D (2010) Structure and Engineering of Celluloses. Adv Carbohydr Chem Biochem 64:26–116. doi: 10.1016/S0065-2318(10)64003-6
24. Slaytor M (1992) Cellulose digestion in termites and cockroaches: What role do symbionts play? Comp Biochem Physiol - B Biochem Mol Biol 103:775–784. doi: 10.1016/0305-0491(92)90194-V
25. Bhat M, Bhat S (1997) Cellulose degrading enzymes and their potential industrial applications. Biotechnol Adv 15:583–620.
26. Bayer E a, Belaich J-P, Shoham Y, Lamed R (2004) The cellulosomes: multienzyme machines for degradation of plant cell wall polysaccharides. Annu Rev Microbiol 58:521–54. doi: 10.1146/annurev.micro.57.030502.091022
27. Lehtiö J, Sugiyama J, Gustavsson M, Fransson L, Linder M, Teeri TT (2003) The binding specificity and affinity determinants of family 1 and family 3 cellulose binding modules. Proc Natl Acad Sci U S A 100:484–9. doi: 10.1073/pnas.212651999
28. Lynd LR, Weimer PJ, Zyl WH Van, Pretorius IS (2002) Microbial Cellulose Utilization : Fundamentals and Biotechnology. 66:506–577. doi: 10.1128/MMBR.66.3.506
29. Ahola S, Turon X, Osterberg M, Laine J, Rojas OJ (2008) Enzymatic hydrolysis of native cellulose nanofibrils and other cellulose model films: effect of surface structure. Langmuir 24:11592–9. doi: 10.1021/la801550j
30. Nidetzky B, Steiner W, Hayn M, Claeyssens M (1994) Cellulose hydrolysis by the cellulases from Trichoderma reesei: a new model for synergistic interaction. Biochem J 298 Pt 3:705–10.
31. Suurnäkki A, Tenkanen M (2000) Trichoderma reesei cellulases and their core domains in the hydrolysis and modification of chemical pulp. 189–209.
32. Mellitzer A, Weis R, Glieder A, Flicker K (2012) Expression of lignocellulolytic enzymes in Pichia pastoris. Microb Cell Fact 11:61. doi: 10.1186/1475-2859-11-61
33. ESTERBAUER H, Steiner W, LABUDOVA I, HERMANN A, Hayn M (1991) Production of Trichoderma cellulase in laboratory and pilot scale. Bioresour Technol 36:51–65.
34. Cosgrove DJ (2000) Loosening of plant cell walls by expansins. Nature 407:321–326.
35. Saloheimo M, Paloheimo M, Hakola S, Pere J, Swanson B, Nyyssönen E, Bhatia A, Ward M, Penttilä M (2002) Swollenin, a Trichoderma reesei protein with sequence similarity to the plant expansins, exhibits disruption activity on cellulosic materials. Eur J Biochem 269:4202–4211. doi: 10.1046/j.1432-1033.2002.03095.x
36. Horwitz A, Duggan K, Buck C, Beckerle MC, Burridge K (1986) Interaction of plasma membrane fibronectin receptor with talin[mdash]a transmembrane linkage. Nature 320:531–533.
37. Gourlay K, Hu J, Arantes V, Andberg M, Saloheimo M, Penttilä M, Saddler J (2013) Swollenin aids in the amorphogenesis step during the enzymatic hydrolysis of pretreated biomass. Bioresour Technol 142:498–503. doi: 10.1016/j.biortech.2013.05.053
38. Binnig G, Rohrer H, Gerber C, Weibel E (1982) Surface studies by scanning tunneling microscopy. Phys Rev Lett 49:57–61. doi: 10.1103/PhysRevLett.49.57
39. Binnig G, Quate CF (1986) Atomic Force Microscope. Phys Rev Lett 56:930–933. doi: 10.1103/PhysRevLett.56.930
40. García R (2010) Amplitude modulation atomic force microscopy. John Wiley & Sons
41. Hanley SJ, Gray DG (1995) Atomic force microscopy. CRC Press, Inc. Boca Raton, Fl
42. Casero E, Vázquez L, Parra-Alfambra AM, Lorenzo E (2010) AFM, SECM and QCM as useful analytical tools in the characterization of enzyme-based bioanalytical platforms. Analyst 135:1878–903. doi: 10.1039/c0an00120a
43. Wei ZQ, Wang C, Bai CL (2000) Surface imaging of fragile materials with hydrophobic atomic force microscope tips. Surf Sci 467:185–190. doi: 10.1016/S0039-6028(00)00783-4

44. Cohen SH, Lightbody ML, Bray MT (1999) Atomic force microscopy/scanning tunneling microscopy 3. Springer
45. Plank H (2014) Materials Characterization III, Institue of Electronmicroscopy and Nanoanalysis, Graz, Technical University.
46. Nečas D, Klapetek P (2012) Gwyddion: an open-source software for SPM data analysis. Cent Eur J Phys 10:181–188. doi: 10.2478/s11534-011-0096-2
47. Nečas D, Klapetek P Gwyddion.
48. Hutter JL, Bechhoefer J (1993) Calibration of atomic-force microscope tips. Rev Sci Instrum 64:1868–1873. doi: 10.1063/1.1143970
49. San Paulo a, García R (2000) High-resolution imaging of antibodies by tapping-mode atomic force microscopy: attractive and repulsive tip-sample interaction regimes. Biophys J 78:1599–1605. doi: 10.1016/S0006-3495(00)76712-9
50. Bruker (2014) NanoScope 9.1 - Manual.
51. Warren BE (1969) X-ray Diffraction. Courier Corporation
52. Klug HP, Alexander LE, others (1954) X-ray diffraction procedures. Wiley New York
53. Ryland a. L (1958) X-Ray Diffraction. J Chem Educ 35:80 – 83.
54. Bergmann L, Schaefer C, Raith W, Bauer MBVSJ, Gutdeutsch R, Hantel M (2005) Lehrbuch der Experimentalphysik: Band 6: Festkörper. Walter de Gruyter
55. Fengel D, Jakob H, Strobel C (1995) Influence of the Alkali Concentration on the Formation of Cellulose II. Study by X-Ray Diffraction and FTIR Spectroscopy. Holzforschung 49:505–511. doi: 10.1515/hfsg.1995.49.6.505
56. Agarwal UP, Reiner RS, Ralph S a. (2010) Cellulose I crystallinity determination using FT–Raman spectroscopy: univariate and multivariate methods. Cellulose 17:721–733. doi: 10.1007/s10570-010-9420-z
57. Bansal P, Hall M, Realff MJ, Lee JH, Bommarius AS (2010) Multivariate statistical analysis of X-ray data from cellulose: a new method to determine degree of crystallinity and predict hydrolysis rates. Bioresour Technol 101:4461–71. doi: 10.1016/j.biortech.2010.01.068
58. Poletto M, Pistor V, Zattera AJ (2013) Structural Characteristics and Thermal Properties of Native Cellulose. Cellul – Fundam Asp 45–68.
59. Edwards HG, Farwell DW, Webster D (1997) FT Raman microscopy of untreated natural plant fibres. Spectrochim Acta A Mol Biomol Spectrosc 53A:2383–92.
60. Long DA (1977) Raman spectroscopy. New York 1–597.
61. Fischer S, Schenzel K, Fischer K, Diepenbrock W (2005) Applications of FT Raman Spectroscopy and Micro Spectroscopy Characterizing Cellulose and Cellulosic Biomaterials. Macromol Symp 223:41–56. doi: 10.1002/masy.200550503
62. Schenzel K, Fischer S (2001) NIR FT Raman spectroscopy - A rapid analytical tool for detecting the transformation of cellulose polymorphs. Cellulose 8:49–57. doi: 10.1023/A:1016616920539
63. Williams DB, Carter CB (1996) The Transmission Electron Microscope. Springer
64. Goldstein JI, Newbury DE, Echlin P, Joy DC, Fiori C, Lifshin E, others (1981) Scanning electron microscopy and X-ray microanalysis. A text for biologists, materials scientists, and geologists. Plenum Publishing Corporation
65. Sturcová A, His I, Apperley DC, Sugiyama J, Jarvis MC (2004) Structural details of crystalline cellulose from higher plants. Biomacromolecules 5:1333–9. doi: 10.1021/bm034517p
66. VLSI Standards (2012) Surface Topography Reference, Model STR 10. www.vlsistandards.com. Accessed 7 Feb 2015
67. Edgar CD, Gray DG (2003) Smooth model cellulose I surfaces from nanocrystal suspensions. 299–306.
68. Sato K, Shikida M, Yamashiro T, Tsunekawa M, Ito S (1999) Roughening of single-crystal silicon surface etched by KOH water solution. Sensors Actuators A Phys 73:122–130. doi: 10.1016/S0924-4247(98)00270-2
69. Okanot T, Sark A (1985) Intermediates and a Possible Mercerization Mechanism *. 30:325–332.
70. Ardizzone S, Dioguardi FS, Mussini T, Mussini PR (1999) Microcrystalline cellulose powders : structure , surface features and water sorption capability. 57–69.
71. Brown CW, Kester AXDR, Daly FP, Brown CW, Kester DR (1972) Sodium and Magnesium Sulfate. 76:

72. Geffroy C, Labeau M., Wong K, Cabane B, Cohen Stuart M. (2000) Kinetics of adsorption of polyvinylamine onto cellulose. Colloids Surfaces A Physicochem Eng Asp 172:47–56. doi: 10.1016/S0927-7757(00)00499-4
73. Kontturi EJ (2005) Surface chemistry of cellulose.
74. Cooper GK, Sandberg KR, Hinck JF (1981) Trimethylsilyl cellulose as precursor to regenerated cellulose fiber. J Appl Polym Sci 26:3827–3836. doi: 10.1002/app.1981.070261129
75. Mohan T, Kargl R, Doliška A, Ehmann HMA, Ribitsch V, Stana-Kleinschek K (2013) Enzymatic digestion of partially and fully regenerated cellulose model films from trimethylsilyl cellulose. Carbohydr Polym 93:191–8. doi: 10.1016/j.carbpol.2012.02.033
76. Nyfors L, Suchy M, Laine J, Kontturi E (2009) Ultrathin cellulose films of tunable nanostructured morphology with a hydrophobic component. Biomacromolecules 10:1276–81. doi: 10.1021/bm900099e
77. Mohan T, Kargl R, Doliška A, Vesel A, Köstler S, Ribitsch V, Stana-Kleinschek K (2011) Wettability and surface composition of partly and fully regenerated cellulose thin films from trimethylsilyl cellulose. J Colloid Interface Sci 358:604–10. doi: 10.1016/j.jcis.2011.03.022
78. Tu M, Chandra RP, Saddler JN (2007) Recycling cellulases during the hydrolysis of steam exploded and ethanol pretreated Lodgepole pine. Biotechnol Prog 23:1130–7. doi: 10.1021/bp070129d
79. Brotman Y, Briff E, Viterbo A, Chet I (2008) Role of swollenin, an expansin-like protein from Trichoderma, in plant root colonization. Plant Physiol 147:779–789. doi: 10.1104/pp.108.116293
80. Ciolacu D, Ciolacu F, Popa VI (2011) Amorphous Cellulose – Structure and Characterization. Cellul Chem Technol 45:13–21.